POLITECNICO DI MILANO

Scuola di Ingegneria Industriale e dell'Informazione

Ingegneria Elettronica

Laurea Magistrale

IMPROVEMENTS ON ELASTIC RECOIL DETECTION ANALYSIS FOR MICROELECTRONIC APPLICATIONS

Promoter: Prof. Marcello Mariani

Co-promoter: Dr. Johan Meersschaut

Opponent: Dr. Federica Zanderigo

Student: Grazia Laricchiuta

Matriculation number: 777004

Academic Year 2013 - 2014

Table of contents

Table of figures

Table of tables

Abstract

Depth profiling of light elements, including hydrogen, became possible in IMEC after the Time-of-Flight Elastic Recoil Detection Analysis spectrometer was installed. But until now the depth profiling was dependent on human eye isotopic discrimination and on human input to select certain intervals of data.

In this thesis work automatic procedures for mass assignment and isotopic discrimination were developed. While requiring limited computational effort, the new procedures let the analysis be free from human errors and inputs.

Keywords: Elastic recoil detection analysis, TOF-ERDA, ERDA, time-of-flight, TOF, mass assignment procedure, isotopic discrimination procedure, decomposition procedure, recoil.

Estratto

L'analisi delle concentrazioni di elementi leggeri, incluso l'idrogeno, è divenuta possibile in IMEC dopo l'installazione di un sistema di rivelazione per Time-of-Flight Elastic Recoil Detection Analysis (TOF-ERDA). Ma fino ad oggi l'analisi dei campioni dipendeva dalla capacità dell'occhio umano di discriminare i segnali dei diversi elementi. Inoltre era necessario l'intervento dell'uomo per selezionare determinati intervalli di dati.

L'oggetto di questa tesi è lo sviluppo di una nuova tecnica di discriminazione degli elementi presenti in un campione. Nella prima parte della tesi è descritta una nuova procedura di assegnazione della massa, che, pur con un basso costo computazionale, è in grado di tener conto della risposta del rivelatore di energia del sistema.

La seconda parte della tesi studia la risoluzione del rivelatore di energia ed in seguito sviluppa la procedura di discriminazione degli isotopi presenti nel campione, chiamata 'decomposizione'.

La 'decomposizione' permette di discriminare isotopi presenti in un campione. Questa discriminazione è possibile anche per isotopi minoritari, i quali hanno segnali spesso indistinguibili all'occhio umano.

La 'decomposizione' permette, inoltre, di discriminare il contenuto isotopico del campione anche quando i segnali di più isotopi sono sovrapposti.

Come risultato della prima e della seconda procedura si giunge perciò ad un'analisi del campione che è completamente libera da intervento umano.

Parole chiave: Elastic recoil detection analysis, TOF-ERDA, ERDA, time-of-flight, TOF, procedura di assegnazione della massa, procedura di discriminazione isotopica, procedura di decomposizione, rinculo.

Introduction

For a deep understanding of semiconductor device, the characteristic properties of all the components, such as conductors, insulators and electrical junctions, need to be known. Since thin films are a major part of the research in semiconductor industry, the development and usability of the characterization methods for them are of great importance.

In material characterization, elemental information can be obtained from the inner electron structure of the atoms by means of proton induced X-ray emission, X-ray fluorescence, photoelectrons or Auger electrons emissions.

However, all the above mentioned methods are qualitative, or in the best case semi-quantitative, without high quality reference samples thus probing only the relative atomic concentrations of the sample and also often lack the possibility for direct detection of hydrogen. [14]

One technique which doesn't need any reference sample for the elemental concentration analysis and which allows to detect hydrogen concentration is Time-of-Flight Elastic Recoil Detection Analysis (TOF-ERDA).

In TOF-ERDA heavy ion beam kicks out of the sample towards the detector recoil ions. When both the recoil velocity and energy are measured the recoil mass can be determined. In the first part of this thesis we will introduce a new mass assignment procedure.

In the second part of this work we will study the development of an isotopic discrimination technique, called 'decomposition'. Decomposition allows to distinguish isotopic masses when recoils from different elements are overlapping.

1 Overview of spectrometry techniques

In this chapter, we introduce different material characterization techniques that are used in the development of advanced micro-electronic devices. Special attention will be given to Rutherford Backscattering spectrometry (RBS) and Elastic Recoil Detection Analysis (ERDA), two Ion Beam Analysis (IBA) techniques in which highly energetic ions are directed towards the target. The present thesis relates specifically to the advancement of the ERDA technique for micro-electronic applications.

1.1 Secondary Ion Mass Spectroscopy (SIMS)

SIMS is a surface analytical technique used to analyze the composition of solid surfaces and thin films by sputtering the surface of the specimen with a focused primary ion beam. The impact of the primary ions generates neutral atoms and charged ions. The ejected secondary ions emitted from the material are collected and analyzed in a mass analyzer.

The sputtering process removes material from the surface, thereby constantly exposing new, previously buried layers to analysis by the ion beam.

The secondary ion intensity for impurities as a function of time, $I_I(t)$, is a measure of the elemental concentration as a function of depth, $C_I(z)$. The conversion from $I_I(t)$ to $C_I(z)$ is roughly as follows: $I_I(t)$ is measured and converted into $I_I(z)$ by measuring the sputtered depth at the end of the measurement assuming a constant erosion rate.

The formula which relates $I_I(z)$ and $C_I(z)$ is

$$C_I(z) = RSF\frac{I_I(z)}{I_m(z)}$$

Eq. 1-1

where $I_m(z)$ is the ion intensity for a reference element m, typically the matrix species; RSF is the relative sensitivity factor.

The RSFs vary for each matrix and impurity element, they are generally derived from the measurement of ion implanted standards or other calibrated standards. There are RSF tables for Si and for compound semiconductors such as GaAs, InP or GaN.

Despite the difficulties for quantification, SIMS is at the moment the most heavily used technique for 1D doping profiling due to its high dynamic range (10E+14 −10E+21 at./cm^3), depth resolution (1-4 nm) and excellent sensitivity (ppm to ppb).

SIMS has the capability of analyzing all elements in the periodic table as well as isotopes. The detection limit for most trace elements is dependent on the type of instrumentation used, on the primary ion beam and the analytical area, and on other factors [2].

The drawbacks are that the technique is destructive, a crater with a diameter of 10 to 200µm is formed. Moreover, the quantification at the surface and at interfaces is not always accurate, i.e. in the case of boron and arsenic [2].

A classical SIMS set-up consists of:

1) primary ion gun generating the primary ion beam;

2) a primary ion column, accelerating and focusing the beam onto the sample (and in some instruments an opportunity to separate the primary ion species by a wien filter or to pulse the beam);

3) high vacuum sample-chamber holding the sample and the secondary ion extraction lens;

4) mass analyzer separating the ions according to their mass to charge ratio;

5) ion detection unit.

In the field of surface analysis, it is common to distinguish Static SIMS and Dynamic SIMS. Static SIMS is the process involved in surface atomic monolayer analysis, usually with a pulsed ion beam and a time of flight mass spectrometer. Dynamic SIMS, on the other hand, is the process involved in bulk analysis, closely related to the sputtering process, using a DC primary ion beam and a magnetic sector or quadrupole mass spectrometer.

A magnetic sector mass spectrometer uses a combination of an electrostatic analyzer and a magnetic analyzer to separate the secondary ions by their mass to charge ratio. A quadrupole mass spectrometer separates the masses by resonant electric fields, where only masses of choice are able to pass.

The time of flight mass analyzer separates the ions at a field free drift path according to their kinetic energy. It is the only SIMS analyzer type able to detect all the generated secondary ions together [2].

The choice of the primary ion beam depends on the required current (pulsed or continuous), on the species to be analyzed and on the sample to be investigated.

In the extreme limit, zero energy SIMS is a new emerging technique using a low energy electron primary beam to sputter the surface and a laser-beam to position the sputtered elements.

1.2 X-ray Photoelectron Spectrometry (XPS)

XPS is a spectroscopic technique that measures the surface elemental composition and chemical state. XPS spectra are obtained by irradiating a material with X-rays and by simultaneously measuring the kinetic energy and the number of electrons emitted by the surface atoms after direct energy transfer to the electrons.

For electrons escaping from the top 1 to 10 nm of the material being analyzed, the electron energy identifies the emitting atom. Thanks to the high energy resolution of the electron spectrometer, XPS provides information on the chemical and electronic state of the identified atoms [2].

XPS detects all elements with an atomic number equal to or bigger than 3, but is blind to H and He atoms[2] [23]. The detection limit for most of the elements is in the parts per thousand range (0.1-1.0 at.%). A detection limit of 100 ppm is possible, but it requires special conditions: concentration at top surface or very long collection time (8-16 hours) [2].

If combined with ion sputtering, elemental depth profiles can be obtained to a depth of hundreds of nanometers like in SIMS. The sputtering process introduces the exact same limitation previously discussed for SIMS, thus part of the sample destruction.

A typical XPS spectrum is a plot of the number of electrons detected versus their binding energy. As the binding energy of the core electrons are specific to each atom, the peak positions are characteristic of an element. Moreover, this energy depends on the chemical state and on the coordination of the atom. Each element produces a characteristic set of XPS peaks, correspondent to the electron configuration of the electrons within the atoms, i.e. 1s, 2s, 2p, etc. Their binding energy can be derived from the following expression:

$$E_{binding} = E_{photon} - E_{kinetic} - \Psi$$

Eq. 1-2

where E_{photon} is the energy of the X-ray photons being used, $E_{kinetic}$ is the kinetic energy of the emitted electron as measured by the instrument and Ψ is the work function of the spectrometer.

In addition, different multi-electron relaxation processes give rise to satellite peaks. Unfortunately, although the identification of the species is unique, different chemical configurations can give rise to the same binding energies. The identification of the chemical state is then sometimes more difficult.

It is important to note that XPS detects only the electrons ejected from the sample and collected at the spectrometer. During their way out to the surface of the sample, the photoelectrons undergo many scattering events, either elastic or inelastic. Only the electrons that have not lost any energy are of interest. The electrons inelastically scattered do not have any longer an energy characteristic of their atoms and are therefore useless in the identification process.

The number of detected electrons in each of the characteristic peaks is directly related to the amount of element within the area irradiated. To generate atomic percentage values, each raw XPS signal must be corrected by dividing its signal intensity by a ”relative sensitivity factor” and normalized over all of the elements detected.

The quantitative accuracy depends on several parameters such as: signal to noise ratio, peak intensity, accuracy of relative sensitivity factors, correction for electron transmission function,

surface volume homogeneity, correction for energy dependency of electron mean free path, and degree of sample degradation due to analysis.

The X-ray irradiation can generate sample degradation during the measurement. This sample degradation depends on the sensitivity of the material to the wavelength of X-rays used, the total dose of the X-rays, the temperature of the surface and the level of the vacuum. Polymers, catalysts, certain highly oxygenated compounds and various inorganic compounds can be degraded by either monochromatic or non-monochromatic X-ray sources. Because the vacuum removes various gases (e.g. O_2, CO) and liquids (e.g. water, solvents) that were initially trapped within or on the surface of the sample, the chemistry and morphology of the surface will continue to change until the surface achieves a steady state. This type of degradation is sometimes difficult to detect.

1.3 Auger electron spectroscopy

Auger electron spectroscopy (AES) is an analytical characterization technique for obtaining the chemical composition of solid surfaces. In AES, the sample is irradiated with electrons from an electron gun. Auger electrons are emitted and analyzed with an electron spectrometer. The experiment is carried out in a UHV environment because the AES technique is surface sensitive due to the limited mean free path of electrons in the kinetic energy range of 20 to 2500 eV.

The basic advantages of this technique are its high sensitivity for chemical analysis in the 5 to 20$\dot{A}$ region near the surface, a rapid data acquisition speed, its ability to detect all elements above helium, and its capability of high-spatial resolution.

Sputtering is sometimes used with AES to perform depth profiling experiments. Sputtering removes thin outer layers of a surface so that AES can be used to determine the underlying composition. Depth profiles are shown as either Auger peak height vs. sputter time or atomic concentration vs. depth.

The Auger effect is an electronic process at the heart of AES, resulting from the inter- and intra-state transitions of electrons in an excited atom. The Auger process can be understood by considering the ionization process of an isolated atom under electron bombardment. The incident electron with sufficient primary energy, E_P, ionizes the core level, such as a K level. The vacancy thus produced is immediately filled by another electron from L_1. The energy ($E_K - E_{L1}$) released from this transition can be transferred to another electron, as in the L_2 level. This electron is ejected from the atom as an Auger electron. The Auger electron will have energy given by:

$$E = E_K - E_{L1} - E_{L2}$$

Eq. 1-3

This excitation process is denoted as a KL_1L_2 Auger transition. It is obvious that at least two energy states and three electrons must take part in an Auger process. Therefore, H and He atoms cannot give rise to Auger electrons.

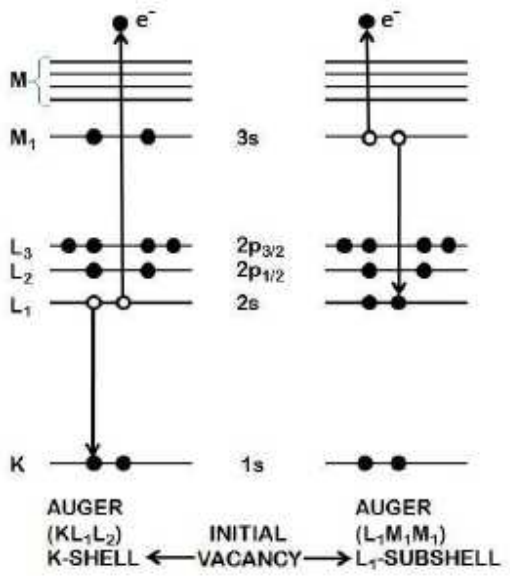

Figure 1-1 Schematic diagram of various two-electron de-excitation processes associated to Auger transitions.[2]

Several transitions (KL_1L_1, KL_1L_2, LM_1M_2, etc.) can occur with various transition probabilities. The Auger electron energies are characteristic of the target material and independent of the incident beam energy.

Surface sensitivity in AES arises from the fact that emitted electrons usually have energies ranging from 20 to 2500 eV and at these values, electrons have a short mean free path in a solid. The escape depth of electrons is therefore localized to within a few nanometers of the target surface, giving AES an extreme sensitivity to surface species.

Since the intensity of the Auger peaks may be small compared to the noise level of the background, AES is often run in a derivative mode which serves to highlight the peaks by modulating the electron collection current via a small applied AC voltage [2]. Plotting in derivative mode also emphasizes Auger fine structure which appear as small secondary peaks surrounding the primary Auger peak. These secondary peaks arise from the presence of the same element in multiple different chemical states on a surface (i.e. adsorbate layers) or from relaxation transitions involving valence band electrons of the substrate [2].

Quantitative compositional and chemical analysis of a sample using AES is dependent on measuring the yield of Auger electrons during a probing event. Electron yield, in turn, depends on several critical parameters such as electron-impact cross-section and fluorescence yield. Since the Auger effect is not the only mechanism available for atomic relaxation, there is a competition between radiative and non-radiative decay processes to be the primary de-excitation pathway.

Despite the advantages of high spatial resolution and precise chemical sensitivity attributed to AES, there are several factors that can limit the applicability of this technique. One of the most common limitations encountered with Auger spectroscopy are charging effects in non-conducting samples.

Charging results when the number of secondary electrons leaving the sample are greater or less than the number of incident electrons, giving rise to a net polarity at the surface. Both positive and negative surface charges severely alter the yield of electrons emitted from the sample and hence distort the measured Auger peaks. To complicate matters, neutralization methods employed in other surface analysis techniques, such as SIMS, are not applicable to AES, as these methods usually involve surface bombardment with either electrons or ions.

In addition to charging effects, AES data can be obscured by the presence of characteristic energy losses and higher order atomic ionization events. Electrons ejected from a solid will generally undergo multiple scattering events and lose energy.

1.4 Rutherford backscattering spectrometry (RBS)

RBS has been widely used for film thickness determination and composition analysis and in process development for more than 30 years. RBS is particularly suited for the quantification of heavy elements, which are detected with high sensitivity (around 10^{15} at./cm^2 [29]) and good mass resolution. On the other hand the limited depth resolution is a factor hindering the applicability of the technique to ultra-thin films as used in advanced device structures.

In RBS analysis, an ion beam is directed to the sample surface (Figure 1-2). The backscattered ions are detected, and the depth at which the scattering had occurred can be calculated by means of scattering kinematics and stopping powers. The atomic concentrations can be calculated from the backscattering yields according to the Rutherford scattering cross-sections.

The incident ions are detected in backward direction, normally at angles between 150° and 170° with respect to the beam direction. This means that RBS is only sensitive to atoms heavier than the probing beam [2]. As the signal of light elements lies on top of the substrate signal, the sensitivity for elements lighter than the substrate is limited to a few atomic percent.

Most RBS laboratories use ^{4}He incident ion beams in combination with solid state energy detectors. This basic setup allows a simple analysis and is ideal when fast response times are required. Typical beam energies for ^{4}He RBS are between 0.5 and 2.0 MeV. In this energy range, the stopping forces of ^{4}He in many common materials have been exhaustively studied and are well known, thus enabling accurate and widely accepted data quantification. The depth resolution can be improved with the use of glancing geometry, but is still limited to a few nanometers [2].

Two common source/acceleration arrangements are used in commercial RBS systems, working in either one or two stages. One-stage systems consist of a He^+ source connected to an acceleration tube with a high positive potential applied to the ion source, and the ground at the end of the acceleration tube. This arrangement is simple and convenient, but it is difficult to achieve energies of above 1 MeV due to the difficulty of applying very high voltages to the system.

Two stage systems, or ”tandem accelerators”, start with a source of He^- ions and position the positive terminal at the center of the acceleration tube. A stripper element included in the positive terminal removes electrons from ions which pass through, converting He^- ions to He^+ or He^{++} ions.

The ions thus start out being attracted to the terminal, pass through and become positive, and are repelled until they exit the tube at ground. This arrangement, though more complex, has the advantage of achieving higher accelerations with lower applied voltages.

The energy of the backscattered ions is usually measured with Passivated Implanted Planar Silicon (PIPS) detectors, a thin layer of P-type silicon on an N-type substrate forming a p-n junction. Ions reaching the detector lose some of their energy to inelastic scattering with the electrons, and some of these electrons gain enough energy to overcome the band gap between the semiconductor valence and conduction bands. This means that each ion incident on the detector will produce a number of electron-hole pairs dependent on the energy of the ion. These pairs can be detected by applying a voltage across the detector and measuring the current, providing an effective measurement of the ion energy. The relation between ion energy and the number of electron-hole pairs produced will be dependent on the detector materials, the type of ion and the efficiency of the current measurement; the energy resolution is dependent on thermal fluctuations [2].

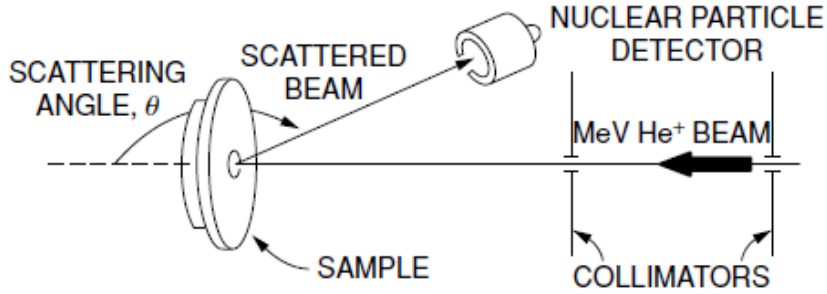

Figure 1-2 RBS schematic. MeV He^+ ion beam hitting the sample surface and scattering at an angle ϑ, where a nuclear particle detector is placed.[6]

While RBS is generally used to measure the elemental composition of a sample, it is also possible to obtain information about the crystalline or amorphous structure of the material by using ion channeling. Channeling of energetic ions occurs when the beam is carefully aligned with a major symmetry direction of a single crystal, such as a crystal axis or plane. In this condition, most of the beam is steered through the channels formed by the string of atoms. Channeled particles cannot get close enough to the atomic nuclei to undergo large angle Rutherford scattering, hence scattering from the substrate is drastically reduced by a factor of ~100.

The depth resolution can be considerably improved with different detection systems, such as time-of-flight and magnetic spectrometers. In case of TOF, in particular, better results can be achieved in combination with heavier beams, thanks to the higher stopping forces for heavier ions. In fact, while the resolution of solid state detectors decreases for heavier ions, time-of-flight telescopes perform well with all ions. Further advantages of heavier beams are improved mass resolution and sensitivity to heavy target atoms.

1.5 Elastic Recoil Detection analysis (ERDA)

Elastic recoil detection analysis is a nuclear technique for the characterization of thin films, providing the sample composition and the elemental depth profiling.

In ERDA, an energetic ion beam is accelerated and focused on a target. The ions interact through Coulomb interaction and the resulting target atoms recoiled in forward direction are detected. The kinematics and the cross-sections of the process, as well as the energy loss of ions in the matter, regulate the quantification and the extraction of depth profiles [**6**].

Forward scattered energetic recoil atoms were used in depth profiling for the first time in 1976, when L'Ecuyer et al. published the results of a study in which they had detected recoils using incident 25-40 MeV ^{35}Cl ions. After more than 30 years, the ERDA methods can now be divided coarsely into two groups: light incident ion ERDA, utilizing low voltage single-ended accelerators, and Heavy incident Ion ERDA (HI-ERDA) which mainly uses large tandem accelerators built originally for nuclear physics research.

ERDA with light incident ions is done using a relatively low energy (~2 MeV) ^{4}He beam, specifically to depth profile hydrogen. In this technique multiple detectors are often used at backscattering angles to detect heavier elements by RBS and a forward detector to simultaneously detect the recoiled hydrogen. The recoil detector has to have a "range foil": a thin film (typically 6 µm of Mylar) to preferentially stop atoms heavier than H, included the incident He beam scattered into the forward direction [**1**].

	Depth resol. (nm)	Sensitivity at./cm^3	Elements	Quantification	Other
SIMS	1-4	$10^{12} - 10^{16}$	All	Semi-quantitative	Surface and interface artifacts, destructive.
AR-XPS	sub-nm	10^{20}	no *H*	Indirect	Surface analysis, limited number of extracted parameters.
AES		10^{20}	no *H*		Surface analysis (< 20nm), high spacial resolution.
RBS	5-10	10^{14}	medium, heavy	Quantitative	Medium and heavy elements, no H.
ERDA	2-5	10^{18}	All	Quantitative	Possible sample damage.

Table 1-1 Comparison of the properties of the most used techniques for 1D elemental profiling. [2]

HI-ERDA is usually equipped with element or mass sensitive detectors, in order to identify the recoiled target atoms and the scattered beam ions. The great advantage in HI-ERDA is that quantitative depth profiling of all the sample atoms can be provided in one measurement [**1**].

A broad variety of ion beams and energies is used in different laboratories, depending on the accelerator facility and the detection system. Typical ions are ^{35}Cl, ^{63}Cu, ^{127}I and ^{197}Au, accelerated at energy up to a few hundred MeV. The most common detection systems are magnetic spectrographs, time-of-flight telescopes or gas ionization detectors.

The performances of the technique depend on the setup and the experimental conditions. Nonetheless, the achievable surface depth resolution is in the order of 1-2 nm, while the sensitivity is better than 0.1 atomic percent for all elements [2].

In HI-ERDA, some factors, such as multiple scattering and ion beam induced damage, have to be taken into consideration. These two processes, less relevant with light projectiles, can affect the data interpretation and the quantification accuracy. In addition, the glancing angles of in-going and out-coming particles make the surface topography related effects important in the interpretation of the results. By including surface topography information into ion beam analysis, a reliable elemental characterization of the surface layers can be obtained [2].

More details about the ERDA basics are given in the next chapter. In this work we studied ERDA performed with low beam energies, 8 MeV ^{35}Cl ion beam.

For our detection system, we used a TOF-E telescope.

2 ERD basics and depth profiling

The aim of an ERD experiment is to perform elemental analysis by detecting the recoil ions in forward directions.

In this chapter Elastic Recoil Detection analysis basics will be presented. We introduce the kinematics of the elastic collision occurring when an ion beam is accelerated towards a target. Furthermore we will analyze recoil energy losses and yield to obtain depth information of the sample. And at the end of the chapter we will present two phenomena which affect depth resolution.

Depth information is conveyed by the energy loss of projectile and recoil ions in the sample whereas the measured yield of recoils with a certain energy reveals the sample composition at a certain depth.

The method offers the advantage of reliable quantification of the results due to well known cross sections and stopping powers. A depth resolution of the order of 1nm can be achieved near the sample surface.

2.1 Collision kinematics

In an ERD experiment recoil ions from binary elastic collisions are analyzed.

A projectile ion of energy E_0 and mass M_1 hits the sample and transfers an amount of energy E_2 to a target atom of mass M_2 during a binary collision (Figure 2-1). Recoil ions are emitted from the sample at recoil angles ϕ (ϕ<90°) in the laboratory frame because of two-body kinematics.

After hitting the target the projectile is backscattered with an energy $E_1 = E_0 - E_2$ and a scattering angle θ.

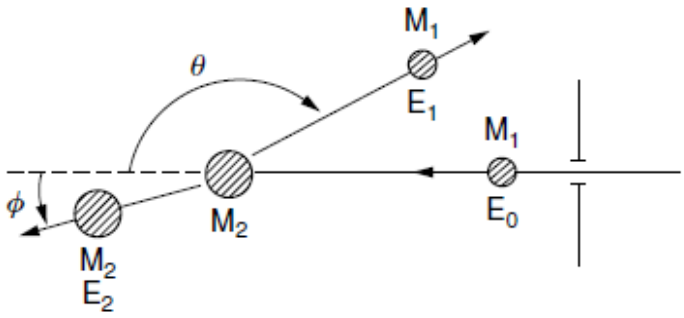

Figure 2-1 – A projectile ion of energy $\boldsymbol{E_0}$ and mass $\boldsymbol{M_1}$ hits the target atom of mass $\boldsymbol{M_2}$ and transfers an amount of energy $\boldsymbol{E_2}$ to it. The target atom is emitted at a recoil angle φ. The projectile is backscattered with an angle ϑ and energy $\boldsymbol{E_1}$. [6]

The energy transfer or kinematics in elastic collisions between two isolated particles can be fully solved by applying the principles of conservation of energy and momentum. For an incident energetic particle of mass M_1 the values of the velocity and energy are v and $E_0(= 1/2\, M_1 v^2)$. The target atom of mass M_2 is at rest.

After the collision the values of the velocities v_1 and v_2 and energies E_1 and E_2 of the projectile and recoil atoms are determined by the scattering angle θ and recoil angle ϕ.

Conservation of energy and momentum parallel and perpendicular to the direction of incidence are expressed by the equations:

$$\frac{1}{2}M_1 v^2 = \frac{1}{2}M_1 v_1^2 + \frac{1}{2}M_2 v_2^2$$

Eq. 2-1

$$M_1 v = M_1 v_1 cos\theta + M_2 v_2 cos\varphi$$

Eq. 2-2

$$0 = M_1 v_1 sin\theta - M_2 v_2 sin\varphi$$

Eq. 2-3

Eliminating φ first and then v_2 from Eq. 2-1, Eq. 2-2 and Eq. 2-3 one finds the ratio of particle velocities:

$$\frac{v_1}{v} = [\frac{\mp(M_2^2 - M_1^2 sin^2\theta)^{1/2} + M_1 cos\theta}{M_2 + M_1}]$$

Eq. 2-4

The projectile energy after collision is

$$E_1 = [\frac{\mp(M_2^2 - M_1^2 sin^2\theta)^{1/2} + M_1 cos\theta}{M_2 + M_1}]^2 E_0$$

Eq. 2-5

The energy ratio, called kinematic scattering factor $K_1 = E_1/E_0$, shows that the energy after scattering is determined only by the masses of the particle and target atom and the scattering angle.

In collisions where $M_1 = M_2$, the incident particle is at rest after the collision, with all the energy transferred to the target atom.

Eliminating θ and then v_1 from Eq. 2-1, Eq. 2-2 and Eq. 2-3 one obtains:

$$E_2 = \frac{4M_1M_2}{(M_1+M_2)^2} cos^2\varphi E_0 = K_2 E_0$$

Eq. 2-6

The energy ratio, called recoil kinematic factor $K_2 = E_2/E_0$, shows that the recoil energy is determined only by the masses of the projectile and target atom and the recoil angle φ.

If $M_1 > M_2$ Eq. 2-5 has two solutions for $\theta < \theta_{max}$ as illustrated in Figure 2-2a (long dashed line). If M1≤M2 the numerator of Eq. 2-5$\mathcal{E}$1=[∓M22−M12sin2θ12+M1cosθM2+M1]2E0 is a sum and it has one solution for $0° < \theta < 90°$ as illustrated in Figure 2-2b.

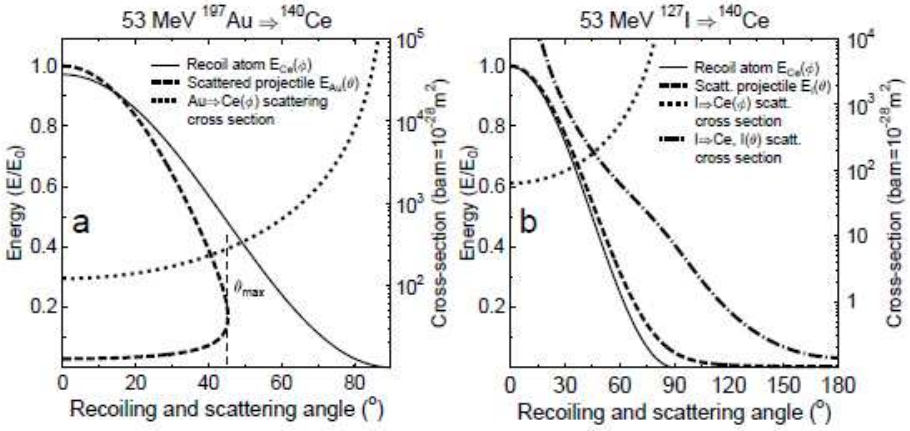

Figure 2-2 Elastic scattering energies and cross-sections of recoil atoms and scattered projectiles as a function of the scattering angle. They are calculated for 53 MeV ^{197}Au hitting on ^{140}Ce (a) and 53 MeV ^{127}I hitting on ^{140}Ce (b). The typical total scattering angle (φ for recoils and θ for incident ions) varies between 35° and 45° . [16]

As long as the projectiles are lighter or not much heavier than the atoms of the layer to be analyzed, the projectiles will also be scattered into the detector.

An elegant method to circumvent this problem is to use projectiles that are much heavier than the main elements in the sample. When $M_1 > M_2$ (Figure 2-2a) the projectiles do not scatter into the detector if the scattering angle θ is chosen to be larger than θ_{max}. θ_{max} is determined by the positive solution of the square root in Eq. 2-5 and:

$$\theta_{max} = arcsin\frac{M_2}{M_1}$$

Eq. 2-7

A change in the recoil angle, $\delta\varphi$, makes a change δE_2 in the recoil-ion energy E_2 according to Eq. 2-6. This change is called the kinematic effect.

The relative change in the recoil energy $\delta E_2/E_2$ is expressed as a Taylor series developed around the mean recoil angle φ and considering the first-order contribution as dominating, as normally used recoil angles are in the range $\varphi \leq 45°$. Thus the relation obtained is:

$$\frac{\delta E_2}{E_2} = -2tan\varphi\delta\varphi$$

Eq. 2-8

[1] [6]

2.2 Ion energy loss in solids

An ion penetrating matter slows down when interacting with the sample atoms, thus reducing its kinetic energy.

The energy loss per unit path length is called stopping force (also stopping power) and it is represented by $S = dE/dx$. The total energy loss for an ion travelling a distance Δx in the material is then

$$\Delta E = \int_o^{\Delta x} S dx = S\Delta x$$

Eq. 2-9

The stopping force is generally known as a function of the energy and is measured in unit eV/10^{15} at./cm^2.

The interaction is usually divided into two separate processes, namely the energy loss in elastic collisions with the nuclei of the sample atoms (nuclear stopping force) and the inelastic collisions with their electrons (electronic stopping force). This classification is mainly derived from ion velocity in comparison to the orbital velocity of the atomic electrons. A schematic of the different stopping force regimes is shown in Figure 2-3.

According to the theory, the maximum of the curve lies in the vicinity of the Thomas-Fermi velocity:

$$v \approx Z_1^{\frac{2}{3}} \frac{e^2}{\hbar}$$

Eq. 2-10

In this regime the electronic stopping force S_e is well described by the Bethe-Block formula:

$$S_e = \frac{4\pi e^2 N Z_1^2 Z_2}{m_e v^2} \ln\left(2m_e v^2 / < I >\right)$$

Eq. 2-11

where Z_1 and Z_2 are the incident and target atomic numbers, respectively; N is the atomic density in the target; m_e is the electronic mass; v is the velocity of the projectile; $< I >$ is the average straggling ionization potential.

At low energies, the stopping force can be approximated by the Lindhard-Scharff-Schiott (LSS) theory as follows

$$S_e = 1.21 * 10^{-16} Z_1^{1/6} \frac{Z_1 Z_2}{(Z_1^{2/3} + Z_2^{2/3})^{3/2}} \frac{1}{\sqrt{M_1[g]}} \sqrt{E_0[eV]}\ [eV * cm^2]$$

Eq. 2-12

where Z_1 and Z_2 are the incident and target atomic numbers respectively, M_1 the incident ion mass and E_0 the projectile energy before the collision. [17]

The positive ion tends to neutralize by electron capture. In this regime the electronic energy loss is approximately proportional to velocity or $\sqrt{E}$.

At very low energies ($v \ll Z_1^{\frac{2}{3}} \frac{e^2}{\hbar}$), the nuclear energy loss is the dominant process. The charge state of the ion increases and finally the ion becomes fully stripped of its outer electrons.

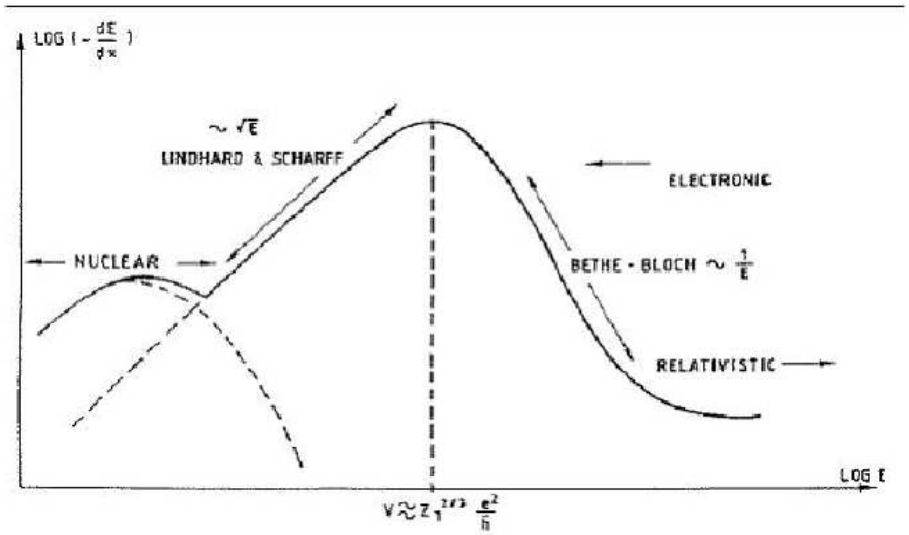

Figure 2-3 Different energy regions of the stopping force curve. In the low-energy limit the fraction of energy loss by nuclear stopping becomes relevant. [2]

In practice, as there is no first-principle theory to calculate stopping forces, experimental results are used to derive semiempirical stopping force tables. The most known parametrization set was created by Ziegler, Biersack and Littmark (ZBL parametrization). According to the ZBL model the stopping force for heavy ions (HI) is derived from the stopping force for protons (S_H) with the same velocity, rescaled with the ion atomic mass Z_{HI}^2 and an effective charge γ_{HI}^2:

$$S_{HI} = S_H Z_{HI}^2 \gamma_{HI}^2$$

Eq. 2-13

The stopping force tables are based on a large number of experimental results. Stopping forces for H and He have been extensively measured over the past decades for single elemental targets, in the energy range of interest for RBS.

Less experimental data are instead available for heavier ions, in particular for projectile energies used in low-energy ERD. The semi-empirical model may thus be less accurate for heavy incident ions or target compounds.

In particular quite critical is the energy region corresponding to the maximum of the stopping force curve, where the error in the predicted values can significantly differ (up to 10-20%) from the actual ones.

Inaccurate stopping forces result in a wrong depth scale conversion and wrong elemental absolute quantification.

In Figure 2-4, we present the Si stopping force for several ions as a function of the ion energy as parametrized in the ZBL tables. The figure also shows the typical energy range used for RBS and low-energy ERD (in the electronic energy loss regime).

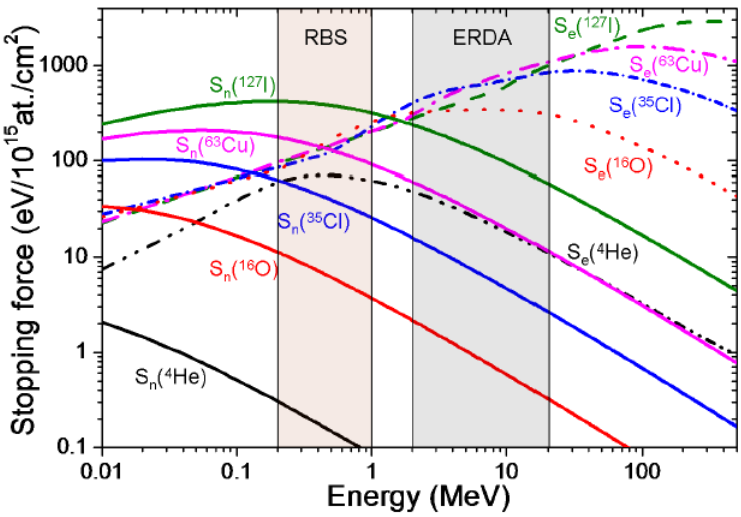

Figure 2-4 Electronic S_e and nuclear S_n stopping force of Si target for several incident ions.[2]

As it can be seen from Figure 2-4 the energy at which the stopping power maximum occurs increases with the atomic number of the incident ion Z_1, as predicted from Eq. 2-10. Both electronic and nuclear stopping forces increase with the ion atomic mass, but below 20MeV the nuclear stopping forces for different ions are quite similar.

The probing depth is directly related to the incident ion mass and energy, the target composition and the scattering geometry.

The surface layers in ion beam analysis mostly contain more than one element. The stopping force of target compounds is calculated assuming the Bragg's rule. The Bragg's rule is a simple linear additivity rule of the stopping contributions of the different compound elements. [2]

For a compound composed of different elements i with atomic concentrations c_i ($\sum c_i = 1$), the total stopping power S is given by

$$S = \sum c_i S_i$$

Eq. 2-14

where S_i is the stopping power of each element. The Bragg's rule assumes that the interaction between the ion and the atom is independent of the surrounding target atoms. The chemical and physical state of the medium were however observed to have a minor effect on the energy loss. [2]

The deviations from Bragg's rule predictions are most pronounced around the stopping power maximum and for solid compounds such as oxides, nitrides and hydrocarbons. In these cases the deviations from Bragg's rule predictions may be of the order of 10-20%. For compounds with heavier atoms the deviations from Bragg's rule is much reduced (<2%). [2]

2.3 Recoil cross-section

In an ERD experiment the identity of target atoms is established by the energy of the recoil particle after an elastic collision.

The number n_i of target atoms per unit area of element i is determined by the probability of a collision between the incident particles and target atoms. This probability is measured by the total number Q_D of detected particles for a given number Q of particles incident on the target.

The connection between the number of target atoms n_i and detected particles is given by the differential cross section of the recoil:

$$Y_i = Q_D = Q n_i x \frac{d\sigma_2}{d\Omega} \delta\Omega$$

Eq. 2-15

where Y_i is the yield of element i ; x is the layer thickness; Ω is the solid angle of the detector and $\frac{d\sigma_2}{d\Omega}$ is the differential cross section for the recoil.

The recoil cross section is derived from Rutherford differential cross section $\frac{d\sigma}{d\Omega}$. Rutherford cross section can be calculated from the force that acts during the collision between the projectile and the target atom.

The nucleus of an atom is a strongly bound system of nucleons located in a small domain with a typical size of

$$R \approx (1.1 - 1.5)A^{1/3} fm$$

Eq. 2-16

where A is the mass number and $fm = 10^{-15}m$.

Nucleons are held together inside nuclei by nuclear forces. These forces are strong attractive forces acting only at short distances. The short range of strong nuclear forces leads to a strict demarcation between the regions where only long-range repulsive Coulomb forces or only nuclear forces operate. Nuclear forces are at least 100 times greater than Coulomb forces at short distances of about 1fm.

In the region of Coulomb forces during the collision it arises an unscreened Coulomb repulsion of two positively charged nuclei, the projectile and target atoms.

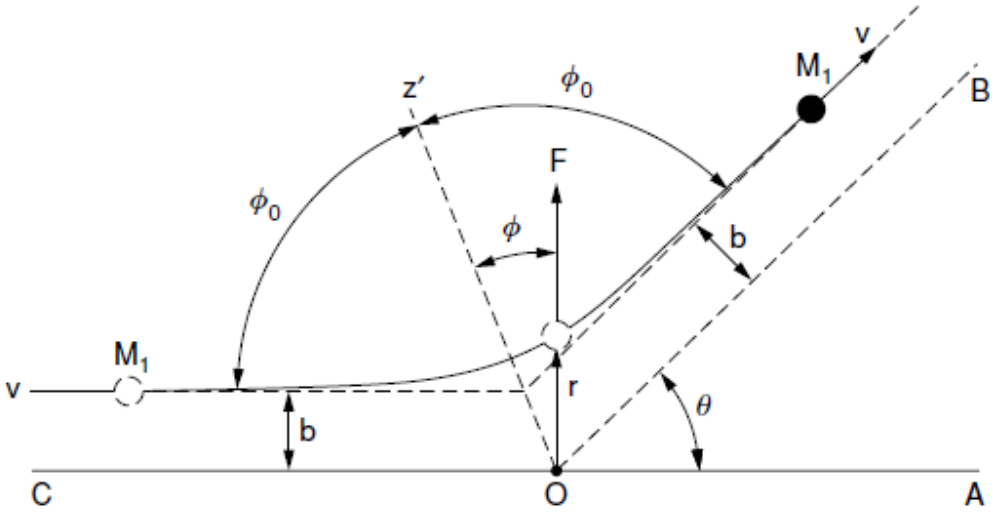

Figure 2-5 Rutherford scattering geometry.The target nucleus is assumed to be a point charge at the origin O. At any distance r, the particle experiences a repulsive force. The scattered ion travels along a hyperbolic path. [6]

As shown in Figure 2-5 we can define the impact parameter b as the perpendicular distance between the incident particle path and the parallel line through the target nucleus. Particles

incident with impact parameters between b and $b + db$ will be scattered through angles between θ and $\theta + d\theta$. Scattered particles are detected in a solid angle $d\Omega$

$$d\Omega = 2\pi sin\theta \, d\theta$$

Eq. 2-17

The relative number of particles scattered into the solid angle $d\Omega$ is equal to the area of the ring with radii b and $b + db$ surrounding the scattering center

$$d\sigma = \frac{dN}{N} = 2\pi b \, db$$

Eq. 2-18

Combining Eq. 2-17 and Eq. 2-18, we obtain the differential cross section expressed as a function of b

$$\frac{d\sigma}{d\Omega} = \frac{b}{sin\theta}\frac{db}{d\theta}$$

Eq. 2-19

As the projectile with charge $Z_1 e$ approaches the target atom with charge $Z_2 e$ it will experience a repulsive force that will cause its trajectory to deviate from the incident straight line path. The value of the Coulomb force F at a distance r is given by

$$F = \frac{Z_1 Z_2 e^2}{4\pi\epsilon_0 r^2}$$

Eq. 2-20

Let p_1 and p_2 be the initial and final momentum vectors of the projectile. The total change in momentum $\Delta p = p_1 - p_2$ is along the z' axis (Figure 2-6). The magnitude of the momentum does not change before and after the impact.

From the isosceles triangle formed by p_1, p_2 and Δp shown in Figure 2-6 we have:

$$\frac{1/2\,\Delta p}{M_1 v} = sin\frac{\theta}{2} \quad \rightarrow \quad \Delta p = 2M_1 v sin\frac{\theta}{2}$$

Eq. 2-21

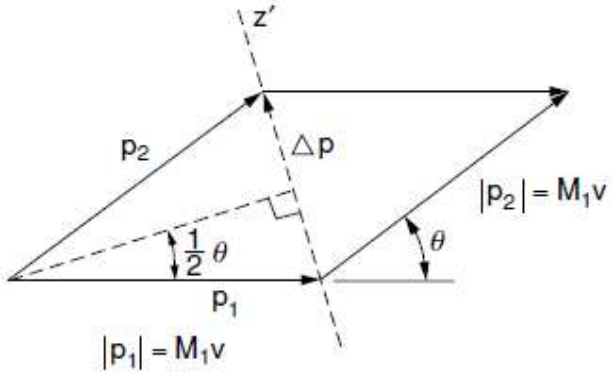

Figure 2-6 Momentum diagram for Rutherford scattering. [6]

We now write Newton's law for the particle:

$$dp = F\,dt$$

The force F is given by Coulomb's law and it is in the radial direction. Taking components along z' direction, and integrating to obtain Δp we have

$$\Delta p = \int (dp)_{z'} = \int F cos\Phi\, dt = \int F cos\Phi\, \frac{dt}{d\Phi}\, d\Phi$$

Eq. 2-22

where we have changed the variable of integration from t to the angle Φ between the z' axis and the force F (Figure 2-5).

Since there is no torque about the origin, the angular momentum of the particle is conserved. Thus we have:

$$M_1 r^2 \frac{d\Phi}{dt} = M_1 vb \;\rightarrow\; \frac{dt}{d\Phi} = \frac{r^2}{vb}$$

Eq. 2-23

Substituting Eq. 2-23 and Eq. 2-20 in Eq. 2-22 we obtain

$$\Delta p = \frac{Z_1 Z_2 e^2}{4\pi\epsilon_0 r^2} \int cos\Phi\, \frac{r^2}{vb}\, d\Phi = \frac{Z_1 Z_2 e^2}{4\pi\epsilon_0 vb} \int cos\Phi\, d\Phi = \frac{Z_1 Z_2 e^2}{4\pi\epsilon_0 vb} (sin\Phi_2 - sin\Phi_1)$$

Eq. 2-24

where $\Phi_1 = -\Phi_0$ and $\Phi_2 = +\Phi_0$ with $2\Phi_0 + \theta = 180°$. Then $sin\Phi_2 - sin\Phi_1 = 2\sin(90° - \frac{1}{2}\theta)$.

Equating Eq. 2-24 with Eq. 2-21 we can extract the impact parameter as

$$b = \frac{Z_1 Z_2 e^2}{8\pi\epsilon_0 E} cot\frac{\theta}{2}$$

Eq. 2-25

Then from Eq. 2-19 and Eq. 2-25:

$$\frac{d\sigma}{d\Omega} = \frac{b}{sin\theta}\frac{db}{d\theta} = (\frac{Z_1 Z_2 e^2}{8\pi\epsilon_0 E})^2 \frac{1}{sin^4\,\theta/2}$$

Eq. 2-26

This is the differential cross section originally derived by Rutherford.

The differential cross-section for scattered ions is derived from Rutherford cross-section as follows. Eq. 2-26 was based on the one-body problem of the projectile scattering by a fixed center of force. However, the second particle is not fixed but recoils from its initial position as a result of the scattering.

In general the two-body central force problem can be reduced to a one-body problem by replacing M_1 by the reduced mass $\mu = M_1 M_2/(M_1 + M_2)$ from Eq. 2-21 up to now.

It follows that the cross-section for scattered ions is:

$$\frac{d\sigma_1}{d\Omega} = (\frac{Z_1 Z_2 e^2}{8\pi\epsilon_0 E_0})^2 \frac{(\sqrt{M_2^2 - M_1^2 sin^2\theta} \pm M_2 cos\theta)^2}{M_2 sin^4\theta\sqrt{M_2^2 - M_1^2 sin^2\theta}}$$

Eq. 2-27

From the energy conservation law $E_0 = E_1 + E_2$, substituting for E_1 and E_2 Eq. 2-5 and Eq. 2-6 respectively we get the relation between scattered and recoil angles, respectively θ and φ:

$$cos^2\varphi = \frac{(M_1 + M_2)^2 - (\sqrt{M_2^2 - M_1^2 sin^2\theta} \pm M_1 cos\theta)^2}{4M_1 M_2}$$

Eq. 2-28

Combining Eq. 2-27 and Eq. 2-28 it is possible to derive the cross-section for recoil atoms. In the laboratory coordinates it is expressed as:

$$\frac{d\sigma_2}{d\Omega} = (\frac{Z_1 Z_2 e^2}{8\pi\epsilon_0 E_0})^2 \frac{(1 + M_1/M_2)^2}{cos^3\varphi}$$

Eq. 2-29

Several specific characteristics of the recoil cross sections as given by Eq. 2-29 can be identified:

a) The cross section increases with recoil angle φ according to $1/cos^3\varphi$ dependence. This increase in cross section is accompanied by a decrease in recoil-ion energy E_2 that is proportional to $cos^2\varphi$ according to Eq. 2-6.
b) In the case of projectiles that are much heavier than the recoil ions ($M_1 > M_2$), the cross section scales as $\sigma_2 \propto {Z_1}^2(M_1 + M_2)^2 \propto {Z_1}^4$ using the same projectile energies or as $\sigma_2 \propto {Z_1}^2$ when the ion velocity, and thus the specific energy E_0/M_1 is kept constant.
c) The cross section is nearly constant for all recoil ions that are much lighter than the projectile ($M_1 \gg M_2$). The only exception is hydrogen, which has a cross section enhanced by almost a factor 4 compared to those of other light elements. This is because $Z_2/A_2 = 1$ in the case of hydrogen compared to $Z_2/A_2 = 1/2$ for the other elements.

Eq. 2-29 only holds where only long-range Coulomb forces operate. If the ions overcome the Coulomb barrier, then strong nuclear interactions dominate the cross sections and the Eq. 2-29 no longer holds true.

The threshold energy E_{Thres} below which only Coulomb forces operate is:

$$E_{Thres} = (1 + M_1/M_2)\frac{Z_1 Z_2 e^2}{4\pi\epsilon_0 R_0}$$

Eq. 2-30

where R_0 is the safe minimum distance of closest approach between projectile and recoil expressed as $R_0 = \left[1.25(A_1^{1/3} + A_2^{1/3}) + 5\right]fm$ where pure Coulomb scattering occurs.

At large projectile energies one must rely on experimental or theoretical values for the elastic recoil cross section. [6]

2.4 Depth profiling algorithm

For a quantitative depth profile an energy spectrum is required for each element which appears in significant concentration in the sample. To extract the depth profiles from the energy spectra one needs the energy depth relationship for each isotope or element.

During scattering at depth $\bar{x}$ a portion K_2 of the projectile energy $E_0(\bar{x})$ is transferred to the recoil atom according to Eq. 2-6.

For a recoil atom of type i scattered at a certain depth $\bar{x}$ underneath the surface, the detected energy of the recoil is written as

$$E_i^{det}(\bar{x}) = K_2\left\{E_0 - \int_0^{\bar{x}}\sum_{i=1}^{m}\left[n_i(x')\frac{S_{1i}(x')}{sin\alpha}\right]dx'\right\} - \int_0^{\bar{x}}\sum_{i=1}^{m}\left[n_i(x')\frac{S_{2i}(x')}{sin\beta}\right]dx' - \int_0^{L} S_0(x')dx' =$$

$$= K_2[E_0 - A(S_{1i}(\bar{x}))] - B(S_{2i}(\bar{x})) - C(S_0(\bar{x}))$$

Eq. 2-31

where α and β are respectively the incident and recoil angle with respect to the sample surface.

The first term $K_2[E_0 - A(S_{1i}(\bar{x}))]$ calculates the recoil energy directly after the scattering event by using the projectile energy reduced by the energy loss of the projectile in the sample up to thickness $\bar{x}$, weighted by the kinematic factor.

The second term $B(S_{2i}(\bar{x}))$ describes the energy loss of the recoil ion on its way back to the surface. The third term, $C(S_0(\bar{x}))$, is the contribution of the foil in front of the detector, thus $S_0(\bar{x})$ is the energy loss in the foil.

Dividing Eq. 2-15 by Eq. 2-31 leads to a system of m linear equations for the concentrations $n_i(\bar{x})$ of m elements in depth $\bar{x}$:

$$\frac{Y_i}{E_i^{det}(\bar{x})} = \frac{Q n_i x \frac{d\sigma_2}{d\Omega} \delta\Omega}{K_2[E_0 - A(S_{1i}(\bar{x}))] - B(S_{2i}(\bar{x})) - C(S_0(\bar{x}))}$$

Eq. 2-32

This system of linear equations would have a nontrivial solution if all the input parameters were accurately known.

But in reality they are submitted to statistical and systematic errors, thus the system is over-determined. Nevertheless an approximate solution can still be obtained at each depth $\bar{x}$ by a so called inverse iteration, if one parameter is left adjustable.

The natural choice is the beam dose Q since it contains the least information and is difficult to determine.

A suitable starting value for the inverse iteration is obtained by taking the concentrations n_i in the same ratio as the corresponding normalized yields $Y_i/E_i^{det}(\bar{x})$ divided by their differential cross-section $(d\sigma_2/d\Omega)_i$.

The concentration profile of the sample is now calculated iteratively from the surface to larger depths. The energy losses for the calculation of $E_i^{det}(\bar{x})$ in the ERDA spectrum of element i that pertains to the depth $\bar{x}$ is thereby obtained from the concentrations n_i that have been calculated for the previous depth interval $\bar{x} - \Delta x$. [7]

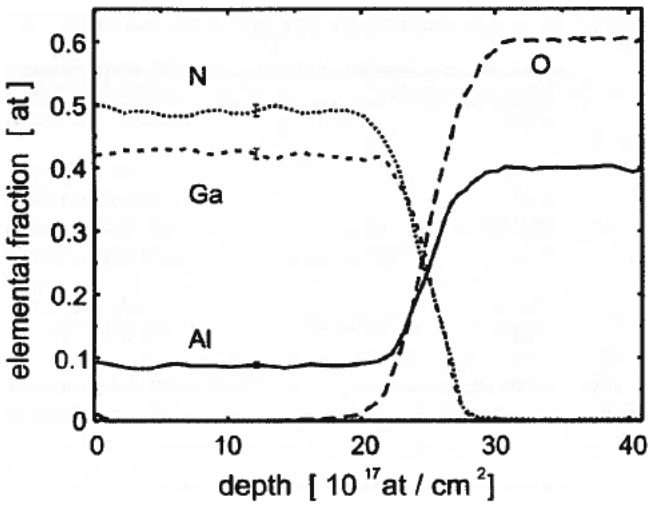

Figure 2-7 Elemental depth profiles as obtained from the recoils for a 200nm-thick $Al_xGa_{1-x}N$ layer deposited on Al_2O_3 substrate. [1]

2.5 Depth resolution

The deceleration of the projectiles on their way into the sample and of the recoil ions on their way out of the sample converts into an energy-depth relationship. The depth resolution δx is therefore directly related to the total energy resolution δE_i, and to the shift dE_i^{det} of the detected energy of recoil ions of type i obtained for a layer of thickness dx:

$$\delta x = \frac{\delta E_i}{dE_i^{det}/dx}$$

Eq. 2-33

The term δE_i is obtained from:

$$\frac{\delta E_i}{E_i} = \sqrt{\sum_j (\frac{\delta E}{E})_j^2}$$

Eq. 2-34

where $(\frac{\delta E}{E})_j$ are the contributions to the relative energy spread for recoil atoms of type i.

Apart from the detector resolution, among the others the major contributions to the relative energy spread are energy straggling and multiple scattering. We will analyze these contributions in this chapter.

2.5.1 Energy straggling

An energetic particle that moves through a medium loses energy via many individual encounters. Such a discrete process is subject to statistical fluctuations. As a result identical energetic particles, which have the same initial velocity, do not have exactly the same energy after passing through a

thickness Δx of a homogeneous medium. The energy loss ΔE is subject to fluctuations δE. This phenomenon is called 'energy straggling'. [6]

Energy straggling is one of the main limits for depth resolution in depth profiling. The straggling contribution to Eq. 2-34 can be approximated by Bohr straggling at high energies and by additional correction factors for low ion energies. It can be expressed as:

$$(\frac{\delta E(x)}{E})_{stragg} = \frac{\sqrt{8ln2}}{E}\frac{e^2}{4\pi\varepsilon_0}\sqrt{4\pi Z_2 \frac{N}{V} x[\frac{W_1^2 Z_1^2}{sin\alpha} + \frac{W_2^2 Z_2^2}{sin\beta}]}$$

Eq. 2-35

where Z_1 and Z_2 are the average nuclear charge of the projectile and target respectively and N/V is the atomic density in the target. Factors W_1 and W_2 correct the Bohr straggling at low energies. These factors cannot currently be calculated accurately for heavy ions at low ion energies, thus semiempirical values are used. [1]

2.5.2 Multiple scattering

Particles on the ingoing and outgoing path undergo numerous small angle scattering events with the sample nuclei. This process is called 'multiple scattering' and it generates an ion angular distribution around the original trajectory.

Additionally ions may perform more than one scattering event with large scattering angle before they are scattered towards the detector (Figure 2-8). This has been called 'plural scattering'. Although these events are scarce, they can play an important role in the analysis.

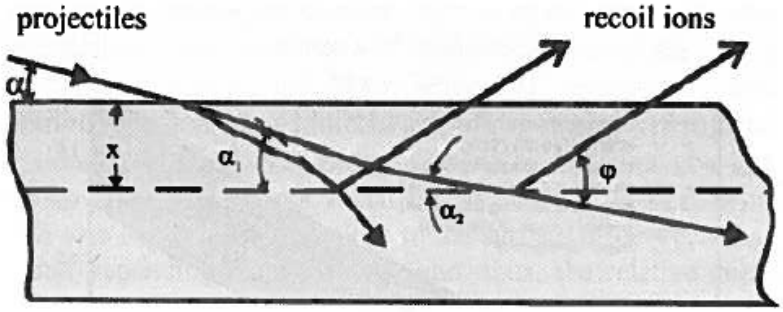

Figure 2-8 Sketch of multiple scattering effects. [1]

Due to the particles angular spread, the original unambiguous measurement geometry is no longer valid. Multiple and plural scattering result indeed in a spread both of the path lengths and of the scattering angle. The former generates spreading in energy (and also in the energy straggling) for ions at a given depth. The spread in scattering angle has instead consequences both for the kinematics and the cross sections associated to the total scattering process.

Multiple scattering has been studied and a model has been proposed, which describes the angular spread distribution. Plural scattering instead cannot be treated analytically but only with simulations. [2]

3 Experimental methodology

In this chapter we will describe two methodologies to perform ERD experiments with their respective properties, advantages and disadvantages.

Furthermore the IMEC setup for ERDA will be introduced, and its performance figures will be listed.

3.1 ΔE-E analysis

The full potential of ERD analysis is obtained when the elemental analysis is performed independently from the depth analysis. In addition to the energy of the recoil ions, one needs a second independent signal to separate the elemental information from the depth information.

A quite simple solution is to use a ΔE-E setup, where an energy-loss signal is gained from the recoil ions using a thin transmission detector in coincidence with the signal of a second detector that is placed directly behind it in order to measure the residual energy. Adding the energy-loss and residual-energy signals gives the total energy of the detected ions.

If the ΔE signal is plotted as a function of the total energy, the different elements are separated from each other because of their different energy-loss signals for a given total energy [1]. An example of a ΔE-E measurement using a detector where the ΔE part consists of a gas ionization chamber and the residual energy, E_{res}, is measured by a silicon detector is shown in .

The analyzed sample was an approximately 200nm-thick $Al_xGa_{1-x}N$ layer deposited on Al_2O_3. It was analyzed using a 170 MeV ^{127}I beam, a scattering angle of φ~40°, and an incident angle of α=15°.

The energy loss, ΔE, is plotted as a function of the total energy E_{tot}, which is the sum of ΔE and E_{res}.

It is shown in Figure 3-1 that all light and medium-heavy elements, including hydrogen (Figure 3-1 insert), are well separated and identified. The potential of elemental separation can be estimated directly from the energy losses of the various elements at a given energy. The separation works efficiently even for various isotopes of the same element when the total energy is beyond the stopping-loss maximum.

When the total energy is low and the energy-loss differences are smaller than the ΔE resolution, elemental separation from the energy-loss signal is hardly possible, with the exception of hydrogen.

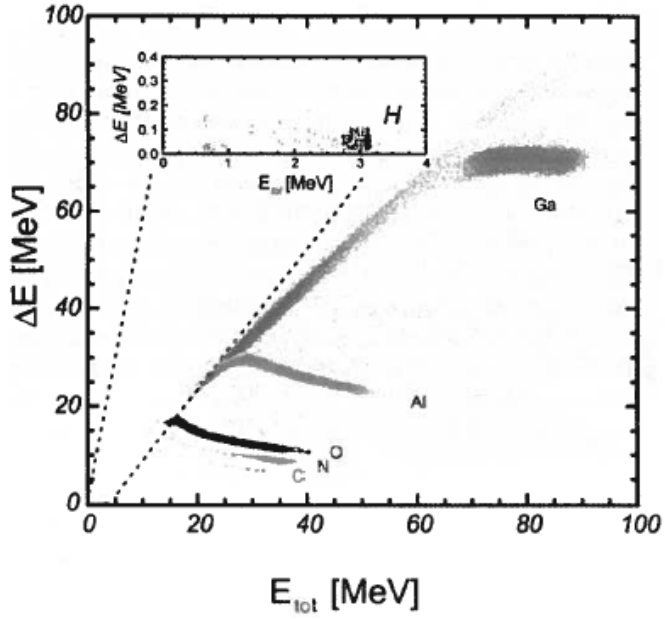

Figure 3-1 $\boldsymbol{\Delta E - E}$ *spectrum of a 200nm-thick* $Al_xGa_{1-x}N$ *layer deposited on* Al_2O_3 *substrate obtained using a 170 MeV* ^{127}I *beam, a scattering angle of* φ*~40°. The* $\boldsymbol{\Delta E}$ *part was measured using a gas ionization chamber and the residual energy was measured using a silicon detector. [1]*

There are several ways to set up $\Delta E - E$ detectors. A straightforward solution is to combine two solid state detectors, one behind the other, where the first one is a thin silicon detector (Figure 3-2a) [1].

Although these detectors are simple to handle, they have disadvantages. The first one is the low energy resolution of the ΔE detector, because of the large noise level of such a thin silicon detector. The second disadvantage is the sensitivity of these detectors to radiation damage.

Better performance has been demonstrated using gas ionization chamber detectors (Figure 3-2b), where the anode is divided into two consecutive stripes [1]. The electrons in the detector are allowed to drift transversally to the impinging recoil ions in order to obtain a ΔE and a residual energy signal.

A Frisch grid configuration, a grid made of a conductive material that is typically placed between the cathode and anode in ionization chamber detectors, makes the energy signal independent of the ion position where the ions enter the detector [1].

Ionization chambers offer reasonable energy resolution for light ions (protons and He). For ions heavier than lithium, gas ionization chambers even outperform silicon detectors, in terms of energy resolution. In addition, these detectors do not suffer from irradiation damage if the detector gas is routinely changed.

The disadvantage of gas ionization chamber detectors is that they are not commercially available but rather have to be set up by each group itself. Another disadvantage is that the length of the detectors is limited.

A general limit of the $\Delta E - E$ technique is the minimum energy required to separate the various recoil ions through their specific energy loss. Although separation of hydrogen isotopes is possible even at very low ion energies, other detectors have to be used to obtain elemental or mass information of the recoil ions at lower energies. [1].

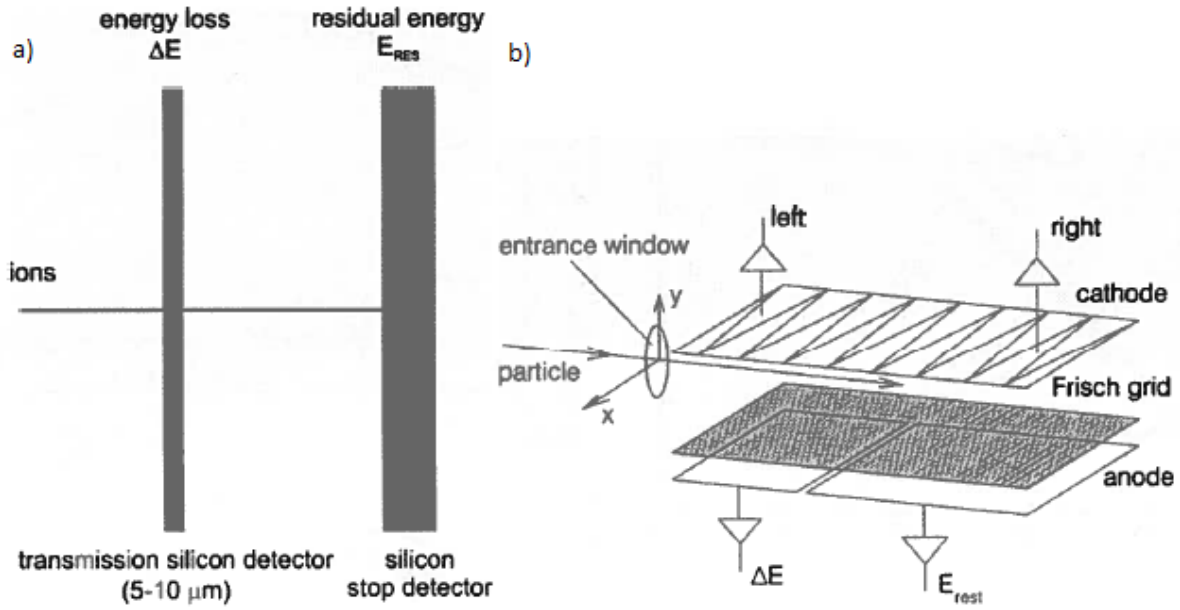

Figure 3-2 Two $\boldsymbol{\Delta E - E}$ detector setups for elemental analysis in ERDA. a) Schematics for all solid state detectors for $\boldsymbol{\Delta E}$ and E measurements. b) Electrode configuration of an $\boldsymbol{\Delta E - E}$ ionization chamber. The Frisch grid makes the anode signal independent of the position of the ion track. [1]

3.2 TOF – E analysis

A second widely used method for recoil-ion identification is to analyze the mass of the recoil ions by measuring their energy E_2 and velocity v_2 independently:

$$M_2 = \frac{2E_2}{v_2^2} = 2E_2\left(\frac{TOF}{L}\right)^2$$

Eq. 3-1

Whereas the energy measurement can be performed by either a solid state detector or an ionization chamber, the velocity of the ions is measured by the time of flight of the recoils (TOF) through a defined flight path L (Figure 3-3a). In Figure 3-3b are shown TOF plots as a function of the recoil energies, both in channel units.

This method can especially be used at recoil ion low energies, where the $\Delta E - E$ technique is no longer useful. Although the principle seems to be relatively simple, the TOF-E method requires sophisticated detectors to achieve its full potential.

The first challenge is to measure the TOF of the ions accurately, because mass resolution δM_2 depends on both TOF resolution and E resolution:

$$\frac{\delta M_2}{M_2} = \sqrt{(\frac{\delta E_2}{E_2})^2 + 2(\frac{\delta TOF_2}{TOF_2})^2}$$

Eq. 3-2

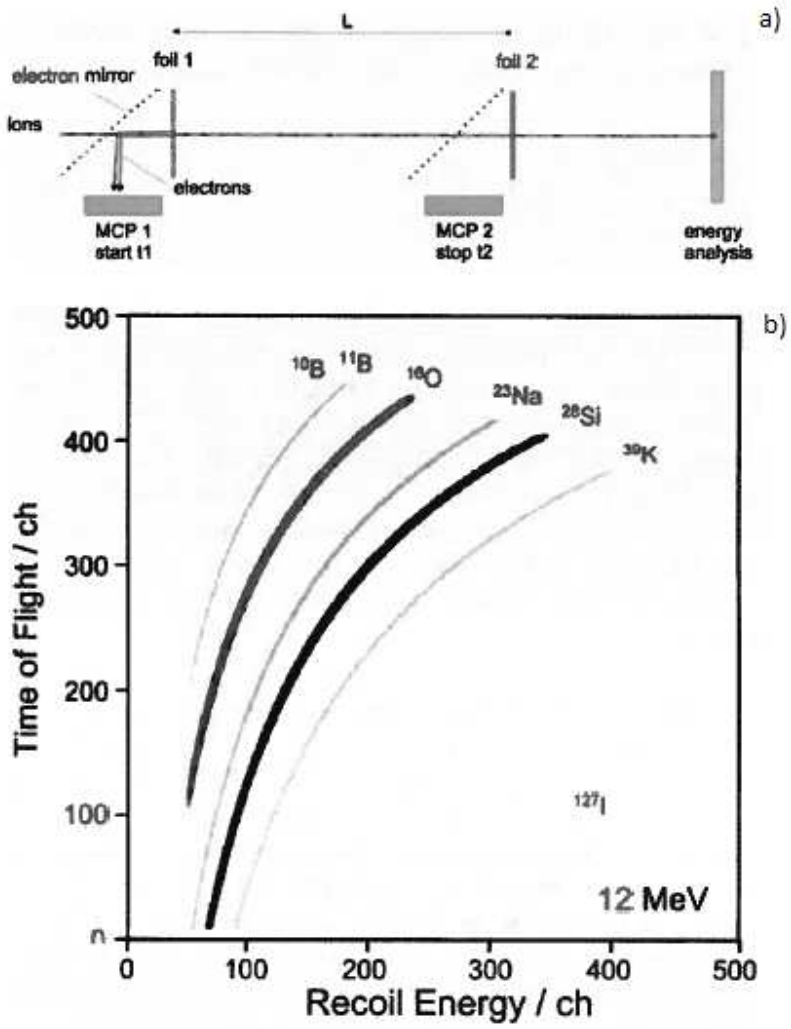

Figure 3-3 a) Start and stop configuration for TOF measurement that allows high TOF resolution. Secondary electrons that are generated in thin foils are used to start and stop signals at the beginning and end of a flight path L. b) Example of a TOF-E ERD analysis. [1]

According to Eq. 3-2 one must obtain a relative TOF resolution better than $\delta TOF_2/TOF_2 < 0.5\%$ and an energy resolution of slightly less in order to obtain a mass resolution better than 1/100.

Two methods have been used to measure TOF. The first is to use a pulsed beam and a silicon energy detector simultaneously to create a fast timing signal. The signal from the detection is used as a start pulse for timing electronics (TAC, TDC), and a signal correlated to the beam pulse is used as a stop pulse.

TOF can be deduced from this time difference Δt as $TOF = t_0 - \Delta t$, for an arbitrary constant t_0.

Typically the overall time resolution achieved by a pulsed-beam system is no better than 0.5ns. This is sufficient to separate hydrogen isotopes and the light recoil ions, but it has limited sensitivity and mass resolution for heavier elements.

The other widely used method to obtain TOF data is based on separate start and stop detectors that each consist of a thin foil that creates a secondary electron pulse when an ion is transmitted through the foil (Figure 3-3a). The secondary electrons are accelerated by a grid close to the foil and led to a secondary-electron detector, in most cases a microchannel plate detector, MCP, as shown in Figure 3-3a.

Microchannel plates, MCP, are made of highly resistive channels, also called pores (Figure 3-4). A single secondary electron enters a channel and emits an electron from the channel wall. Both the input electron and the generated one are accelerated by an electric field developed by a voltage applied across the both ends of the MCP. They travel along their trajectories until they in turn strike the channel surface, thus producing more secondary electrons. This process is repeated many times along the channel (Figure 3-4).

As a result, this cascade process yields a cloud of several thousand electrons, which emerge from the rear of the plate [25]. The generated current is collected from an underlying anode.

Most modern MCP detectors consist of two microchannel plates with angled channels rotated 180° from each other producing a Chevron (v-like) shape (Figure 3-5 right). In a chevron MCP the electrons that exit the first plate start the cascade in the next plate. The advantage of the Chevron MCP over the straight channel MCP is significantly more gain at a given voltage [26].

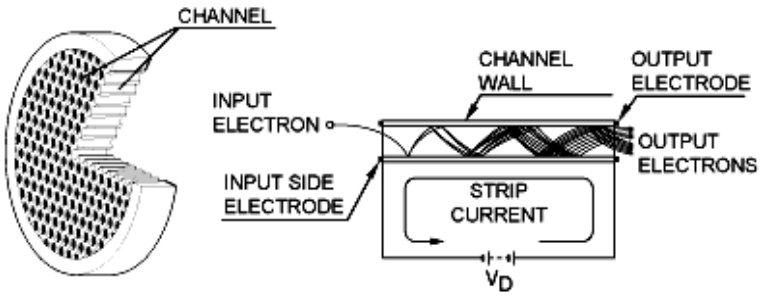

Figure 3-4 Schematic view of a microchannel plate. On the right a cross section of a channel is shown [25].

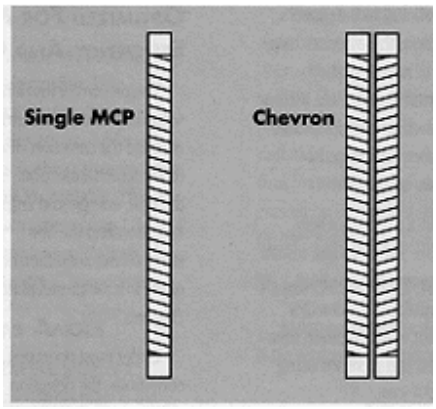

Figure 3-5 On the left the cross section of a single MCP. On the right the cross section of a Chevron type MCP [27].

To avoid large time spreads due to fast electrons that stem from forward-scattered electrons at the exit side of the foil, one can use the electrons emitted from the entrance side.

The number of electrons emitted depends on the foil material, thickness and the electronic stopping loss of the ions. The electron yield is normally greater than unity for all ions except high-energy hydrogen ions.

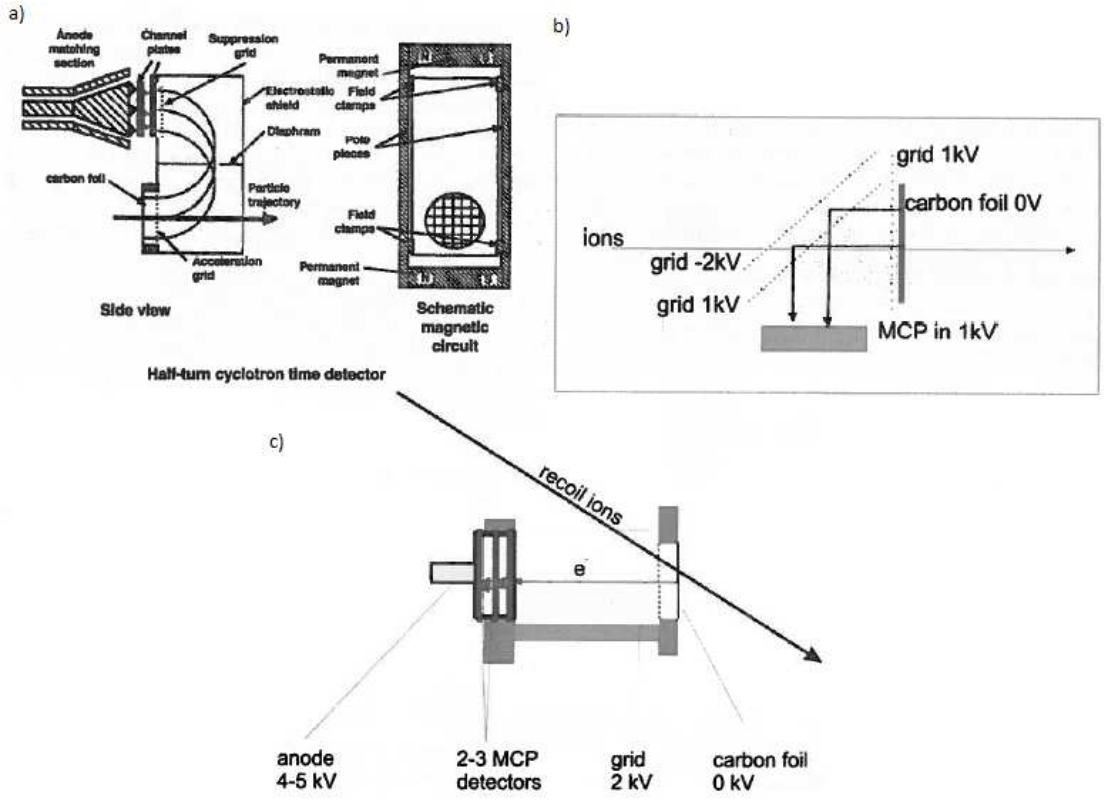

Figure 3-6 Various configurations to deflect secondary electrons out of the ion path. a) 180° magnetic field detector, b) electrostatic mirror configuration consisting of electrostatic grids, c) tilted configuration with 0° electron detection. [1]

Several configurations are used to direct the secondary electrons from the beam direction onto the channel plate:

a) The secondary electrons are guided in a homogeneous magnetic field and deflected 180° onto the MCP (Figure 3-6a).
b) The secondary electrons are reflected by an electrostatic mirror onto the MCP (Figure 3-6b).
c) The thin foil traversed by the recoil ions is tilted by a certain angle (Figure 3-6c). Thus the electrons can be accelerated perpendicularly from the foil, reaching the MCP outside the beam direction.

Method b) is probably the most widely used, although the most compact method is c). A disadvantage of method c) is that the effective foil thickness increases because of the tilt.

In most cases thin carbon foils are used as secondary-electron emitters because they can be produced thinnest with respect to energy loss, energy-loss straggling, and angular scattering effects. The thinnest give minimized energy straggling and are used for high resolution work. [1]

3.3 Experimental setup in IMEC

The TOF-ERDA setup was installed in IMEC parallel to the RBS setup, using its ion source and accelerator.

The latest setup was built up in December 2013, on the model of Jyväskylä University setup [24].

The setup consists of a sputtering negative ion source (SNICS) from NEC, which can be typically switched between alpha particles, chlorine or copper ions. Then we have a 1.6MeV accelerator, a sample chamber, on top of which a goniometer is mounted, and a telescope. Typical vacuum conditions in the scattering chamber during the measurements are 1×10^{-8} mbar.

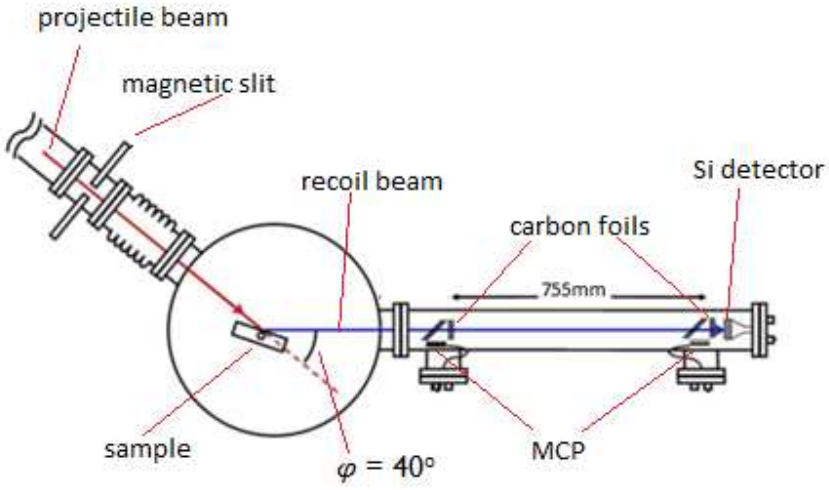

Figure 3-7 Schematic view of the TOF-E spectrometer in IMEC. [2]

Just before hitting the sample the ion beam is collimated thanks to magnetic slits positioned in the proximity of the sample chamber (Figure 3-7). The goniometer is used to rotate the sample holder in order to choose the incidence angle.

In the telescope we have two timing gates (Figure 3-8), T1 and T2, each made of a carbon foil, an electrostatic mirror, an MCP and an anode. The two timing gates are spaced from a fixed distance L of 755.4mm.

In each timing gate recoils exiting the sample hit the carbon foil, secondary electrons are created in the carbon foil from which they are emitted by the traversing ion.[14] Later the secondary electrons are bended thanks to an electrostatic mirror, they are multiplied by the MCP and collected by the anode underlying the MCP.

The signal collected by each anode, called timing signal, is then processed by the electronics. T1 timing signal is used as start pulse, T2 timing signal is used as stop pulse.

We define Time of Flight (TOF) as the time for a recoil atom to travel the fixed distance L between the two timing gates. Thus the TOF is the time between the start and stop pulses generated by T1 and T2.

At the end of the telescope is positioned a silicon detector, it records the energy signal of recoils. The silicon detector measures in arbitrary unit the energy channel of a recoil. Energy channel is the response of the Si detector to the arrival of a recoil. This is not necessarily linear either with mass or energy (see Section 4.3), so the unit of energy is not valid for the energy channel quantity.

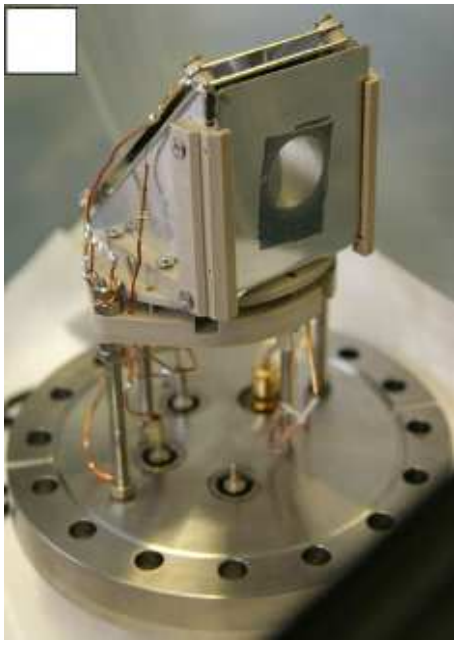

Figure 3-8 T2 timing gate with diameter 18 mm.T1 timing gate has a diameter of 7 mm. [14] [15]

The foil in the T1 has density of 5.0 μg/cm^2 and foil voltage of -500V (Figure 3-9a), while the carbon foil in the T2 has density of 9.0 μg/cm^2 and foil voltage of -3kV (Figure 3-9b).

Both timing gates have the same effective diameter (~ 40 mm) Chevron-type MCPs supplied by Tectra Gmbh with pore size 12 µm (Figure 3-10) [15]. The difference between the two MCPs is voltage: +2600 V for T1 MCP (Figure 3-9a) and -1850 V for T2 MCP (Figure 3-9b).

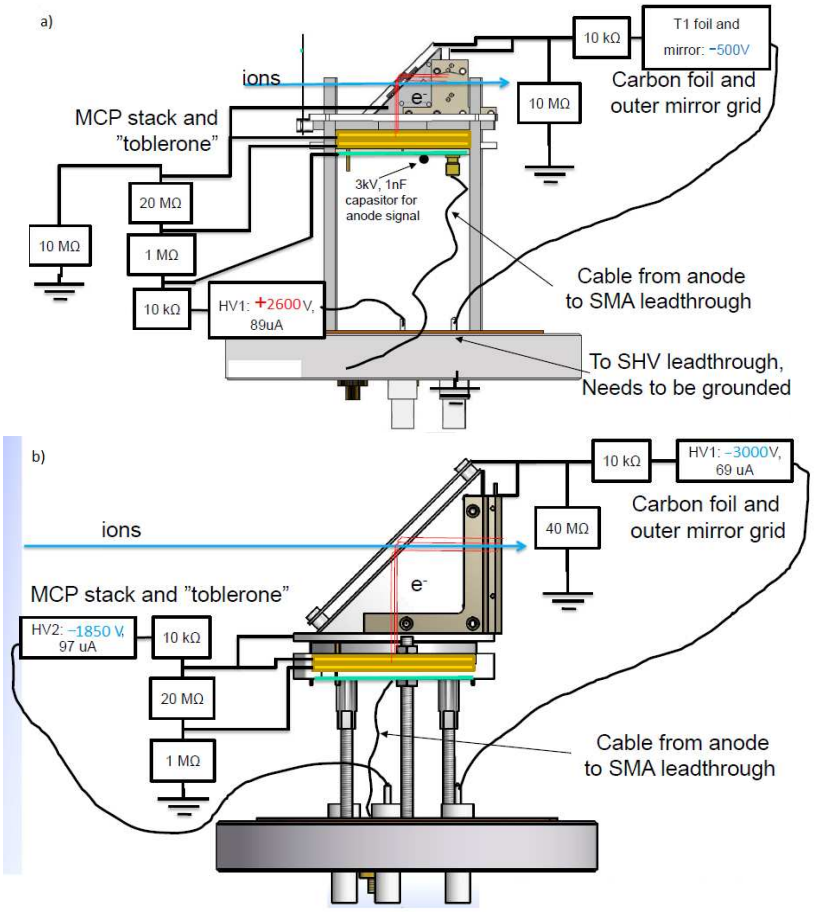

Figure 3-9 Resistor/voltage configuration of a) T1 timing gate b) T2 timing gate [15].

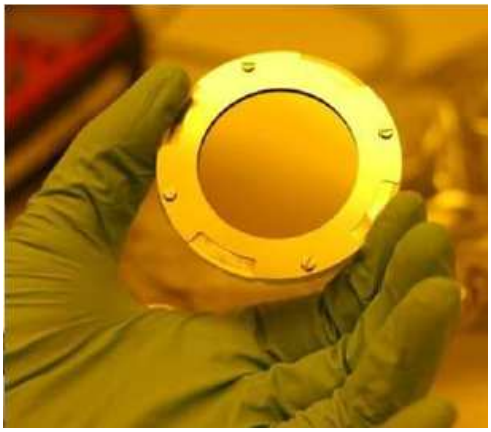

Figure 3-10 MCP by Tectra Gmbh. It has active diameter >40 mm, pore size 12 µm, channel length/diameter 40:1. [15]

Carbon foils and MCP voltages were set similar to Jyväskylä University setup voltages [24]. Originally the voltages of the both timing gates were identical (similar to current T2) but the operation voltages of the first timing gate were afterwards changed in order to minimize the possible tandem effect [24].

The tandem effect can generally be described as a time-of-flight spread due to the charge state exchange of the passing ion in the carbon foil of the first timing gate [28].

Both T1 and T2 have an electrostatic mirror (Figure 3-11) made out of 25 μm or smaller diameter gold plated W wire. 1.0 mm wire-to-wire spacing was chosen as this combination was proven to be feasible and well per-forming in the similar timing detectors.[14]

Figure 3-11 Electrostatic mirror grid: Spot-welded 25 μm diameter Au plated W wire; wire-to-wire distance 1 mm. [15]

The energy detector used during this thesis work is a silicon detector, it was installed on December 06th, 2013. It was supplied by ORTEC, its active area is 450 mm^2 and alpha particles resolution less than 17keV.

Conventional analog electronics was used for signal amplification and discrimination for the two timing detectors and for the energy detector.

For the energy detector, an Ortec 142 preamplifier was coupled to a shaping amplifier and further connected to an ADC (analog to digital converter) unit.[14]

For the timing detectors a Phillips Scientific 775 amplifier with a gain of 10, bandwidth from 100 KHz to 1.8 GHz was used for the fast timing signals pre-amplification. [15] Amplified timing signals

were fed to an Ortec 935 constant fraction discriminator (CFD) giving logical start and stop pulses to a TDC (time to digital converter) unit. [14]

The combined ADC+TDC unit was a FAST ComTec dual TADC 7072T with a constant ADC conversion time of 500 ns. Both channels had 13 bit conversion length. The smallest 50 ns timing window width combined with the manufacturer specified resolution of 4.1 channels results in about 25 ps timing resolution. In practice, for the 500 ns timing window required in typical TOF-ERDA measurements, the timing resolution of the TADC is limited to about 250 ps. [14]

Data retrieval from the Fast TADC was realized by modern FPGA module (National Instruments PXI-7811R-FPGA). The time stamping resolution is determined by the 40 MHz (equal to 25 ns) signal clock of the FPGA unit, although it was later discovered that the TADC unit could not provide data completely independently of its amplitude/length. In practice, the minimum coincidence window width was 4×25 ns for the TOF and the E signals. In typical measurements the coincidence window width was typically 12×25 ns = 300 ns. [14]

In this thesis for the experimental results we used as projectile ion beam isotope 35 of ions Cl^{4+} accelerated with +1.6MV potential. This ion beam is produced starting from an ion source of isotope 35 Cl^{-} accelerated with +1.6MV potential. Thus the total charge difference after the acceleration by the chlorine beam is $5e$. The projectiles hitting energy on the sample E_0 is:

$$E_0 = q * V = 5e * 1.6MV = 8MeV$$

Eq. 3-3

where e is the electron charge. The projectile ion beam is collimated thanks to a metallic slit positioned just before the sample. The projectile ion beam has an incident angle α=20°, the recoil angle is determined to be φ=40°. The angle is defined with respect to the target surface plane.

3.4 Performance figures of the IMEC setup

In this section performance figures are given for the TOF-ERDA telescope and the combined data-acquisition system. Together these figures describe well the actual performance of the ToF-ERDA system used for the thin film analysis. [14]

The consideration of the resolution of the energy detector is left out from this section as it will be analyzed later in the thesis.

3.4.1 Detection efficiency

The probability of detecting all the ions that pass through the timing gates is not 100 % as it is for the energy detector.

TOF spectrometers have a detection efficiency that is energy and ion dependent. For the IMEC setup the total detection efficiency is given by

$$\varepsilon = \varepsilon_{T1} * \varepsilon_{T2} * T_{Cfoil1}$$

Eq. 3-4

where ε_{T1} and ε_{T2} are the efficiencies of the two timing gates and the last term T_{Cfoil1} is the contribution associated with the scattering in the first carbon foil.

The detection efficiency of the timing gates is limited by the secondary electron yield of the foil Y_e. According to the Sternglass theory [3], the mean number of ejected secondary electrons is directly proportional to the electronic stopping power

$$Y_e = \Lambda \frac{dE}{dx}$$

Eq. 3-5

with the coefficient Λ depending on the atomic number and energy of the incident ion. We know from Section 2.2 that also the stopping power is dependent on the atomic number and energy of the incident ion.

Furthermore, for thin carbon foils, like those used in the IMEC setup, the electron emission is proportional to the film thickness, as observed by Koschar et al. [4]. On the other hand thinner foils are preferred for a smaller energy straggling. Consequently, a compromise of the optimal carbon foil thickness is then required.

In addition to the secondary electron emission, other factors affect the detection efficiency of the TOF detector. The electron detection efficiency of the MCP is determined by the probability that an incident electron creates an electron cascade when hitting a channel wall and is given by the sum of two components: the open area and the front surface contributions.

The last contribution to the detection efficiency is associated to the scattering in the first carbon foil. Due to this scattering, ions can deviate from their straight trajectories and consequently do not hit the second timing gate and the energy detector. The scattering of ions in the carbon foil becomes significant for very heavy ions. [2]

In Fig. 3.7 the detection efficiencies for He, Li and C are plotted. Comparison for the similar TOF-ERDA system at Jyväskylä University is also shown.

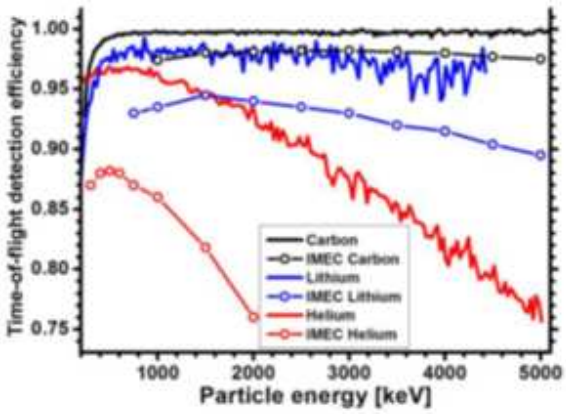

Figure 3-12 Energy dependence of detection efficiency for carbon, lithium and helium ions. The detection efficiencies curves for IMEC setup are shown together with efficiencies for Jyväskylä University system. [14] For carbon our detection efficiency is ~98%.

For carbon we have ~98% detection efficiency at 5MeV. But when elemental analysis is performed for lighter elements, the reduced detection efficiency needs to be taken into account. [14]

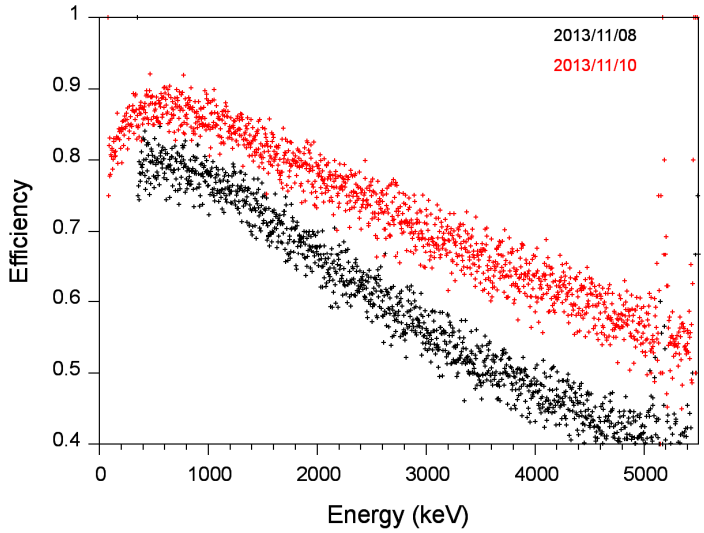

Figure 3-13 Energy dependence of detection efficiency for He ions hitting on 0.6 nm WAl layer deposited on 40 nm TiN on Si bulk. The black data were recorded with T2 MCP voltage of -1.7kV. The red data were recorded with T2 MCP voltage of -1.85kV.

For instance we recorded two different detection efficiency curves for He ions hitting on 0.6 nm WAl layer deposited on 40 nm TiN on Si bulk. These curves were measured in two days, having different T2 foil voltages.

The measurement on November 08th, 2013 (black dots in Figure 3-13) is done with T2 MCP voltage of -1.7 kV.

On November 10th, 2013 the detection efficiency was recorded with a T2 MCP voltage of -1850V. At 5 MeV He ions have improved from 40% to ~ 60%. Thus applying higher voltages across an MCP

leads to higher the number of electrons produced in the cascades inside the MCP channels. T2 MCP voltage was established at -1850V, as already said in Section 3.3.

3.4.2 Timing detector resolution

A good timing resolution is still critical in the separation of different masses in the TOF-E histograms, although deeper in the sample energy straggling and multiple scattering induced spreading (Section 2.5.1 and 2.5.2) overruns TOF resolution induced spreading. [14]

Measured timing signals from timing gates T1 and T2 are presented in Figure 3-14a-b. The signal from T2 MCP anode has rise time of about 1 ns(Figure 3-14b: rise time delimited between the two orange lines). While T1 MCP has rise time of 1.39ns(Figure 3-14a: rise time delimited between the two orange lines). T1 rise time is slightly worse, most likely because of the presence of a 1nF capacitor. [15]

Data for Figure 3-15 was measured by scattering 5.5MeV alpha particles. The figure shows that timing signals have a Gaussian distribution with FWHM 217ps. [15] This value should be adopted as the timing detector resolution in the IMEC setup.

Timing resolution depends on atomic number and energy of incident ions and TDC properties. [14]

a)

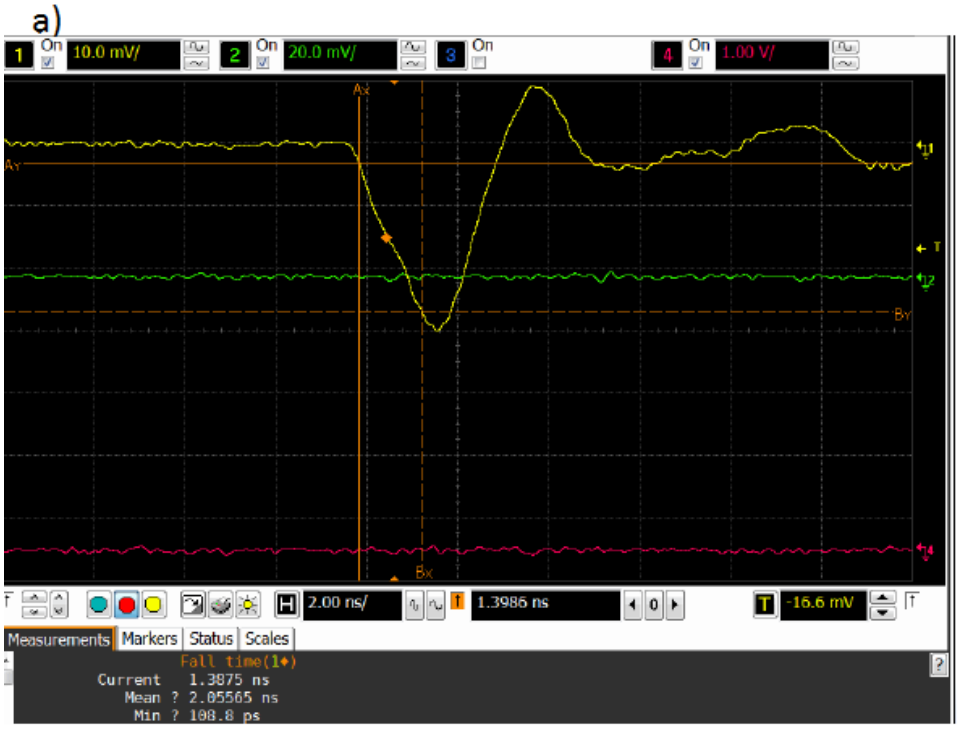

b)

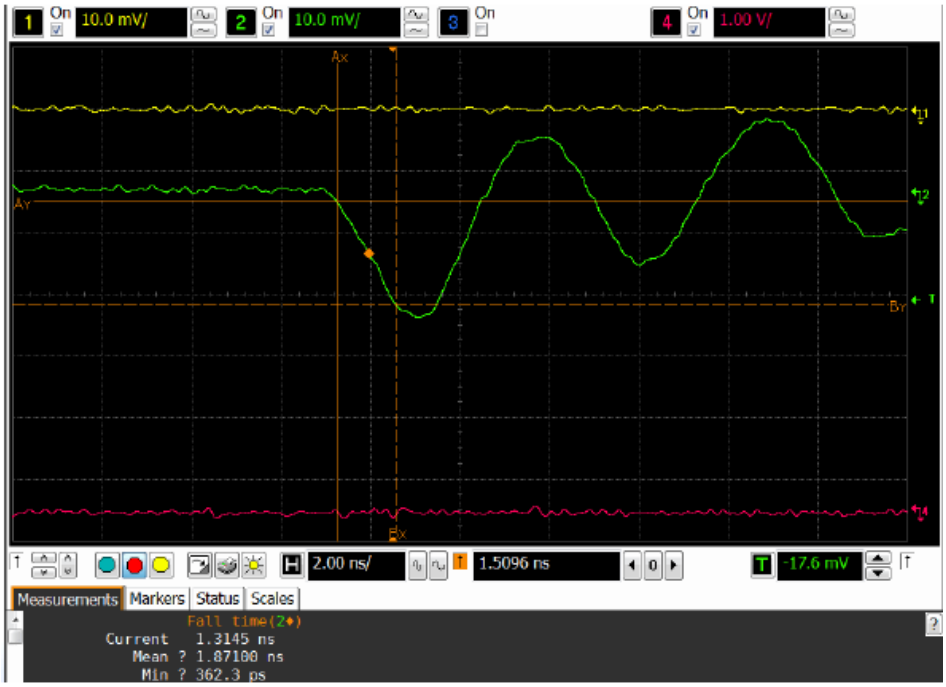

Figure 3-14 a) Timing signal from T1(yellow). Rise time delimited between continuous and dashed orange lines is 1.387ns. b) Timing signal from T2(green). Rise time delimited between continuous and dashed orange lines is 1.31ns. [15]

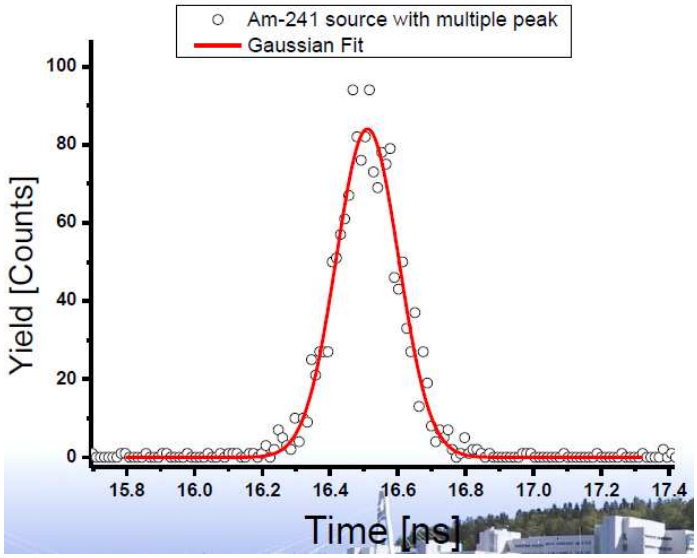

Figure 3-15 Timing signal distribution (empty circles) fitted with a pure Gaussian (red line) for scattered 5.5MeV alpha particles. The FWHM of the Gaussian, thus the timing resolution, is 217ps. [15]

4 Mass assignment procedure

In this chapter we will define what is a 2D TOF-Energy histogram, and the effect of silicon detector irradiation damages on the elemental signals.

To conduct elemental analysis on the samples it is common use to draw manually a polygonal cut in the 2D histogram around the elemental signal. This manual selection for mass is satisfactory when the signals from the different isotopes are well separated, such as for light elements. But it is difficult to apply when the cross talk between elemental signals is large. Moreover this task is subject to human error, indeed it requires a subjective judgment which precludes automatic analysis procedures and increases the overall uncertainty in the measurement. [8]

For all these reasons in this thesis we developed an automatic mass assignment procedure. In the following chapter we will present the procedure.

4.1 2D TOF-Energy histogram

The two detected quantities, TOF and energy channel, define the detection of a recoil ion representing an event. It is possible to plot a 2D histogram that on the x-axis has TOF, on the y-axis has energy channel and colors indicate the intensity of events.

The signals generated by different masses lie on different curves on the 2D histogram. In this way, each element could be analyzed separately.

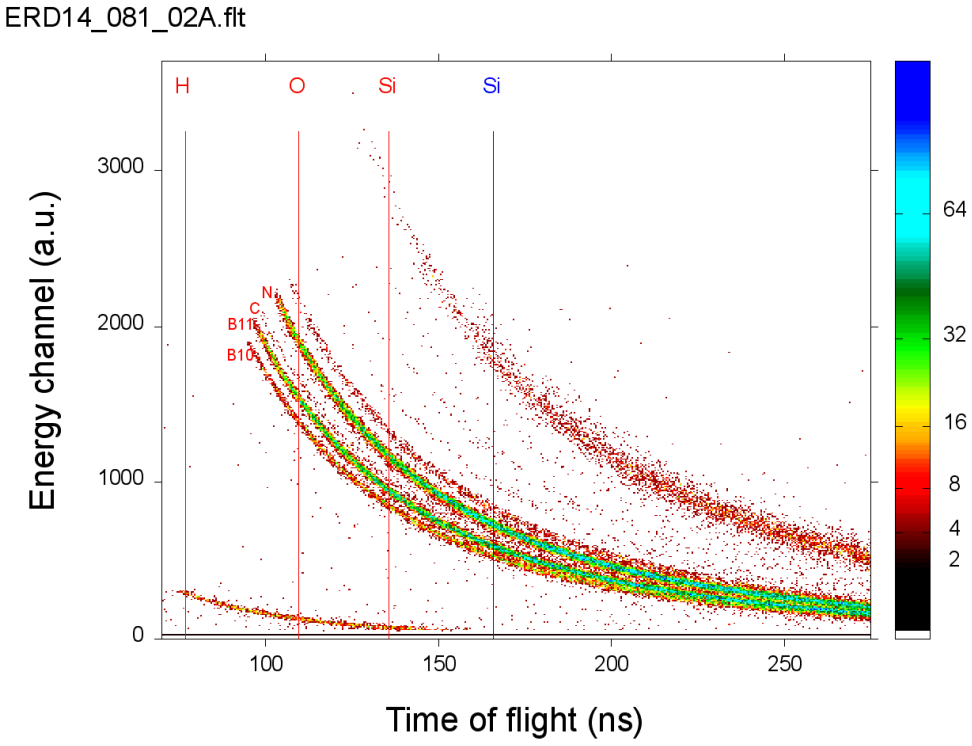

Figure 4-1 2D histogram of boron-nitride sample analysis with ERDA. The experimental setup is IMEC one (Section 3.3).

In Figure 4-1 it is shown the 2D histogram recorded on a boron-nitride sample. The analysis was conducted with the IMEC experimental setup. Each recoil belonging to a particular element is positioned in a different curve called “banana” in the histogram. In Figure 4-1 we highlighted boron 10, 11, carbon and nitrogen bananas.

As said the aim of an ERD experiment is to identify the elemental mass of each recoil event.

Elemental mass identification of an event is easily done by human eye when the banana are well separated, but when they are overlapped (as evident in Figure 4-1 for high TOF) mass discrimination conducted by human eye is impossible to perform.

4.2 Irradiation damage on silicon detectors

It is well-known that heavy ion irradiation results in the introduction of damage centers into the Si, which may cause drifts in the position of the energy spectra in the 2D histogram.

The spectra shifts arise from a reduced charge-carrier collection efficiency. It can be associated with direct recombination and also with the reduced electric field due to the increased voltage drop across the bias resistor associated with the generation current through the defect centers. [**5**]

One approach to compensate for the latter is to use a feedback system to maintain a constant potential difference across the silicon detector.

The spectra shifts have serious implications for measurements that are based on reproducible line shapes and positions and where accurate assignment of the depth vs. concentration in ERDA studies of light elements in heavy substrates is important. In such measurements, progressive spectra shifts will manifest themselves as an apparent loss of resolving power in individual spectra and a shift of spectral features in cases where a number of spectra are measured sequentially (e.g. from a batch of samples). ([**5**] and references therein)

4.3 Silicon detector response

In literature, El Bouanani et al. [8] observe that the nonlinear response of the Si detector is pronounced especially for Cu and heavier recoils in the energy range of 2-40MeV.

This is illustrated by El Bouanani et al. for molybdenum. The authors calculate the energies of the recoils according to the standard formula:

$$E = M(\frac{L}{T})^2$$

Eq. 4-1

as they know a priori M because of analyzing a molybdenum sample, L is the flight path and T is the time of flight for each recoil.

The difference between the Si detector energy response E_{ch} and the calculated energy E, called ΔE, has a nonlinear trend as a function of E. This is shown in Figure 4-2. Thus

$$\Delta E = E_{ch} - E = f(E)$$

Eq. 4-2

where $f(E)$ is a nonlinear function of the energy E. We can conclude that the energy detector response E_{ch} is nonlinear with the energy E.

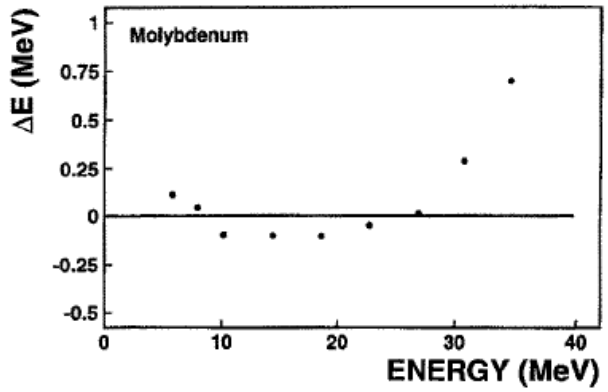

Figure 4-2 The deviation ΔE of the Si detector pulse height from the energy calculated from TOF as a function of the energy calculated from TOF for molybdenum recoils. [8]

It is not possible to assign the mass to recoils of any sample by simply filling Eq. 4-1 with E_{ch}, L and time of flight T, thus it results:

$$\mathrm{M} \neq E_{ch}(\frac{T}{L})^2$$

Eq. 4-3

A more complex model for mass assignment is needed.

4.4 Historical perspective

In literature El Bouanani et al. developed an optimized energy calibration procedure. In this work 77MeV $^{127}I^{10+}$ and 64MeV $^{127}I^{9+}$ were used as projectile ions. The incoming ions impinged at an angle $\alpha = 60°$, the recoil angle was $\varphi = 45°$, the path length L of 437.5mm. Standard samples used for the calibration were Au/glass, glass, $CuInSe_2$/glass, and Mo/glass. The glass substrates contained oxygen, sodium, silicon and calcium.

The calibration is based on a multivariate regression model based on the following considerations.

It was empirically seen that a second order polynomial law would yield a good energy calibration:

$$E = a_0 + a_1 E_{ch} + a_2 E_{ch}^2$$

Eq. 4-4

It was also found that the polynomial coefficients a_0, a_1 and a_2 could be represented by a straight line law dependence on recoil mass M_2. Thus it is possible to write:

$$E = c_0 + c_1 M_2 + c_2 E_{ch} + c_3 M_2 E_{ch} + c_4 E_{ch}^2 + c_5 M_2 E_{ch}^2$$

Eq. 4-5

where c_0,…, c_5 are the silicon detector coefficients which are valid for a given detector.

One approach would be to independently determine c_0,…, c_5 for some recoil reference elements. The situation is complicated because the recoil energy interval varies with recoil mass. [8] Thus El Bouanani et al. proposed the use of a multiple regression model to determine c_0,…, c_5 accurately.

Having six c coefficients and n recoil ions, of the order of 10^6, the manipulation of a $nx6$ matrix is required. This task is computationally expensive. Therefore it was chosen to consider only a limited representative number of equally spaced groups of data values on which the c parameters were optimized (Figure 4-3). [8]

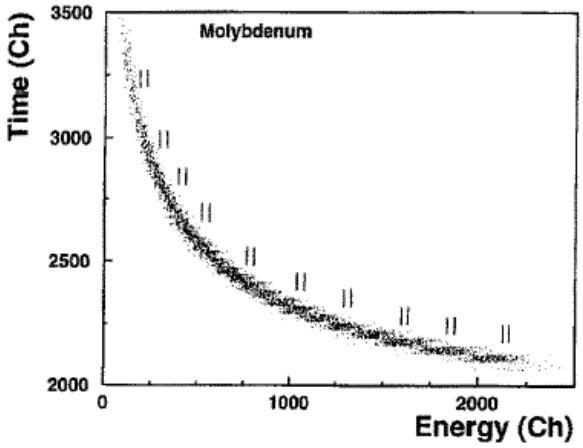

Figure 4-3 A 2D TOF-Energy histogram for molybdenum obtained with 77MeV I^{10+} as incident ion beam. The vertical parallel lines indicate the regions corresponding to the representative data values used in the calibration [8]

Changing the elements on which the calibration is performed the representative groups of data will change, as each element is positioned in a different banana in the histogram (Section 4.1). Thus the procedure is not optimized for every element. Human inputs are needed to select new sets of representative data for new elements.

The obtained energy calibration parameters were subsequently used to assign the mass M_2 of recoils from their known time of flight T, energy channel E_{ch} and telescope length L. In Eq. 4-5 substituting E with Eq. 4-1 and inverting to find M_2 it is possible to write:

$$M_2 = k\frac{c_0 + c_2 E_{ch} + c_4 E_{ch}^2}{((L^2/2T^2) - c_1 - c_3 E_{ch} - c_5 E_{ch}^2)}$$

Eq. 4-6

Here k is a constant that relates the absolute mass M with the isotopic mass A: $M = kA$.

In Figure 4-4 the data obtained from mass assignment according to Eq. 4-6 [8]. El Bouanani et al. procedure leads to a distribution of the signals for the different isotopes along straight lines of constant M. In Figure 4-4 it is shown a TOF-Mass histogram where mass results are not calibrated in [a.m.u.] but proportional to it. Thus relation coefficients are unknown.

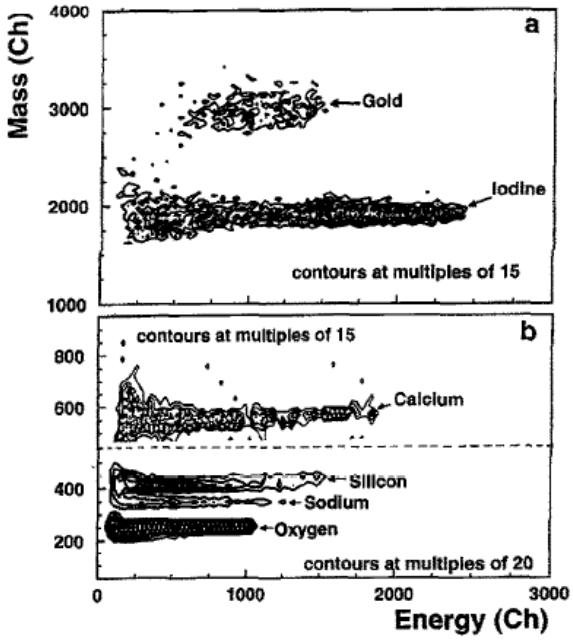

Figure 4-4 A contour plot of 2D mass-energy histogram for 64MeV $^{127}I^{10+}$ incident ion beam with mass assignment according to Eq. 4-6. [8]

Persson et al. [9] conducted further analysis with El Bouanani procedure and calibration coefficients on a Pd layer deposited on InP substrate sample.

According to Eq. 2-9 the energy loss ΔE for an ion is proportional to the travelled distance Δx through the stopping power S. This means that atoms placed deeper in the sample will have higher energy losses and will recoil with lower energy with respect to surface atoms.

In Persson's analysis the Pd layer is at the top of the sample, thus it is unexpected the tail observed in the Pd energy spectrum (Figure 4-5) for low energies (E~500channel).

Tests revealed that the relative height of the tail was very sensitive to the mass calibration. Indeed a simulated change of 0.5% in the calibration coefficients leads to significant changes in the relative amplitude of the tail. [9]

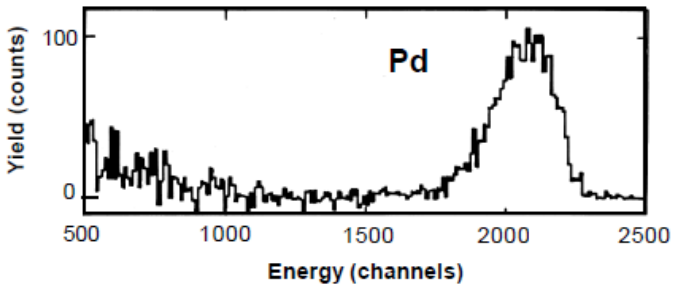

Figure 4-5 1D histogram energy distribution for Pd recoils. [9]

The tail is attributed to the progressive shift in the energy calibration which occurred between calibration and analysis. [9] This shift is resulting from radiation damage of the Si detector as observed by Zhang et al. [5].

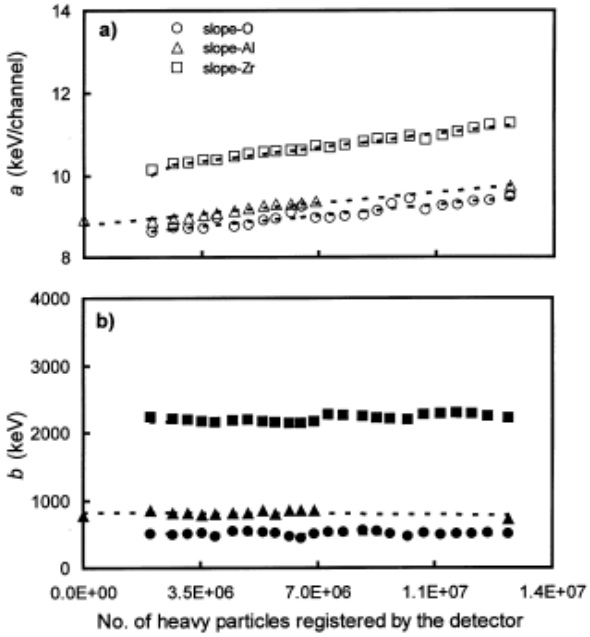

Figure 4-6 a) and b) Calibration constants from Eq. 4-7 vs. total number of the heavy particles registered in the energy detector. In a) and b) circles, triangles and squares correspond to ^{16}O, ^{27}Al and Zr recoils, respectively. The dotted lines are straight-line fits. [5]

Radiation damage in solid state detectors was studied in detail by Zhang et al. The authors had empirically determined a linear energy calibration model of type [5]

$$E = aE_{ch} + b$$

Eq. 4-7

Zhang et al. observed a progressive shift of the first-order coefficient a with the number of heavy particles hitting the Si detector, as visible in Figure 4-6. This shift was particularly evident for heavy

elements. On the other hand the constant term b was almost independent of the number of hitting particles.

Calibration shifts associated with radiation damage of Si detectors are problematic. These can be corrected by interpolation between calibrations established at regular intervals, although it is computationally tedious.

Alternatively gas ionization detectors can be employed. These kind of detectors are insensitive to the cumulative effects of radiation damage. [9]

Moreover a non-linear optimization model can overcome El Bouanani's one. Although an upgrade of IMEC ERD setup with gas ionization detectors will take place in the future, we present in this thesis the development of a non-linear optimization model for mass calibration.

Another contribution from literature about mass calibration is the one from Mallepell [18]. Mallepell empirical energy-TOF model is

$$E_{ch} = aE + E_0 = a\left(\frac{1}{2}ML^2\frac{1}{(t_0 - TOF)^2}\right) + E_0$$

Eq. 4-8

where M is the recoil mass, L is the telescope length, TOF and E_{ch} the time and energy coordinates in the 2-D histogram respectively. The author determined a, E_0 and t_0 calibration constants by means of a simultaneous least square fit of Eq. 4-8 on calibration curves from known elements [19]. In Figure 4-7 calibration $TOF - E_{ch}$ curves from known elements are represented with blue dots and the fitting on three elemental signals is shown by red lines.

From Eq. 4-8, since a, E_0 and t_0 coefficients are constant with mass, we can conclude Mallepell model for the energy detector response E_{ch} is linear with mass, thus with energy E.

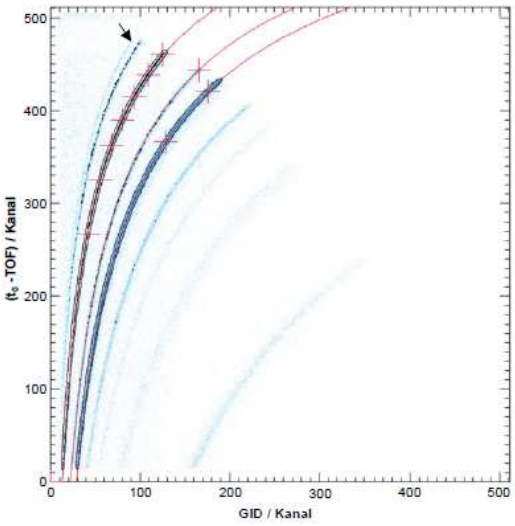

Figure 4-7 TOF-energy histogram for same calibration elements. Red curves represent the fitting on data according to Eq. 4-8 *[18].*

Each pair of data (TOF, E_{ch}) in the ToF-energy histogram in Figure 4-7 (blue dots) can be associated with a mass M by the following expression:

$$M = c(E_{ch} - E_0) * (t_0 - TOF)^2$$

Eq. 4-9

where M is the recoil mass, TOF and E_{ch} the time and energy coordinates in the 2-D histogram respectively and $c = 2/(aL^2)$ [19].

In Figure 4-7 we can see that for high TOF (($t_0 - TOF$)/Kanal<100) the fitting (red curves) doesn't seem to well reproduce elemental signals (blue dots). Moreover in Mallepell work it is not shown any TOF-Mass histogram after mass assignment, thus we cannot verify that elemental signals stand on straight iso-mass lines.

In conclusion, motivations for a new mass assignment procedure are:

- Computational effort.
- Human input to select representative intervals of data.
- Result is not calibrated (in [a.m.u.]) but proportional to it. Thus relation coefficients are unknown.
- Not verifiable straightness of mass signals in TOF-Mass histograms.
- Nonlinearity of the energy detector response E_{ch} with energy E.

4.5 New mass assignment procedure

In this section, we will introduce the new technique for mass calibration. This techniques is built in two parts:

a) energy calibration;
b) mass calibration.

4.5.1 Energy calibration

In Figure 4-1 it was shown a boron-nitride sample measured with IMEC setup. We acquired recoil events for a time interval of average five minutes. This time interval for measurement will be adopted for every calibration sample data acquisition.

In Figure 4-8a it is made an hand-made selection of the spectrum with nitrogen events (black line). Thus one gets a new 2D histogram with nitrogen spectrum only (Figure 4-8b).

We developed an energy calibration which is based on an empirical non-linear model for elemental signals representation:

$$E_{ch} = A_1 + A_2 * \frac{M}{2} * \left(\frac{L}{T - A_3}\right)^2$$

Eq. 4-10

where A_1, A_2 and A_3 are the energy calibration coefficients, M, L and T respectively the elemental mass, the telescope length and the recoil time of flight.

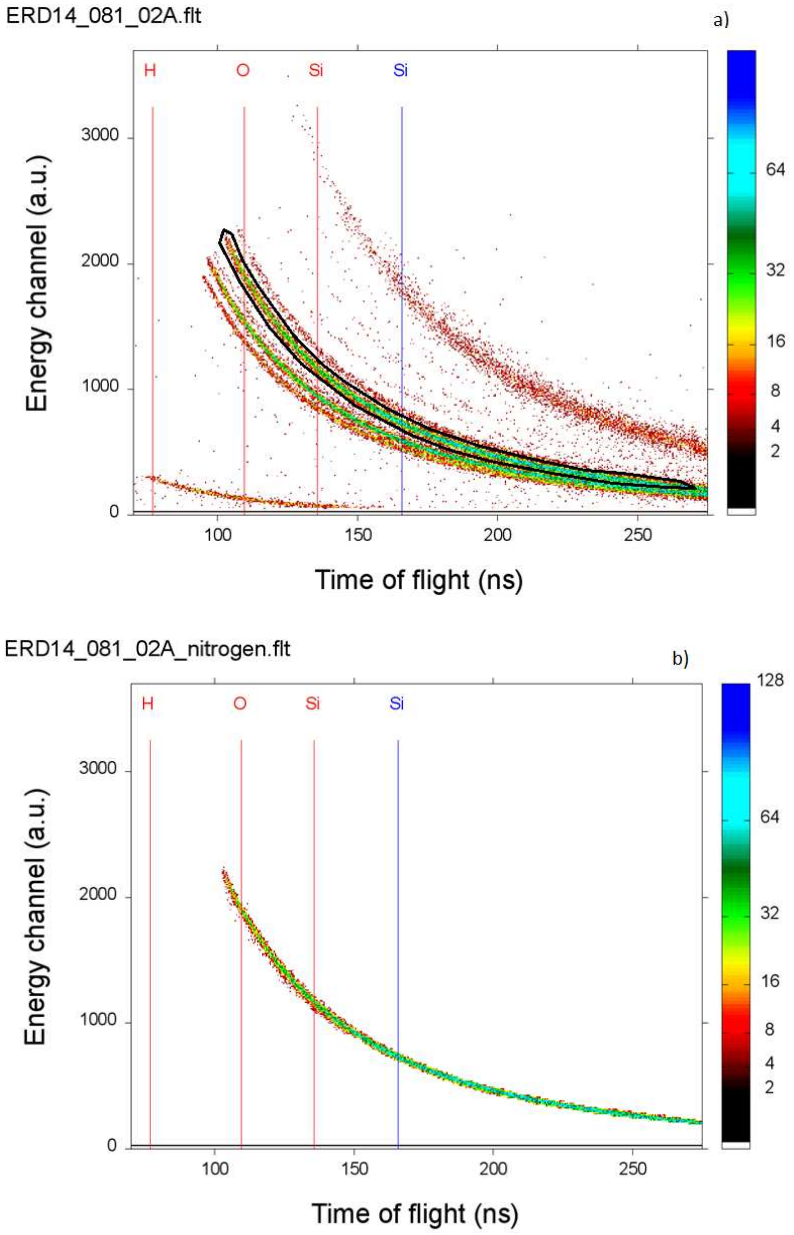

Figure 4-8 a) 2D histogram of boron-nitride sample analysis with IMEC ERD setup. The black line is an hand-made selection of nitrogen recoil ions. b) 2D histogram with only nitrogen recoils from the BN sample.

We have fitted the data in Figure 4-8b with the model in Eq. 4-10, with known $L = 755.4mm$, M(14.01a.m.u. for nitrogen), A_1, A_2 and A_3 as free parameters. The fitting looks for the optimal A_1, A_2 and A_3 coefficients that give the smallest error between data energy channels E_{ch} and simulated energy channels $E_{ch.sim}$. This error minimization is achieved through least squares method.

The sum of squared residuals between data and model is defined as

$$S = \sum_{i=1}^{n} (E_{ch\,i} - E_{ch,sim\,i})^2 = \sum_{i=1}^{n} {r_i}^2$$

Eq. 4-11

where n is the total number of recoiled ions. The least squares method finds its optimum when S is a minimum, so it stands:

$$\frac{dS}{dA_k} = 0 \;\rightarrow\; A_{k,opt} \qquad k = 1,2,3$$

Eq. 4-12

A C program was developed in order to find the minimum of S, thus the optimal A coefficients. It was observed that the A coefficients are extremely interdependent on each other.

This interdependence between the A coefficients is illustrated in Figure 4-9. For nitrogen, given a fixed A_1(-71.896 channel) the plot represents A_2 as a function of A_3, and it shows with colors the root mean square residual, called CHI:

$$CHI = \sqrt{\frac{\sum_{i=1}^{n} (E_{ch\,i} - E_{ch,sim\,i})^2}{n-1}}$$

Eq. 4-13

In Figure 4-9, one observes a region where CHI is minimum (Figure 4-9 in black), thus in this area $A_{2,opt}$ and $A_{3,opt}$ are optimized.

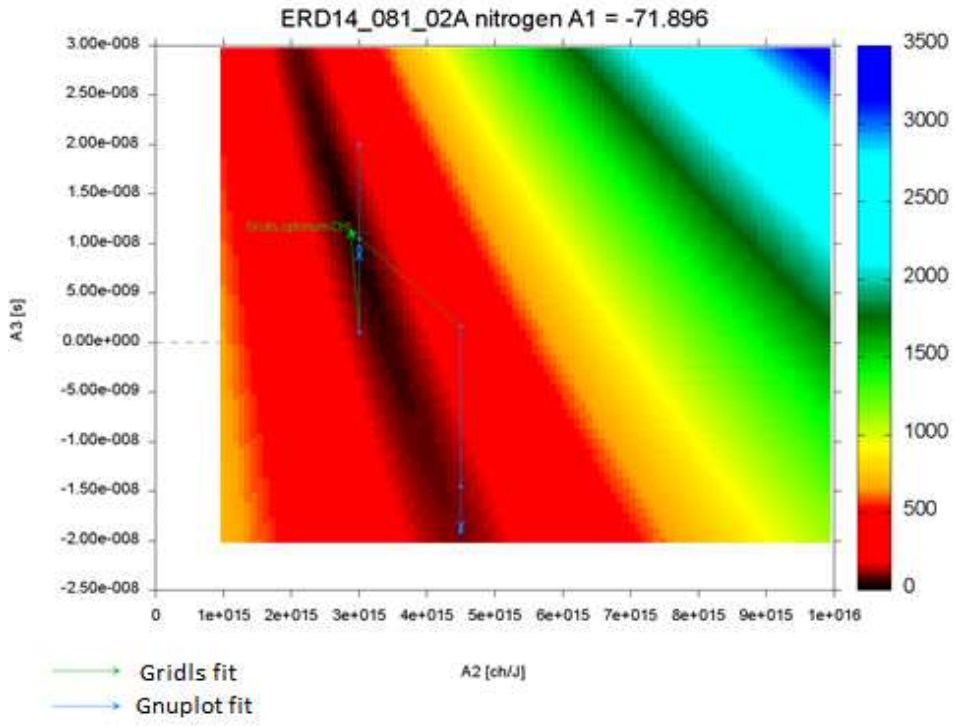

Figure 4-9 $\boldsymbol{A_2}$ as a function of $\boldsymbol{A_3}$ for fixed $\boldsymbol{A_1}$=-71.896ch for nitrogen. Colors represent the CHI, defined in Eq. 4-13.

In Figure 4-9, blue arrows point at the optimized values $A_{2,opt}$ and $A_{3,opt}$, starting from given random initial guesses for A_2 and A_3, the blue arrows point at the values ($A_{2,opt}$; $A_{3,opt}$) that not always stand in the region of minimum CHI (Figure 4-9 intense black). This especially happens when both initial guesses for A_2 and A_3 differ from optimal values, $\mathrm{A}_{2,\mathrm{opt}}$ and $\mathrm{A}_{3,\mathrm{opt}}$.

In Figure 4-9 green arrows point at the optimized values $\mathrm{A}_{2,\mathrm{opt}}$ and $\mathrm{A}_{3,\mathrm{opt}}$ returned from advanced program, starting from given random initial guesses for A_2 and A_3. The green arrows point at couples ($\mathrm{A}_{2,\mathrm{opt}}$; $\mathrm{A}_{3,\mathrm{opt}}$) that stand in the region of minimum CHI (Figure 4-9 intense black). Thus the advanced algorithm effectively finds optimal A coefficients.

The x-axis was partitioned in time-of -flight bins. For each time of flight bin filling Eq. 4-10 with flight path L, nitrogen mass M and nitrogen optimal A coefficients it was possible to simulate the best energy channel $E_{ch,sim\,bin}$ for nitrogen, according to

$$E_{ch,sim\,bin} = A_{1,opt} + A_{2,opt} * \frac{M}{2} * \left(\frac{L}{bin - A_{3,opt}}\right)^2$$

Eq. 4-14

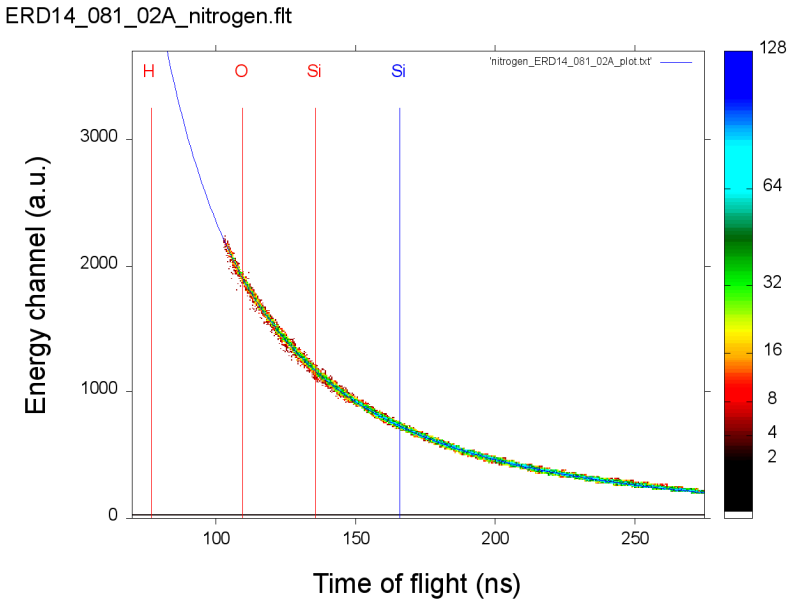

Figure 4-10) 2D histogram with nitrogen recoil data and best nitrogen energy spectrum, represented by the blue curve, calculated according to Eq. 4-14.

where $bin = TOF[s] = -2.7e-9 + 5.8189e-11j$ with $j = 1, \dots, 8192$. The value $-2.7e-9[s]$ is the time offset and $5.8189e-11$[s/ch] is the time per channel determined from time calibration.

From now on we will call "locus" the set of $(TOF; E_{ch,sim\,bin})$ data for each element. Representation of the optimal locus (Eq. 4-14) for nitrogen is shown in Figure 4-10 with a blue curve. It is shown that the theoretical function describes the experimental data to a very high degree of accuracy.

In conclusion every nitrogen recoil data in Figure 4-10 is projected on the best elemental locus (Figure 4-10 blue curve).

The same procedure described above was conducted not only for nitrogen, but for a full set of calibration elements. They comprise hydrogen, helium, isotopes 6 and 7 of lithium, beryllium, isotopes 10 and 11 of boron, carbon, nitrogen, oxygen, fluorine, sodium, magnesium, aluminum and isotope 35 of chlorine.

Given that A coefficients are mass dependent, fifteen sets of optimal A coefficients, one per isotope, were obtained in the calibration. Thus fifteen best elemental loci were simulated.

4.5.2 Mass calibration

Having obtained the best loci for all calibration elements (Figure 4-11 blue curves) it was possible to perform mass calibration.

For a fixed time of flight bin, $\overline{\mathrm{bin}} \sim 125\mathrm{ns}$, fifteen $\mathrm{E_{ch,sim\,M}}$ were calculated filling Eq. 4-14 with optimal A coefficients, the telescope length $\mathrm{L} = 755.4\mathrm{mm}$, the given value $\overline{\mathrm{bin}}$ and as M the fifteen

isotopic masses chosen for the calibration, $\mathrm{M} = \mathrm{M_H}, \mathrm{M_{He}}, \mathrm{M_{Li6}}, \mathrm{M_{Li7}}, \mathrm{M_{Be}}, \mathrm{M_{B10}}, \mathrm{M_{B11}}, \mathrm{M_C}, \mathrm{M_N}, \mathrm{M_O}, \mathrm{M_F}, \mathrm{M_{Na}}, \mathrm{M_{Mg}}, \mathrm{M_{Al}}, \mathrm{M_{Cl35}}$.

Representation of these fifteen $\mathrm{E_{ch,sim\,M}}$, one per calibration isotope, for $\overline{\mathrm{bin}}\sim 125\mathrm{ns}$ is shown in Figure 4-11. The intercepts of the purple line drawn at $\overline{\mathrm{bin}}\sim 125\mathrm{ns}$ with the blue lines, representing the optimal calibration energy spectra, are the fifteen $\mathrm{E_{ch,sim\,M}}$.

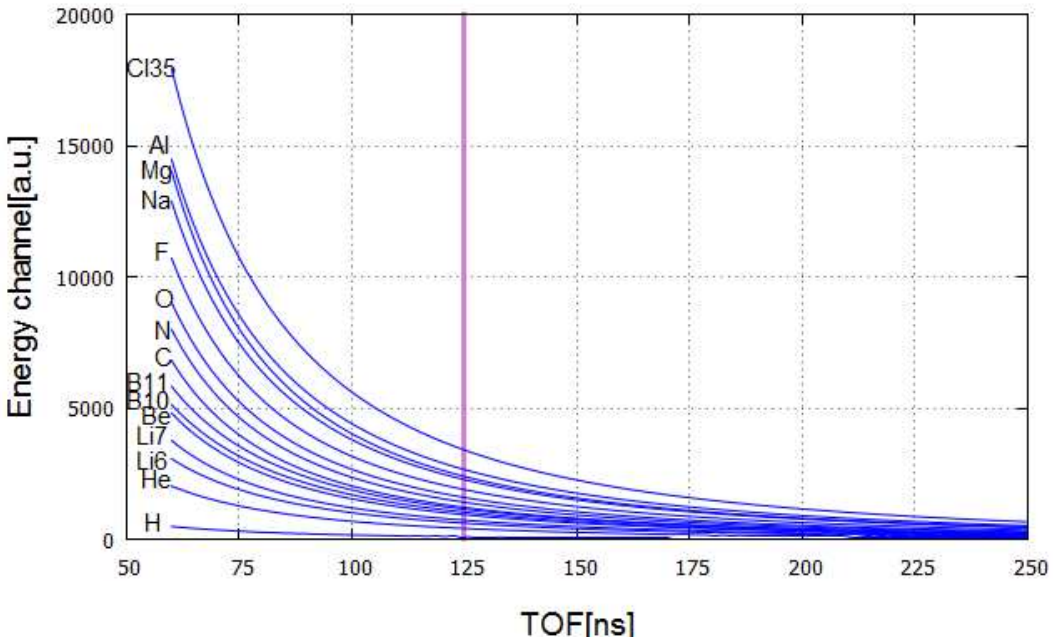

Figure 4-11 Blue lines represent the optimal isotopic energy spectra for calibration samples. Intercepts of the purple line drawn at $\overline{bin}\sim 125ns$ and the blue lines are the fifteen $E_{ch,sim\,M}$, one per isotope.

In Figure 4-12 the fifteen calibration masses were plotted as a function of the fifteen $E_{ch,sim\,M}$ values with green crosses.

Then, a fitting model, linear in its B coefficients, is applied on $(E_{ch,sim\,M}, M)$ data (Figure 4-12 green crosses):

$$\mathrm{M_{2,sim}[a.m.u.]} = \mathrm{B_1} + \mathrm{B_2 E_{ch,sim\,M}} + \mathrm{B_3 E_{ch,sim\,M}^2}$$

Eq. 4-15

The fitting looks for $\mathrm{B_{1,opt}}, \mathrm{B_{2,opt}}$ and $\mathrm{B_{3,opt}}$ coefficients that give the smallest error between calibration isotopic masses and simulated masses $\mathrm{M_{2,sim}}$.

$\mathrm{B_{1,opt}}, \mathrm{B_{2,opt}}$ and $\mathrm{B_{3,opt}}$ coefficients are bin dependent. Considering the purple line in Figure 4-11 at different values of x, being the time channel, it is possible to repeat the procedure described for one specifying bin to all the 8192 time bins.

Thus we get 8192 sets of optimal B coefficients, and 8192 plots like Figure 4-12 can be drawn.

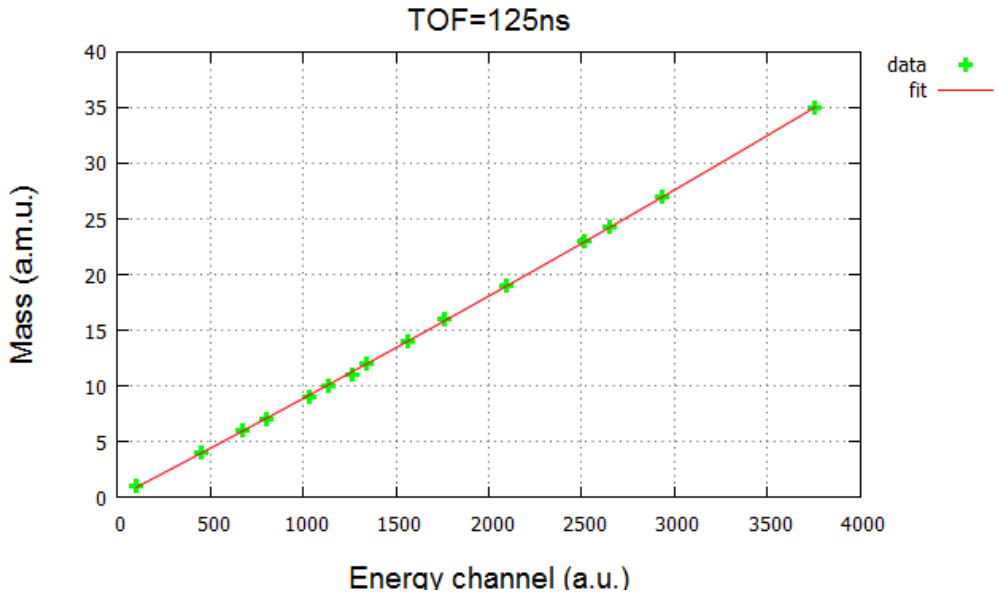

Figure 4-12 Elemental masses [a.m.u.] as a function of $\boldsymbol{E_{ch,sim\,\overline{bin}}}$ *values calculated according to* Eq. 4-14 *for* $\boldsymbol{\overline{bin}}$**~125*ns*** *represented by green crosses. The red line shows the fitting of the linear model of* Eq. 4-15 *to data values.*

Given the sets of optimal B coefficients for each time bin, it is possible to simulate the mass, according to Eq. 4-15, for each detected recoil in an ERD experiment. This mass simulation was done for the selected nitrogen events in Figure 4-8b, the result is shown in the TOF-Mass histogram in Figure 4-13a.

Nitrogen recoils manually selected in Figure 4-8a after the mass simulation effectively stand on the nitrogen mass line at 14a.m.u., as visible in Figure 4-13a. From now one we will call each isotopic line where recoils stand 'mass-banana'.

Figure 4-13b shows BN sample recoils from Figure 4-1 after mass simulation. For high TOF, one observes a broadening of the mass-banana for each element. Thus, it is not possible anymore for human eye to distinguish the elemental mass of each recoil.

Simulation of the masses was done for each calibration sample.

The appropriateness of this mass calibration technique is demonstrated by three points:

- distribution of the simulated masses along straight iso-mass lines (Figure 4-13a-b);
- the linear dependence between simulated masses $\mathrm{M_{2,sim}}$ and surface TOF ($\mathrm{T_{surf}}$) (Figure 4-13a-b blue oblique line) as predicted by inverting Eq. 2-6:

$$T_{surf} = L\sqrt{\frac{M_{2,sim}(M_1 + M_{2,sim})^2}{8M_1 M_{2,sim} COS^2\varphi E_{0i}}} = L(M_1 + M_{2,sim})\sqrt{\frac{1}{8M_1 COS^2\varphi E_{0i}}}$$

Eq. 4-16

- fast computational time.

Indeed this calibration procedure requires typically one hour for the data acquisition and half a day for data elaboration. Thus it will be easy to re-calibrate once in a month in order to align the procedure coefficients with radiation damage shifts of the elemental energy spectra.

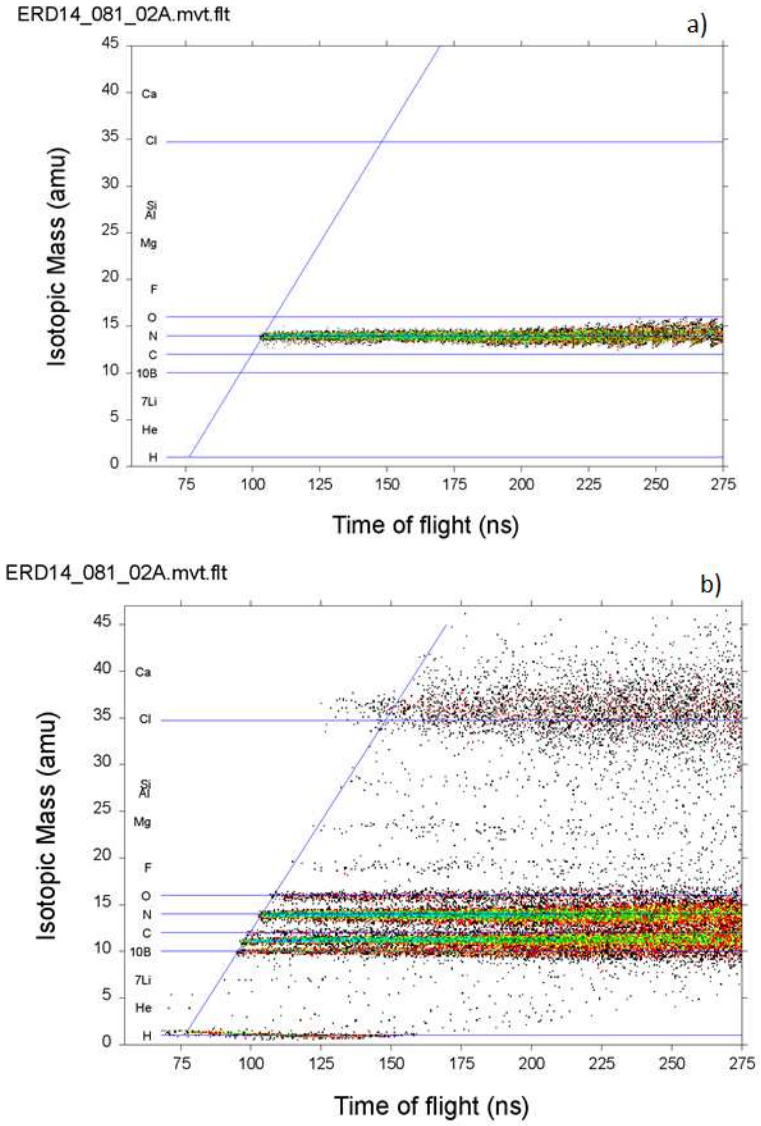

Figure 4-13 a) Manually selected nitrogen recoils from Figure 4-8a after mass simulation. b) BN sample recoils from Figure 4-1 after mass simulation.

5 Silicon detector energy resolution

Mass and depth resolution are both limited by the silicon detector energy resolution, knowledge of which is therefore needed for optimizing the design. In this chapter we present some literature studies about Si detector energy resolution and we compare them with experimental data from IMEC setup.

We also present a procedure to perform full width at half maximum calibration.

5.1 Historical perspective

In literature Hinrichsen et al. [10], Hult et al. [11] [13] and Döbeli et al. [12] studied silicon detector energy resolution.

Hinrichsen et al. [10] worked with ^{6}Li, ^{7}Li, ^{11}B, ^{16}O, ^{35}Cl and ^{81}Br ion beams backscattered from samples of gold evaporated onto silicon wafers, they have an incident angle on the sample of 7°, a new Ortec detector was used.

They fitted the pulse height spectra with the sum of a symmetrical Gaussian peak plus the convolution of a Gaussian with a one-sided exponential which reproduces the low-energy tail of the spectra. The fitting is shown in Figure 5-1 for different energy ^{11}B ion beams. Fitted line shapes are approximately independent of energy for a given ion beam. [10]

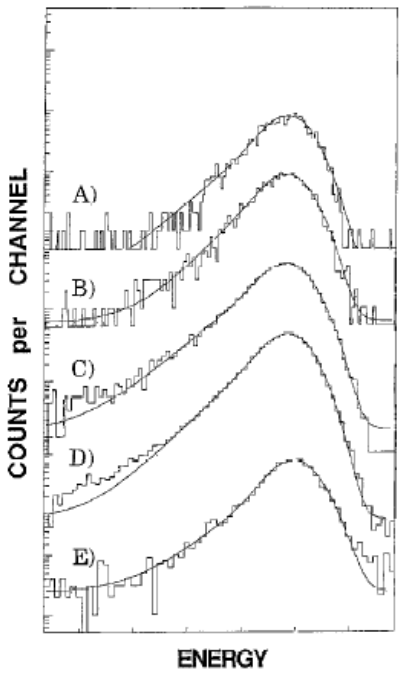

Figure 5-1 The pulse height distributions and fitted line shapes for {A) 16.02 MeV, (B) 7.12 MeV, (C) 1.78 MeV, (D) 0.80 MeV and (E) 0.47 MeV "B ions. The line shapes are essentially independent of energy for a given mass. [10]

The parameters derived from this non-linear least squares fit were then used to calculate the full width at half maximum (FWHM) of the distributions.

The main contributions to the observed FWHMs δE are:

a) kinematic energy spread due to the finite size of the beam spot and detector collimators δE_k;
b) energy loss variation in the finite thickness of the target δE_t;
c) energy straggling in the target δE_s;
d) noise in the detector electronics δE_n;
e) the detector resolution δE_d.

Factors a) to d) are generally small, however they were calculated and subtracted in quadrature to derive the detector resolution δE_d. [10]

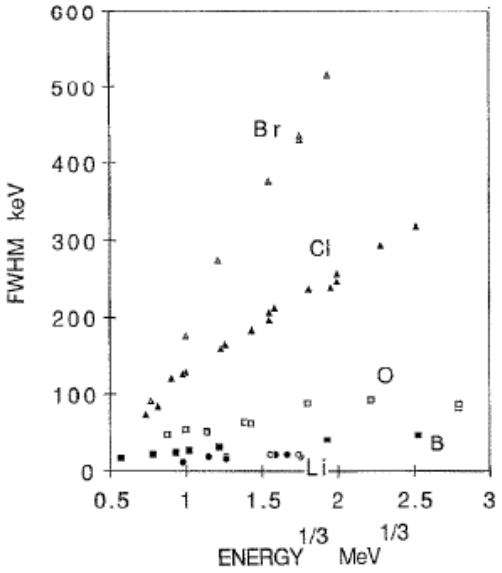

Figure 5-2 The present detector resolution data for: ^{6}Li (solid circles), ^{7}Li (open circles), ^{11}B (solid squares), ^{16}O (open squares, ^{35}Cl (solid triangles) and ^{81}Br (open triangles) are plotted vs the one-third power of the incident energy. *[10]*

Detector resolution for different ion beams is plotted as a function of scattered ion energy in Figure 5-2. It is observed that FWHMs are dependent on projectile ion masses.
The data for ^{6}Li and ^{7}Li showed some scatter but are consistent with previously reported results. Data in Figure 5-2 are in agreement with those of previous literature studies and follow an $E^{1/3}$ relation over an energy range from 0.4 to 25 MeV. [10]
Thus for Hinrichsen et al. case of study it stands:

$$\mathrm{FWHM} = \delta E_d \propto E^{1/3}$$

Eq. 5-1

Döbeli et al. [12] also studied silicon detector energy resolution. They worked with ion beam of H, Li, N, S, Fe, I and Au of energies between 0.3 and 2.7MeV. These beams hit directly a new Ortec silicon detector.

Especially for slow heavy ions the peaks produced in the pulse height spectrum can have an asymmetry. Therefore a fit function composed of a Gaussian with an exponential tail was chosen to determine the position and the true full width at half maximum of a peak. [12]

Figure 5-3 shows the silicon detector energy resolution as a function of energy for all investigated particle types. The energy resolution is dependent on ion masses, indeed it gets higher increasing the atomic number of the hitting particles. In Figure 5-3 it is also observed a linear dependence between energy resolution and hitting ion energies.

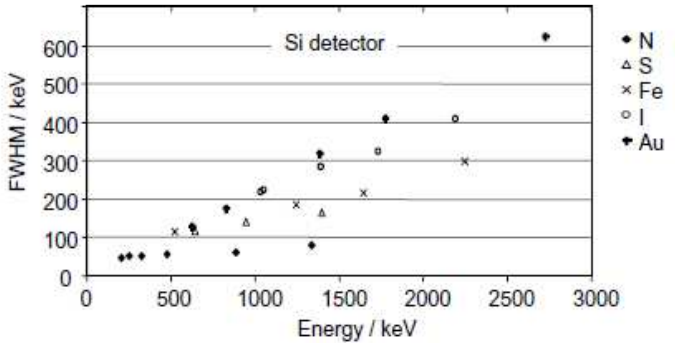

Figure 5-3 Energy resolution (FWHM) as a function of energy for all measured particles for gas ionization detector (above) and for silicon surface barrier detector (below). [12]

A third contribution to the silicon detector energy resolution study came from Hult et al. [11]. They worked with 77MeV $^{127}I^{10+}$ and 91MeV ^{127}I ions, incident and recoil angles were respectively 60° and 45° with respect to the surface sample. They analyzed a variety of reference samples.
TOF-E data were transformed to mass-energy histograms (Figure 5-4) using the multivariate calibration procedure developed by El Bouanani et al. in [8].

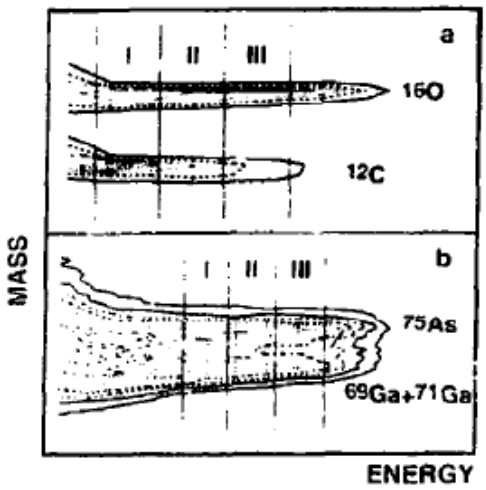

Figure 5-4 Mass-energy histogram of a) ^{12}C and ^{16}O b) ^{69}Ga and ^{71}Ga and ^{75}As. The mass transformation has been carried out using the procedure of El Bouanani et al. in [8]. [11]

The broadening of the mass spectrum was characterized by fitting Gaussian functions using a maximum likelihood method to the mass distribution for narrow energy bins. In the case of multi-isotope targets (GaAs and Mo) the fitted function was the sum of a number of Gaussians with an area that corresponded to the natural abundance and a position that corresponded to the known isotopic mass [11]. This Gaussian fitting is shown in Figure 5-5 for ^{69}Ga and ^{71}Ga and ^{75}As for three energy bins.

Starting from the classical formula for energy, inverting it to find mass

$$M = 2E(\frac{T}{L})^2$$

Eq. 5-2

the uncertainty in the mass assignment can be written as

$$\delta M = M(\frac{\delta E}{E} + 2\frac{\delta T}{T} + 2\frac{\delta L}{L})$$

Eq. 5-3

The contribution associated with the flight length $\delta L/L$ becomes significant only for fast recoils. They are very small in other cases and can be neglected [11].

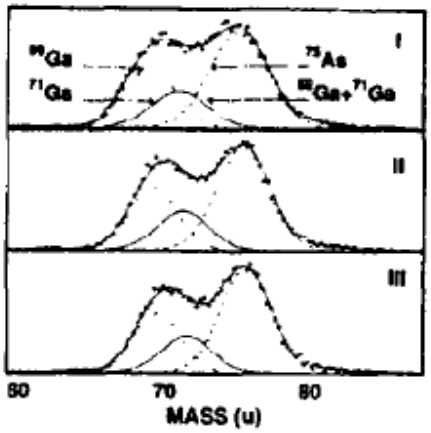

Figure 5-5 Projection onto the mass axis of ^{69}Ga and ^{71}Ga and ^{75}As from energy bins I, II and III. The fitting function is the sum of the three Gaussian distributions that are shown. [11]

The dominant contributions in Eq. 5-3 are associated with the energy detector resolution δE and the time detector resolution δT.

Modeling of the energy detector resolution in Eq. 5-3 was based on the empirical expression:

$$\delta E_{det} = a + bE^{1/3}$$

Eq. 5-4

Eq. 5-4 is an extended version of Eq. 5-1, the $\delta E_{det} - E^{1/3}$ linear relation already suiting Hinrichsen et al. energy resolution data.

By neglecting the contribution associated with the flight length and considering δT constant Eq. 5-3 can be expressed as

$$\delta M = M\left(aE^{-1} + bE^{-2/3}\right) + cM^{1/2}E^{1/2}$$

Eq. 5-5

Parameters a, b and c are mass dependent [11].

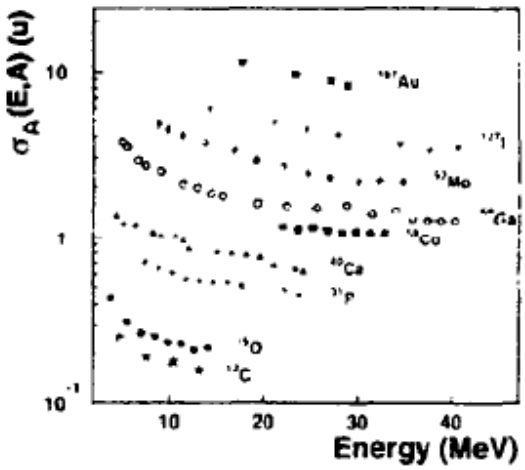

Figure 5-6 $\boldsymbol{\sigma_A(E,A)}$ versus energy E for various recoil isotopes. The lines indicate the best fit for Eq. 5-6. [11]

Thus the empirical fitting function for the Gaussian standard deviation results in:

$$\sigma_A(E,A) = C_1 + C_2A^{3/2}E^{-1} + C_3A^2E^{-2/3} + C_4AE^{1/2}$$

Eq. 5-6

with known fitted constants, and A the isotopic mass. The E^{-1} and $E^{-2/3}$ terms in Eq. 5-6 are associated with the energy detector resolution, whilst the $E^{1/2}$ term is associated with the contribution from the time detector resolution.

Figure 5-6 shows measured values of $\sigma_A(E,A)$ together with the fitted function of Eq. 5-6 [11].

5.2 Experimental results

From mass-TOF histograms, like the one for nitrogen in Figure 4-13a, the x-axis was divided into slices which contain at least 2000 recoils.

For each time slice we assume that recoil counts as a function of mass, called mass spectrum, have a Gaussian distribution. We will demonstrate the validity of this assumption in later chapters. We call μ and σ respectively the mean and the standard deviation of the Gaussian distribution. Then for Gaussian distributions it is possible to write

$$FWHM_{MASS} = 2.355 * \sigma = 2.355 * (\frac{\sum_{i=1}^{N}(M_i - \mu)^2}{N})$$

Eq. 5-7

where M_i is the assigned mass of recoil i, and N is the number of recoils in the time slice.

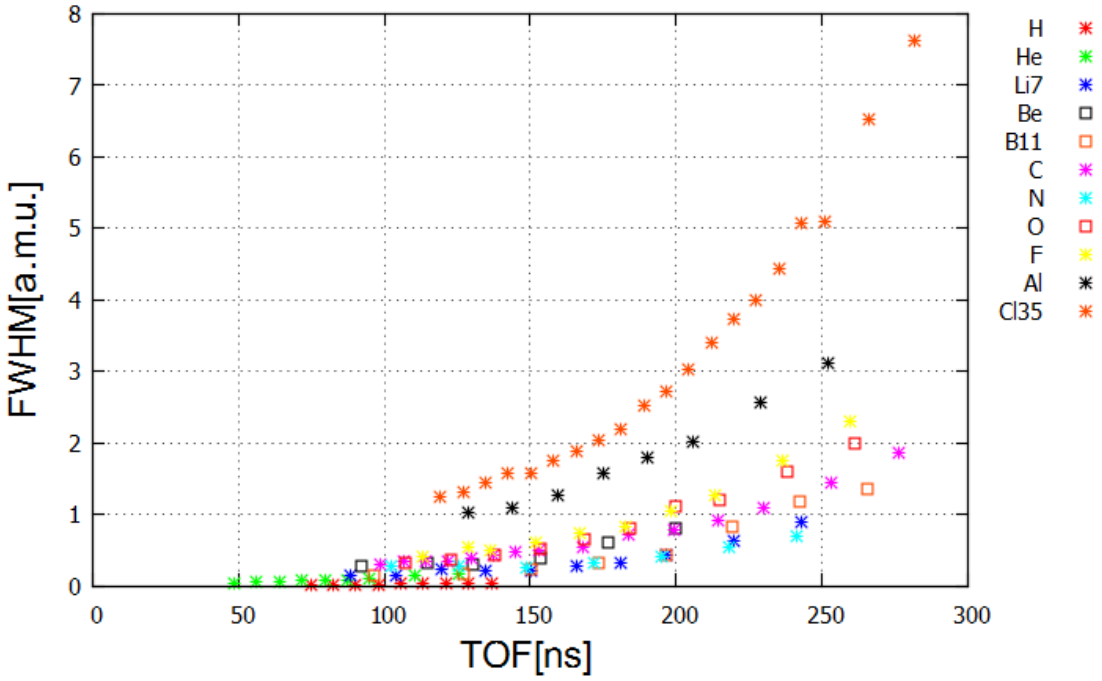

Figure 5-7 . $\boldsymbol{FWHM_{MASS}}$ values calculated according to Eq. 5-7 are plotted as a function of $\boldsymbol{TOF}$ for hydrogen, helium, lithium 7, beryllium, boron 11, carbon, nitrogen, oxygen, fluorine, aluminum and chlorine 35. Lithium6, boron10, sodium and magnesium $\boldsymbol{FWHM_{MASS}}$ values are missing because there were few recoils detected.

According to Eq. 5-7 $FWHM_{MASS}$ values were calculated for each time slice and for each isotope chosen for calibration. $FWHM_{MASS}$ values as a function of TOF are represented in Figure 5-7. For isotope 6 of lithium, isotope 10 of boron, sodium and magnesium we had few recoil counts, thus values of $FWHM_{MASS}$ were not accurate.

Alternatively it is possible to express the TOF data of pair data $(TOF, FWHM_{MASS})$ in Figure 5-7 as energy with the classical formula in Eq. 4-1. Filling Eq. 4-1 with TOF data, L telescope length and M calibration isotopic masses we can calculate energies for each $FWHM_{MASS}$ data and for each calibration isotope.

Also $FWHM_{MASS}$ data of pair data $(TOF, FWHM_{MASS})$ in Figure 5-7 were transformed into $FWHM_{Energy}$ data according to

$$FWHM_{Energy} = FWHM_{MASS}(\frac{L}{T})^2$$

Eq. 5-8

Filling Eq. 5-8 with TOF data, telescope length L, and $FWHM_{MASS}$ data it is possible to obtain $FWHM_{Energy}$ data. These $FWHM_{Energy}$ data were plotted as a function of energy in Figure 5-8.

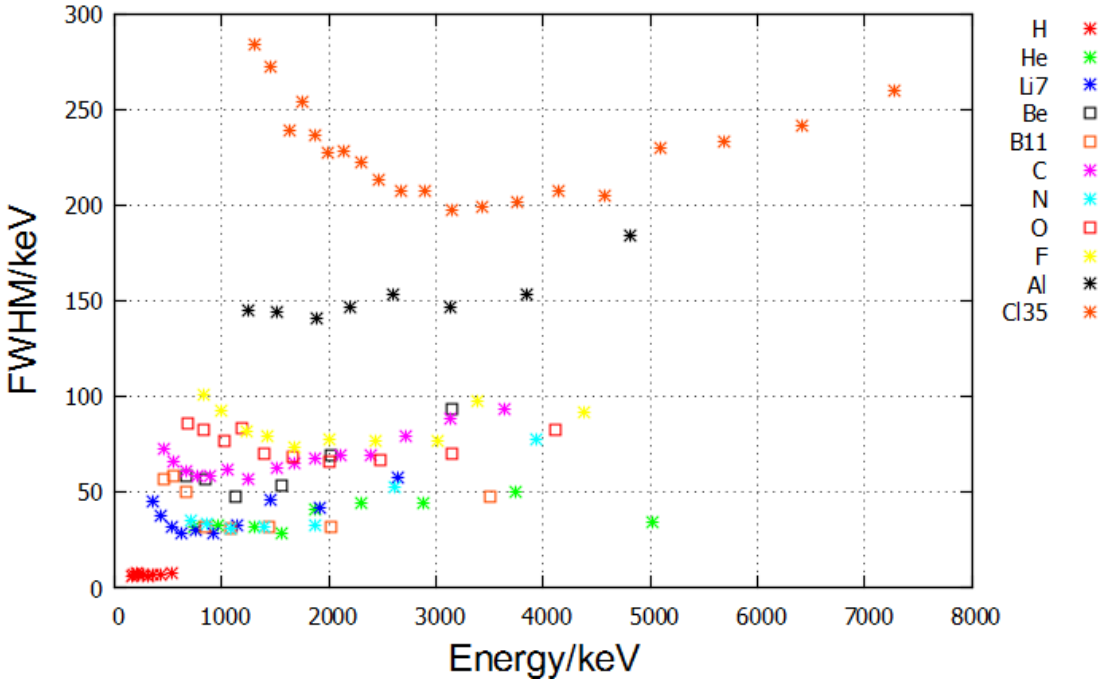

Figure 5-8 $FWHM_{Energy}$ values are plotted as a function of energy for hydrogen, helium, lithium 7, beryllium, boron 11, carbon, nitrogen, oxygen, fluorine, aluminum and chlorine 35.

We can compare $FWHM_{Energy}$ data in Figure 5-8 with data in Figure 5-3 from Döbeli et al. [12]. The common element for which $FWHM_{Energy}$ data are reported in both figures is nitrogen.

Nitrogen data in Figure 5-8 (cyan stars) which occurs at energy 1000keV has $FWHM_{Energy}$ of approximately 30keV. Nitrogen data in Figure 5-3 (rhombus) which occurs at around energy 1000keV has $FWHM_{Energy}$ of approximately 70keV. Thus smaller values of $FWHM_{Energy}$ were obtained from IMEC setup for nitrogen. This could mean that IMEC setup has a better silicon detector energy resolution than Döbeli et al. one.

As a general consideration in Figure 5-8 it was seen that for low energies the isotopic $\mathrm{FWHM_{Energy}}$ trends as a function of energy deviate from Döbeli et al. empirical monotonic trends (Figure 5-3). This is particularly true for elements with high atomic number (high mass), which exhibit unexpected higher $\mathrm{FWHM_{Energy}}$ in the low energies range.

For instance we can roughly compare isotope 35 of chlorine data in Figure 5-8(orange stars) with sulfur data in Figure 5-3(empty triangle), as these two have the closest atomic numbers(masses). In Figure 5-8 chlorine35 $\mathrm{FWHM_{Energy}}$ trend exhibits a decreasing behavior with energy in the low energies range (1000-3000keV), in Figure 5-3 sulfur $\mathrm{FWHM_{Energy}}$ trend is increasing with energy in the energy range between 500keV and 1500keV.

This was probably due to energy straggling in the first carbon foil of the timing gate. Energy straggling was defined in Section 2.5.1 as the statistical fluctuations affecting the energy losses of two or more identical energetic particles traversing a homogeneous medium.

Given the energy straggling definition, due to energy straggling we can have particles energy spreading. Thus this could be an explanation for increasing the $\mathrm{FWHM}_{\mathrm{Energy}}$ values in the low energies range, where the energy losses strongly affect recoils.

Plus as analyzed in Section 2.2 energy loss increases with the atomic number of the ions, as represented in Figure 2-4. This could explain the increasing deviation from monotonic behavior in the $\mathrm{FWHM}_{\mathrm{Energy}}$ trends in Figure 5-8 with increasing atomic number elements.

As a future outlook this mismatch in the low energies region between IMEC setup $\mathrm{FWHM}_{\mathrm{Energy}}$ data and Döbeli et al. $\mathrm{FWHM}_{\mathrm{Energy}}$ could be studied.

As these $FWHM_{Energy}$ data were affected by this phenomenon, they were not taken into account in the development of this procedure. Thus we will only consider $FWHM_{Energy}$ data increasing with energies (Figure 5-9).

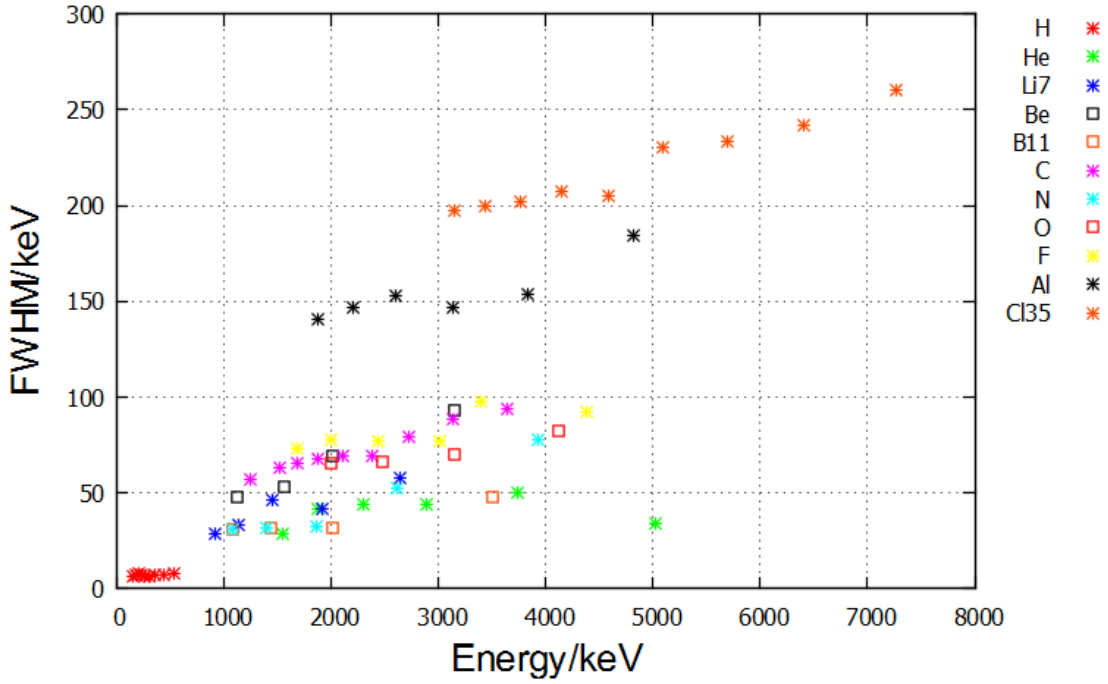

Figure 5-9 No straggling affected $\boldsymbol{FWHM_{Energy}}$ values are plotted as a function of energy for hydrogen, helium, lithium 7, beryllium, boron 11, carbon, nitrogen, oxygen, fluorine, aluminum and chlorine 35.

In Figure 5-10 we plot no straggling affected $FWHM_{Energy}$ data as a function of $E^{1/3}$ for the eleven calibration isotopes, where we got $FWHM_{MASS}$ values. They are represented by stars and empty squares. In Figure 5-10 we plot with lines Eq. 5-1 fitting the data through optimal zero-order and slope coefficients for each of the eleven calibration isotope.

We can compare Figure 5-10 with Hinrichsen et al. [10] Figure 5-2. The common elements for which $FWHM_{Energy}$ data are reported in both figures are lithium7, boron11, oxygen16 and chlorine35, respectively in Figure 5-10 drawn with blue stars, orange empty squares, red empty squares and orange stars, and in Figure 5-2 they are plotted with open circles, solid squares, open squares and solid triangles.

For lithium7 in Figure 5-2 data at $E^{1/3}$~$1.5MeV^{1/3}$ and $E^{1/3}$~$1.75MeV^{1/3}$ were reported to have both $FWHM_{Energy}$~$25keV$. In Figure 5-10 the highest energy $FWHM_{Energy}$ recorded data is at about $E^{1/3}$~$1.4MeV^{1/3}$ and its $FWHM_{Energy}$ value is already above 50keV.

For boron11 in Figure 5-2 data at $E^{1/3}$~$1MeV^{1/3}$ was reported to have $FWHM_{Energy}$~$30keV$. In Figure 5-10 the lowest energy $FWHM_{Energy}$ recorded data is at $E^{1/3}$~$1MeV^{1/3}$ and its $FWHM_{Energy}$ value is approximately 30keV.

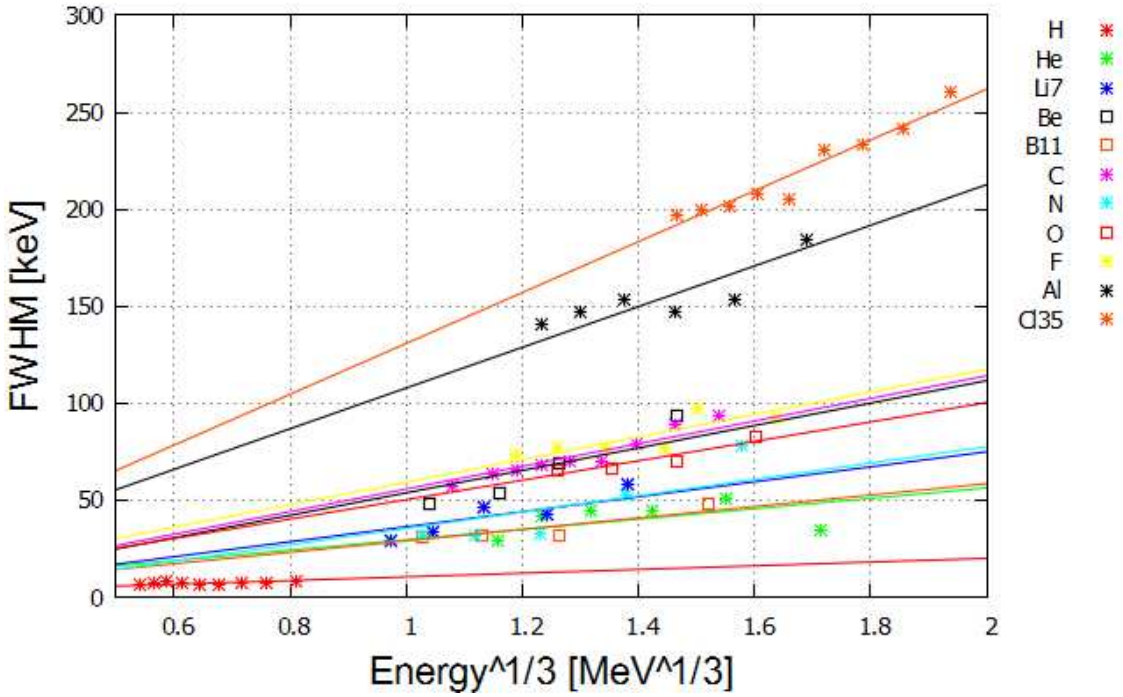

Figure 5-10 No straggling affected $\boldsymbol{FWHM_{Energy}}$ data as a function of $\boldsymbol{E^{1/3}}$ for hydrogen, helium, lithium 7, beryllium, boron 11, carbon, nitrogen, oxygen, fluorine, aluminum and chlorine 35. Eq. 5-1 fitted to the data thanks to optimal zero-order and slope coefficients is plotted with lines of different color for each isotope.

For oxygen16 in Figure 5-2 data at $E^{1/3}$~$1.5MeV^{1/3}$ was reported to have $FWHM_{Energy}$~$60keV$. In Figure 5-10 data at $E^{1/3}$~$1.5MeV^{1/3}$ is found to have $FWHM_{Energy}$~$75keV$.

For chlorine35 in Figure 5-2 data at $E^{1/3}$~$1.5MeV^{1/3}$ and $E^{1/3}$~$2MeV^{1/3}$ were reported to have respectively $FWHM_{Energy}$~$200keV$ and $FWHM_{Energy}$~$250keV$. In Figure 5-10 data at $E^{1/3}$~$1.5MeV^{1/3}$ and $E^{1/3}$~$2MeV^{1/3}$ is found to have respectively $FWHM_{Energy} = 200keV$ and $FWHM_{Energy} = 260keV$.

Thus we have accordance of $FWHM_{Energy}$ data between IMEC setup $FWHM_{Energy}$ values and Hinrichsen et al. [10] data for boron11 and chlorine35; lithium7 and oxygen16 were found to have higher $FWHM_{Energy}$ when extracted from data measured in the IMEC setup.

Moreover although in Figure 5-10 beryllium, nitrogen and aluminum $FWHM_{Energy}$ data appear to have a non-linear relation with $E^{1/3}$; we can observe that for the remaining elements, except for helium, the relation $FWHM_{Energy} - E^{1/3}$ is linear, as predicted from Eq. 5-1.

In the coming section we will analyze in further detail the $FWHM_{Energy} - E$ dependence for our case of study, thus $FWHM_{MASS} - TOF$ dependence. Given that Eq. 5-1 is a good starting point to model $FWHM_{Energy}$ data for the majority of our calibration isotopes, we will improve this dependence to take into account variations of $FWHM_{Energy} - E$ behaviour for beryllium, nitrogen and aluminum.

In Figure 5-11 we plot no straggling affected $FWHM_{MASS}$ data as a function of energy for the eleven calibration isotopes where we got $FWHM_{MASS}$ data.

We can compare Figure 5-11 with Hult et al. [11] Figure 5-6. The common elements for which $FWHM_{MASS}$ data as a function of energy are reported in both figures are isotope 12 of carbon and isotope 16 of oxygen.

Our carbon $FWHM_{MASS}$ data (purple stars in Figure 5-11) occur on average at lower energies with respect to the carbon data in Figure 5-6. But the lowest energy carbon data in Figure 5-6 occurs at an energy around 3MeV and has $FWHM_{MASS}$ of 0.3 a.m.u. Carbon data in Figure 5-11(purple stars) around energy 3MeV have approximately $FWHM_{MASS}$ of 0.3 a.m.u.

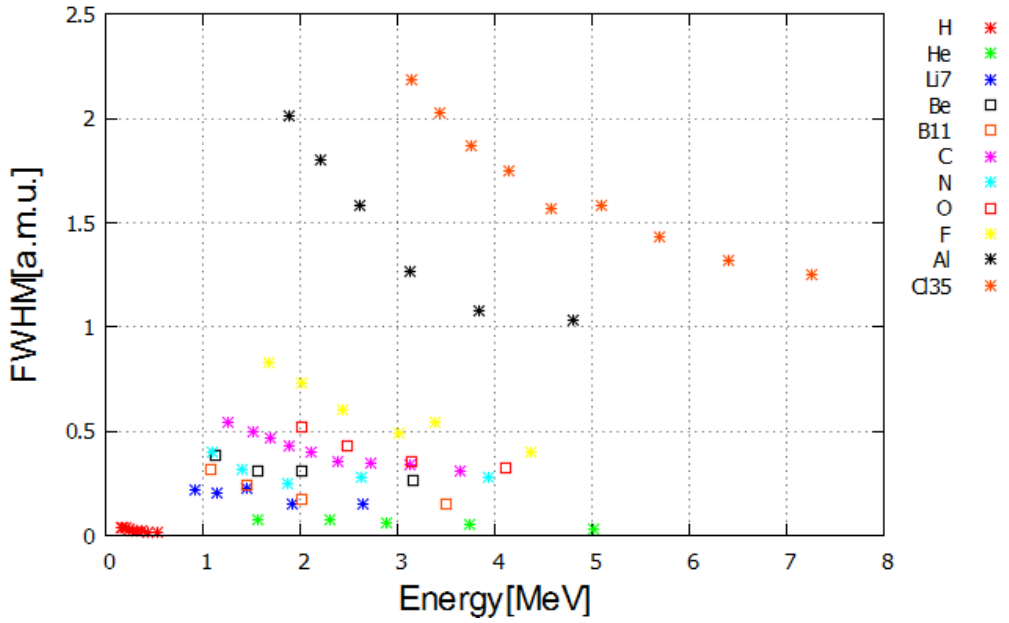

Figure 5-11 $FWHM_{MASS}$ values calculated according to Eq. 5-7 are plotted as a function of energy, obtained from TOF according to Eq. 4-1 for hydrogen, helium, lithium 7, beryllium, boron 11, carbon, nitrogen, oxygen, fluorine, aluminum and chlorine 35.

The lowest energy oxygen data in Figure 5-6 occurs at an energy around 2MeV and has $FWHM_{MASS}$ of approximately 0.45 a.m.u. Oxygen data in Figure 5-11(red empty squares) at energy 2MeV has $FWHM_{MASS}$ of 0.5 a.m.u. Thus we found pretty accordance between our data and Hult et al. ones.

In Eq. 5-4 Hult et al. empirically modeled their silicon detector energy resolution with a linear dependence with $E^{1/3}$, the same empirical model found by Hinrichsen et al.. Hult et al. mass resolution relation with energy expressed in Eq. 5-5 is derived from Eq. 5-4.

Thus to compare IMEC setup $FWHM_{MASS} - E$ trend with Hult et al. one the same considerations made during comparison with Hinrichsen et al. data stand.

5.3 FWHM calibration

From Figure 5-10 we had clear the need for a more general $FWHM_{Energy} - E$ relation than Eq. 5-1, so that we can take into account also beryllium, nitrogen and aluminum $FWHM_{Energy} - E$ behavior. Their $FWHM_{Energy}$ dependence with $E^{1/3}$ is more than linear, we can conclude that the order of the relation between energy resolution and energy is also mass dependent.

Alternatively we can analyze $FWHM_{MASS} - E$ relation, as we can transform $FWHM_{Energy}$ into $FWHM_{MASS}$ by inverting Eq. 5-8.

Eq. 5-3 suggests that the major contribution to mass resolution is the energy detector resolution, since in the IMEC setup timing detector resolution is negligible (Section 3.4.2).

Thus Eq. 5-3 becomes

$$\delta M = FWHM_{MASS,sim} = M\frac{\delta E}{E}$$

Eq. 5-9

The term $\delta E/E$ has an empirical determination. We start from Eq. 5-1 and we make it more general in order to better reproduce our data, so the $\delta E/E$ term can be written as

$$\frac{\delta E}{E} = C_1^* + C_2^* E^{C_3}$$

Eq. 5-10

It is possible to rewrite Eq. 5-9 with the empirical formula

$$FWHM_{MASS,sim} = M\frac{\delta E}{E} = C_1 + C_2 * E^{C_3}$$

Eq. 5-11

where $FWHM_{MASS}$ is in a.m.u., E is in MeV and C_1, C_2 and C_3 are mass dependent.

$FWHMMASS,sim=M\delta EE=C1+C2*EC3$ equation as

$$FWHM_{MASS,sim} = M\frac{\delta E}{E} = C_1 + C_2 * (\frac{M}{2} * L^2)^{C_3} * T^{(-2*C3)}$$

Eq. 5-12

Firstly we will find a model for the nitrogen $FWHM_{MASS}$ data. These data were calculated from nitrogen recoils according to Eq. 5-7. We plotted them as a function of TOF in Figure 5-12 with stars.

Filling Eq. 5-12 with telescope length L, nitrogen mass M, as T the time of flight data of each pair data $(TOF, FWHM_{MASS})$ in Figure 5-12 and arbitrary C_1, C_2 and C_3 one obtains simulated $FWHM_{MASS,sim}$.

An advanced program was developed in order to fit the model of Eq. 5-12 with nitrogen $FWHM_{MASS}$ data plotted in Figure 5-12. The fitting looks for $C_{1,opt}, C_{2,opt}$ and $C_{3,opt}$ coefficients that give the smallest error between $FWHM_{MASS}$ calculated from data according to Eq. 5-7 and simulated data $FWHM_{MASS,sim}$ calculated according to Eq. 5-12.

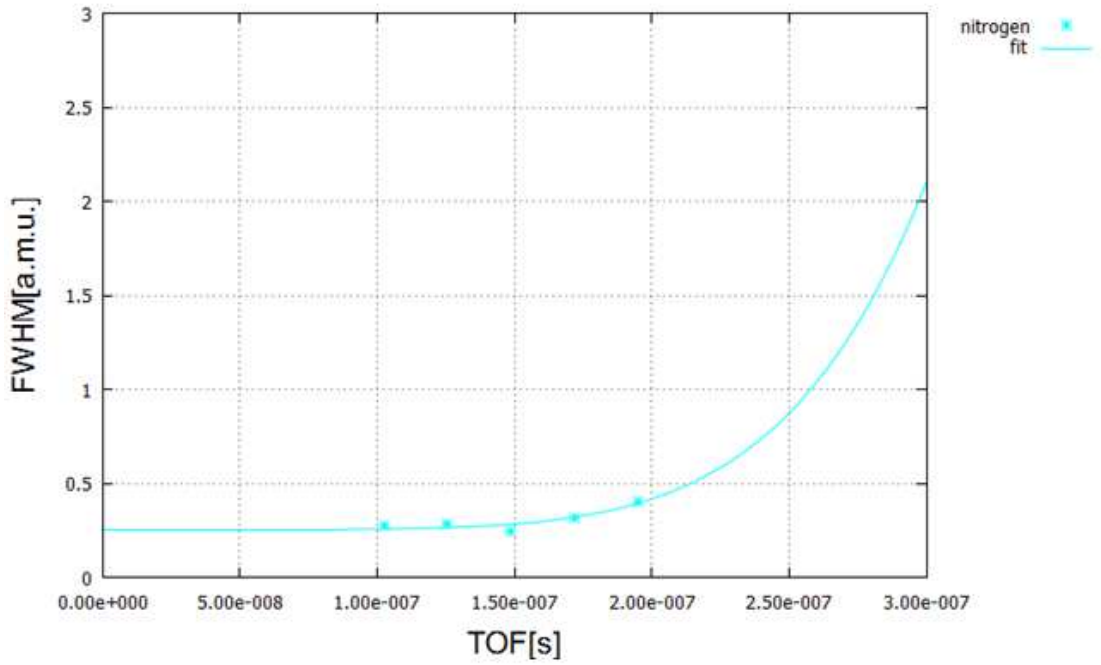

Figure 5-12 $\boldsymbol{FWHM_{MASS}}$ values calculated according to Eq. 5-7 are plotted as a function of $\boldsymbol{TOF}$ for nitrogen (cyan stars). $\boldsymbol{FWHM^{opt}_{MASS,sim}}$ as a function of TOF for nitrogen is plotted with the cyan line.

Substituting in Eq. 5-12 optimal C coefficients for nitrogen and as T the time of flight bins defined in Section 4.5.1, telescope length L and nitrogen mass M it was possible to simulate the optimal $FWHM^{opt}_{MASS,sim}$ values for each bin. Representation of $FWHM^{opt}_{MASS,sim}$ as a function of time of flight bins is in Figure 5-12 drawn with a line.

The same procedure described above was conducted not only for nitrogen, but for all calibration isotopes where we got $FWHM_{MASS}$ data. As said it was not possible to calculate $FWHM_{MASS}$ data

for isotope 6 of lithium, isotope 10 of boron, sodium and magnesium, thus the procedure was performed on eleven calibration isotopes: hydrogen, helium, isotope 7 of lithium, beryllium, isotope 11 of boron, carbon, nitrogen, oxygen, fluorine, aluminum and isotope 35 of chlorine.

Given that C coefficients are mass dependent, eleven sets of optimal C coefficients, one per isotope, are obtained in the $FWHM$ calibration.

During the FWHM calibration we obtained eight sets of optimal C coefficients, one per hydrogen, helium, isotope 7 of lithium, carbon, nitrogen, fluorine, aluminum and isotope 35 of chlorine. Thus eight $FWHM^{opt}_{MASS,sim} - TOF$ curves were simulated.

Representation of the eight isotopic $FWHM^{opt}_{MASS,sim} - TOF$ curves are showed in Figure 5-13 with lines, instead $FWHM_{MASS}$ calculated from data according to Eq. 5-7 are plotted as a function of TOF with stars and squares.

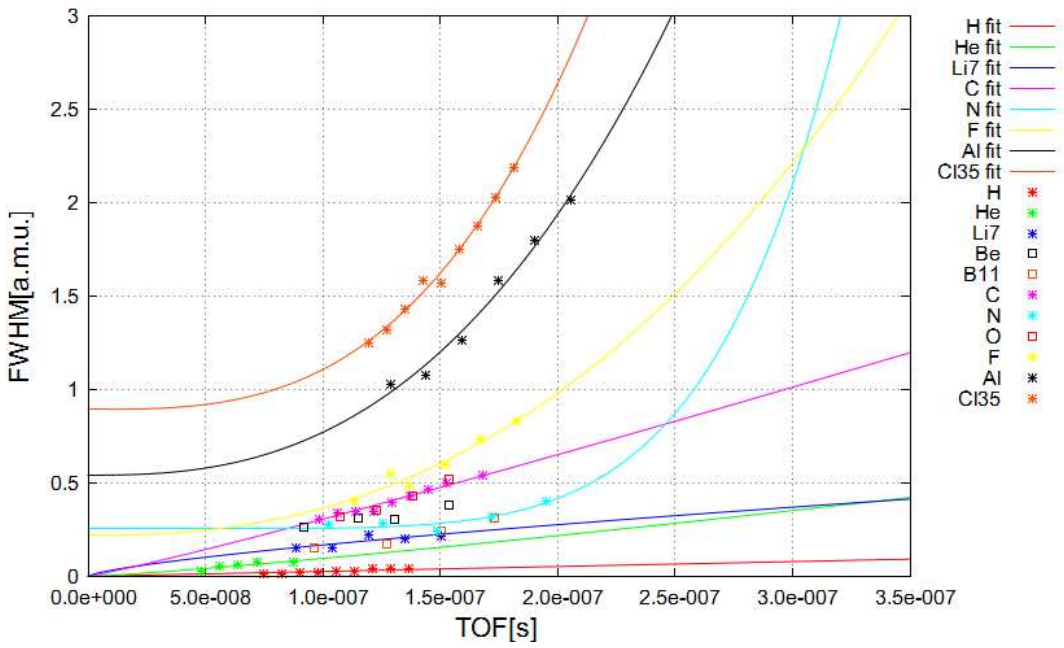

Figure 5-13 $\boldsymbol{FWHM_{MASS}}$ *values calculated according to Eq. 5-7 are plotted as a function of* $\boldsymbol{TOF}$ *for hydrogen, helium, lithium 7, beryllium, boron 11, carbon, nitrogen, oxygen, fluorine, aluminum and chlorine 35 (stars and empty squares).* $\boldsymbol{FWHM^{opt}_{MASS,sim}}$ *as a function of TOF for hydrogen, helium, lithium 7, carbon, nitrogen, fluorine, aluminum and chlorine 35 are plotted with lines.*

As visible in Figure 5-13 the optimal models $FWHM^{opt}_{MASS,sim} - TOF$, represented by lines, well reproduce $FWHM_{MASS} - TOF$ data, represented by stars and empty squares. Fits, as data, follow a mass dependence, which is not respected only for nitrogen low and high TOF regions.

Having calculated $FWHM^{opt}_{MASS,sim} - TOF$ curves for the eight isotopes it was chosen a fixed time of flight bin, $\overline{bin}$~$150ns$, and eight $FWHM^{opt}_{MASS,sim,\overline{bin}}$ were extracted. This is visible in Figure 5-14,

where the thin colorful lines represent $FWHM^{opt}_{MASS,sim} - TOF$ curves, the thick green line is set at $\overline{bin}$~$150ns$, so the intercepts of the thin curves with the green thick line are the eight $FWHM^{opt}_{MASS,sim,\overline{bin}}$ values extracted.

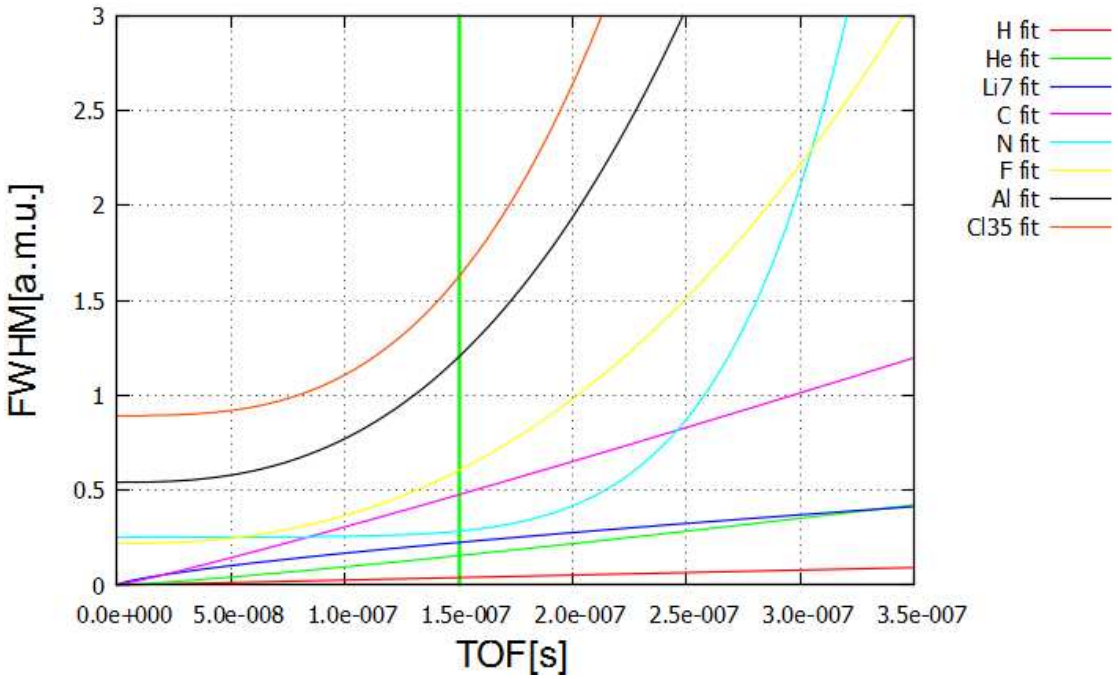

Figure 5-14 $\boldsymbol{FWHM^{opt}_{MASS,sim}}$ *as a function of TOF for hydrogen, helium, lithium 7, carbon, nitrogen, fluorine, aluminum and chlorine 35 are plotted with thin lines. The green thick line represents* $\boldsymbol{\overline{bin}}$**~150**$\boldsymbol{ns}$*. Intercepts of the green thick line with the thin lines are the eight* $\boldsymbol{FWHM^{opt}_{MASS,sim,\overline{bin}}}$.

These eight $FWHM^{opt}_{MASS,sim,\overline{bin}}$ values were plotted as a function of isotopic masses in Figure 5-15 marked with red crosses. From now on we will call $FWHM^{opt}_{MASS,sim,\overline{bin}}$ as $FWHM^{opt}_{MASS,sim,\overline{bin}}(TOF)$ to indicate that those values were calculated from Eq. 5-12.

A fitting model linear in its D coefficients was empirically determined:

$$FWHM_{MASS,sim}(M)[a.m.u.] = D1 + D2 * M + D3 * M^2$$

Eq. 5-13

Filling Eq. 5-13 with the eight isotopic masses M and arbitrary D_1, D_2 and D_3 one obtains eight simulated $FWHM_{MASS,sim,\overline{bin}}(M)$. A software was used in order to fit the linear model of Eq. 5-13 with data in Figure 5-15 marked with red crosses.

The fitting looks for $D_{1,opt}, D_{2,opt}$ and $D_{3,opt}$ coefficients that give the smallest error between $FWHM^{opt}_{MASS,sim,\overline{bin}}(TOF)$ and $FWHM^{opt}_{MASS,sim,\overline{bin}}(M)$. Representation of $FWHM^{opt}_{MASS,sim,\overline{bin}}(M)$ as a function of mass is in Figure 5-15 green line.

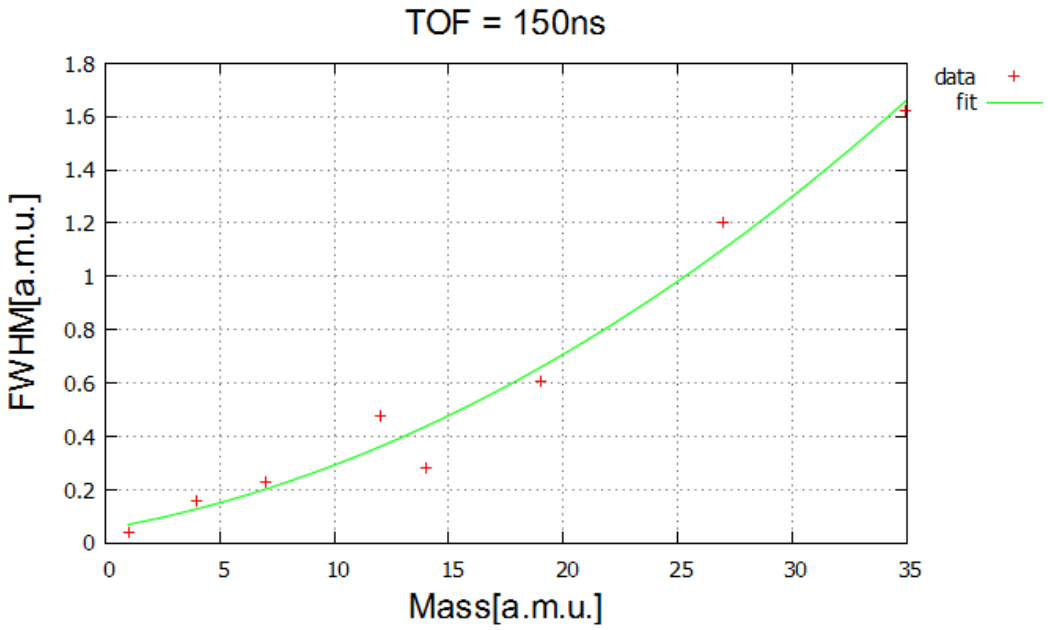

Figure 5-15 The eight $\boldsymbol{FWHM^{opt}_{MASS,sim,\overline{bin}}}$ *values extracted from Figure 5-14 for* $\boldsymbol{\overline{bin}\sim 150ns}$ *were plotted as a function of their isotopic masses (red stars).* $\boldsymbol{FWHM^{opt}_{MASS,sim,\overline{bin}}(M) - M}$ *curve obtained with optimal D coefficients for* $\boldsymbol{\overline{bin}\sim 150ns}$ *is plotted with the green line.*

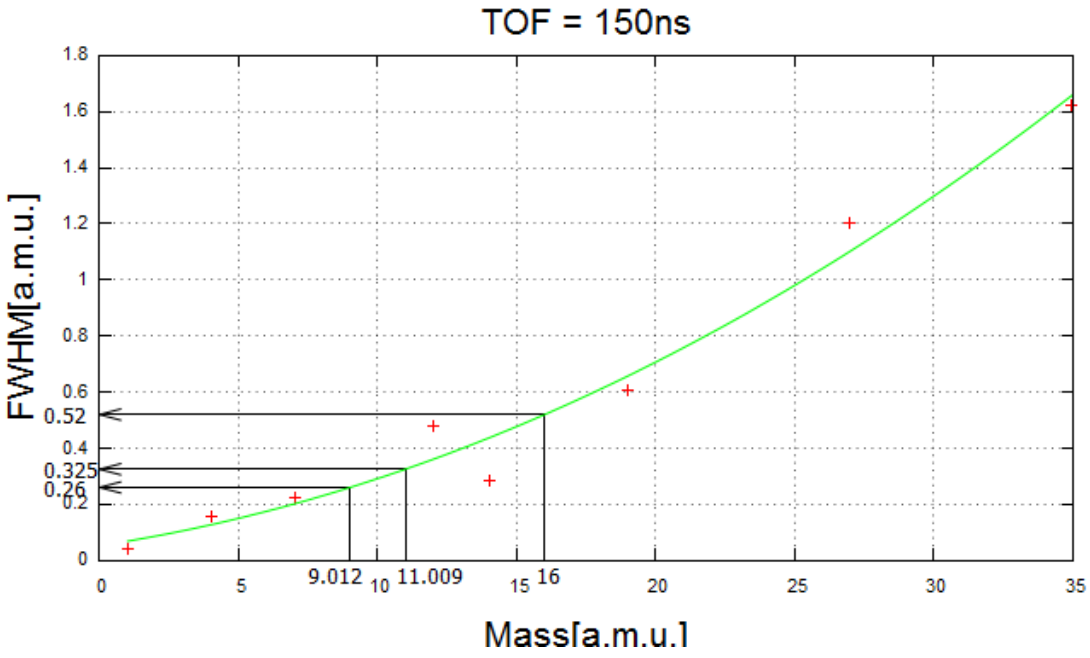

Figure 5-16 The eight $\boldsymbol{FWHM^{opt}_{MASS,sim,\overline{bin}}}$ *values extracted from Figure 5-14 for* $\boldsymbol{\overline{bin}\sim 150ns}$ *were plotted as a function of their isotopic masses (red stars).* $\boldsymbol{FWHM^{opt}_{MASS,sim,\overline{bin}}(M) - M}$ *curve obtained with optimal D coefficients for*

$\overline{bin}\sim 150ns$ is plotted with the green line. Extracted $FWHM^{opt}_{MASS,sim,\overline{bin}}(M)$ values from the green curve are pointed on the y-axis by black arrows for $\overline{bin}\sim 150ns$ for beryllium, boron 11 and oxygen.

It was possible to extract from Figure 5-15 $FWHM^{opt}_{MASS,sim,\overline{bin}}(M)$ for $\overline{bin}$ for beryllium, isotope 11 of boron and oxygen, where the program couldn't achieve C coefficients optimization.

Indeed in Figure 5-16 having isotopic masses of beryllium (9.012a.m.u.), boron 11(11.009a.m.u.) and oxygen (16a.m.u.) it was possible to extract from the green curve $FWHM^{opt}_{MASS,sim,\overline{bin}}(M)$ values for those isotopes (Figure 5-16 values on the y-axis pointed by black arrows).

$D_{1,opt}$, $D_{2,opt}$ and $D_{3,opt}$ coefficients are time bin dependent. Ideally moving the green thick line in Figure 5-14 through the whole x-axis it is possible to repeat the procedure described for $\overline{bin}$ to all the 8192 time bins, which we divided the x-axis in. Thus we obtain 8192 plots like Figure 5-15 and we get 8192 sets of optimal D coefficients.

Given the sets of optimal D coefficients for each time bin, it is possible to simulate the $FWHM^{opt}_{MASS,sim,bin}(M)$, according to Eq. 5-13, for each mass and time bin.

6 Element discrimination

In this last chapter of the thesis we will introduce a procedure that allows to discriminate isotopic abundances in each ERD experiment. This procedure is fully free from human eye errors and human inputs.

We will also present some future outlooks in order to improve the procedure and make it suitable even when not-common behavior of the data is observed.

6.1 Historical perspective

In chapter 5 we have already introduced Hult et al. [11] [13] [20] work on element discrimination, talking about energy detector resolution. The authors fitted mass spectra for narrow energy bins with Gaussian functions using a maximum likelihood method. In the case of multi-isotope targets the fitted function was the sum of a number of Gaussians with an area that corresponded to the isotope abundance and a position that corresponded to the isotopic mass. [11]

Hult et al. in [13] worked with an experimental setup consisting of a 738mm-telescope, 100mm^2 ion-implanted Si detector (SiTek), 64MeV $^{127}I^{11+}$ projectile ions with incident angle of 45°. Recoils from a $Al_xGa_{(1-x)}As$ sample were analyzed at recoil angle of 67.5°. The mass, M, was derived from the energy detector response E_{ch} and TOF, T, according to the model

$$M_{ch} = (T - T_0)^2 * 2E_{ch}/L^2$$

Eq. 6-1

Where T_0 is an adjustable constant which is selected to take care of electronic delays, etc [13]. Masses M_{ch} are not calibrated in [a.m.u.] (Figure 6-1), but in channels.

Elemental discrimination on mass data (Figure 6-1 crosses) is carried out thanks to the fitting shown in Figure 6-1 (continue line along crosses trend) for ^{69}Ga and ^{71}Ga and ^{75}As for the energy bin between 11.7 and 30MeV. The sum of three Gaussians, one for each sample isotope, was used in the fitting. The areas, positions and widths of the three Gaussians were left as free parameters in the fitting [13]. In Figure 6-1 the two inner lines represent gallium 69 and arsenic 75 fitted Gaussians.

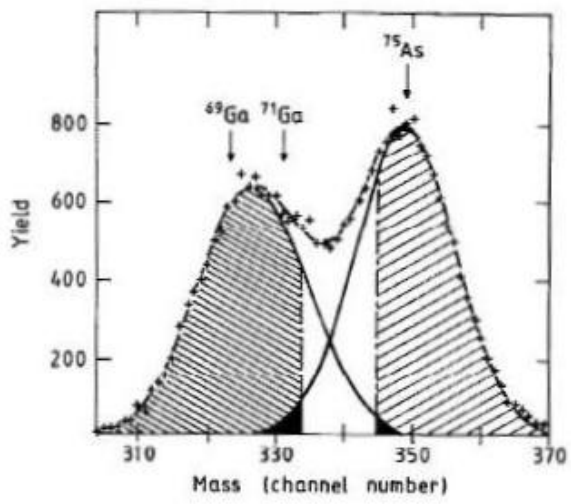

Figure 6-1 Recoil mass distribution from a Co-Ga-As reference sample for 11.7-30-MeV recoils (O-500nm depth in GaAs). The contributions from Ga and As have been determined by decomposition into three Gaussians. [13]

In Figure 6-1 gallium isotope 69 and arsenic isotope 75 peaks of the fitting Gaussians are distinguishable by human eye, although their tails are overlapped. On the other hand gallium isotope 71 peak of the fitting Gaussian is not distinguishable by human eye, because of its lower natural abundance with respect to gallium isotope 69.

On the basis of the fit indicated in Figure 6-1, the mass windows for Ga and As were chosen. These windows are marked by hatching in Figure 6-1 and cover 83% and 74% of the Ga and As areas, respectively, with less than 2% crosstalk (indicated in black) [13]. The fitted function describes well the low- and high-mass flanks of the Ga and As peaks, respectively [13].

The effect of small variations in the position and width of the isotope peaks with recoil energy was checked by sorting the data to yield mass spectra for small recoil energy slices. The crosstalk, determined using the procedure above, increased with decreasing recoil energy (greater depth) from ~0.5% at the surface to ~2% and ~4.5% for Ga and As, respectively, at a depth corresponding to 500 nm in GaAs [13].

Data from the mass-energy histogram for the $Al_xGa_{(1-x)}As$ sample was then sorted using the mass windows for Ga and As indicated in Figure 6-1(hatching) to yield TOF distributions for ^{27}Al, $^{69\text{-}71}Ga$, and ^{75}As recoils [13].

These TOF distributions were subsequently transformed to energy distributions with assumed masses of 27.0, 69.8, and 75.0 a.m.u. for Al, Ga, and As, respectively (Figure 6-2). The recoil TOF was used to define the energy, rather than the silicon particle detector signal, because of the superior energy resolution attainable [13].

The main limitation of this approach seems to be that masses are not calibrated in [a.m.u.] (Figure 6-1), but in channels, thus one needs to know a priori the elements present in the sample in order to extract the TOF distributions.

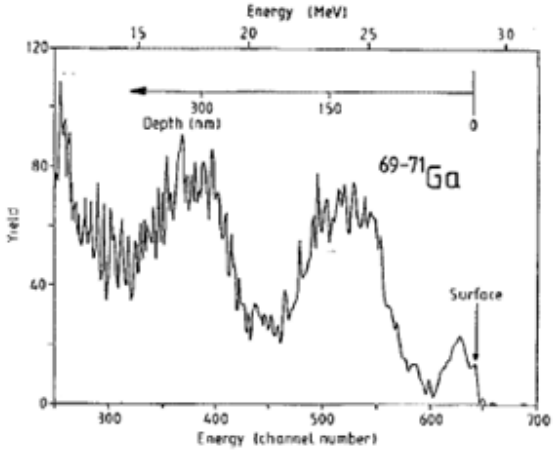

Figure 6-2 Energy distributions for $^{69-71}$Ga where the energy has been derived using the recoil time of flight. The depth scale is derived from the known structure of the sample [13].

Another contribution to elemental discrimination is the one from Kottler et al. [19].

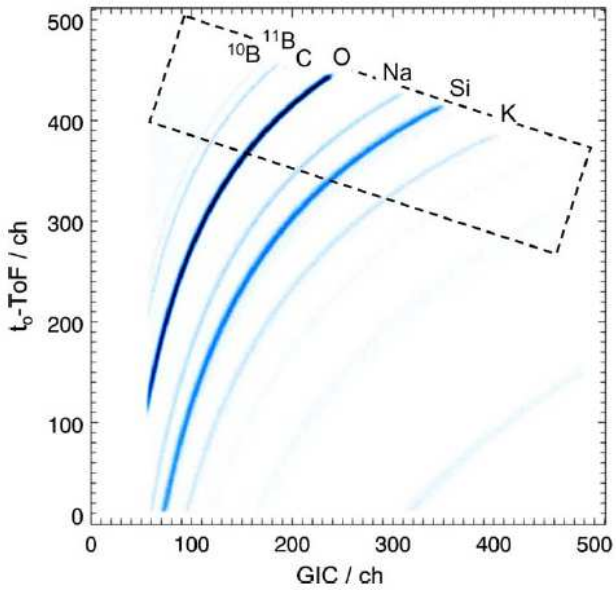

Figure 6-3 ToF versus energy histogram of the ERDA measurement of a borosilicate glass surface using 12 MeV ^{127}I projectiles. The ToF axis is inverted [19].

Authors analyzed a borosilicate glass surface using 12 MeV ^{127}I projectiles and a gas ionization detector. They adopted Mallepell empirical model (Eq. 4-9) to transform each pair of data (TOF, E_{ch}) in the area delimited by the dashed line in Figure 6-3 into (TOF, M) pairs.

As an example, the mass spectrum of the events inside the selected area indicated in Figure 6-3 is shown in Figure 6-4. By fitting the mass peaks with a Gaussian the mass resolution ΔM (FWHM) was determined.

In order to demonstrate the sensitivity of the spectrometer to trace elements the peak from the ^{18}O isotope ($^{18}O/^{16}O$ = 0.2%) is shown as a magnified section in the left inset of Figure 6-4. Although this peak is sitting on the smooth tail of the much stronger ^{16}O signal the two oxygen isotopes are clearly separated [19].

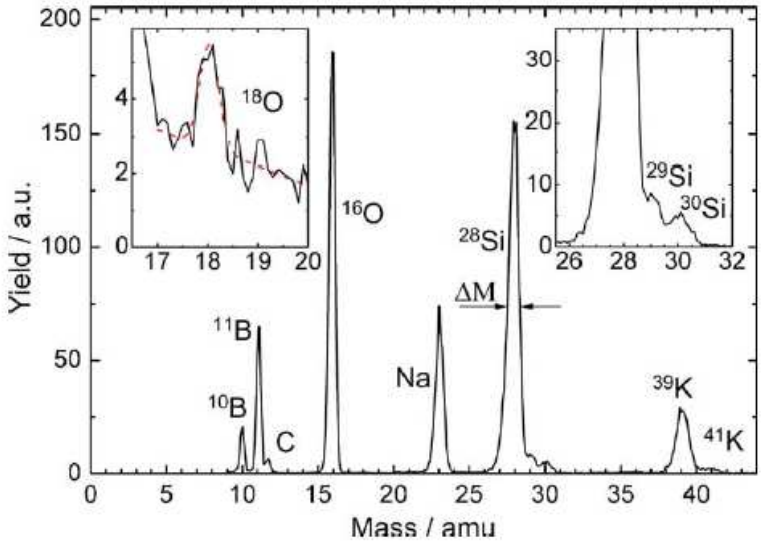

Figure 6-4 Mass spectrum obtained by conversion of the marked region in the 2-D ERDA spectrum shown in Figure 6-3. Insets demonstrate the separation of oxygen and silicon isotopes [19].

The third contribution to elemental discrimination comes from Persson et al. [9]. The authors consider a one-dimensional mass spectrum vector S with channel contents S_i and associated statistical weight w_i. Each vector S corresponds to an energy slice a single energy bin wide.

The least squares fit of a function $f_i(a,i)$ that is linear in its parameters a_k can be written in the form of the matrix equation:

$$\alpha a = \beta S$$

Eq. 6-2

where a is the vector of adjustable parameters a_k, and the matrices α and β have elements

$$\alpha_{jk} = \sum_i w_i^{-1} \beta_{ji} \beta_{ki}$$

Eq. 6-3

$$\beta_{ji} = w_i \left(\frac{\partial f_i(a,i)}{\partial a_j} \right)$$

Eq. 6-4

[9].

Vector a is then given by

$$a = \alpha^{-1}\beta S = \Gamma S$$

Eq. 6-5

where $\Gamma = \alpha^{-1}\beta$ [9].

$f_i(a, i)$ is made up of the sum of Gaussian line-shape functions $f_k(i)$ corresponding to the k constituents

$$f_i(a, i) = \sum_k a_k f_k(i)$$

Eq. 6-6

Each Gaussian line-shape $f_k(i)$ has the centroid corresponding to the nominal mass A of the kth isotope and $\sigma(E, A)$ obtained thanks to Eq. 5-7 [9].

The authors gave unity weights w_i, thus no assumptions has to be made regarding the concentration of the different elements present in the sample [9].

Vector a can be evaluated by applying the matrix transformation in Eq. 6-5, provided the Gaussians $f_k(i)$ and the mass spectrum S are known. So fixing the values of the centroid and the standard deviation of each Gaussian it is possible to obtain from the matrix transformation the abundance a_k of the kth isotope. Matrix Γ in Eq. 6-5 describes how much the channel content S_i contribute to each a_k [9].

Simulations were carried out in order to test the goodness of the model. One significant test was made for the case of rectangular energy distributions of palladium, indium and iodine with elemental yield ratio respectively 2:10:10 and a total Pd yield of 200 counts.

Authors found that using Gaussian distributions to represent the isotope mass line-shapes and treating the abundance of the isotopes as free parameters, the different isotopic distributions exhibited wild fluctuations [9] especially in the low energy range (Figure 6-5a).

In order to improve the situation the number of free parameters was reduced by assigning the line-shape function $\mathrm{f_k(i)}$ for each element rather than for each isotope. After this modification the agreement with the rectangular test data was found to be excellent (Figure 6-5b) [9]. Indeed in Figure 6-5b it is represented the fitted Pd total signal yield composed by line-shape Gaussians with isotopic abundance fixed at the natural nominal values and nominal mass of each Pd isotope.

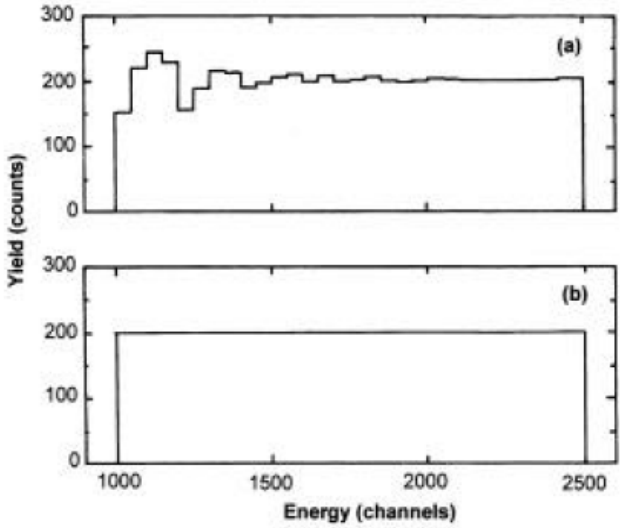

Figure 6-5 (a) The sum of fitted total signal yields from all Pd isotopes when a single Gaussian line-shape function is fitted independently for each isotope. (b) The fitted Pd total signal yield when a composite line-shape comprising Gaussians corresponding to the nominal natural abundance and mass of each Pd isotope was fitted. [9]

The assignment of a line-shape function to each element instead of each isotope is preferred because this minimizes uncertainties associated with counting statistics and numerical rounding errors [9].

Another challenge faced by the authors was the limit of low counting statistics [9], when dealing with few number of events in energy slice a single energy bin wide. Thus the simulated two dimensional spectrum (mass-energy histogram) was multiplied by a random factor [9].

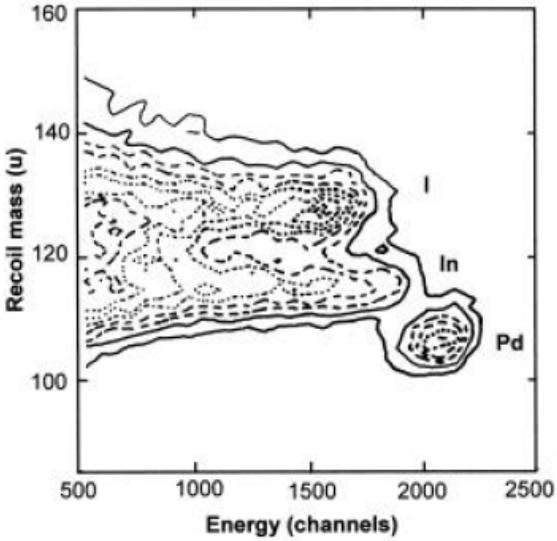

Figure 6-6 Mass number-energy histogram for 50nmPd/InP in the Pd-In-I region. The contour lines are drawn at ten equally spaced yield intervals. [9]

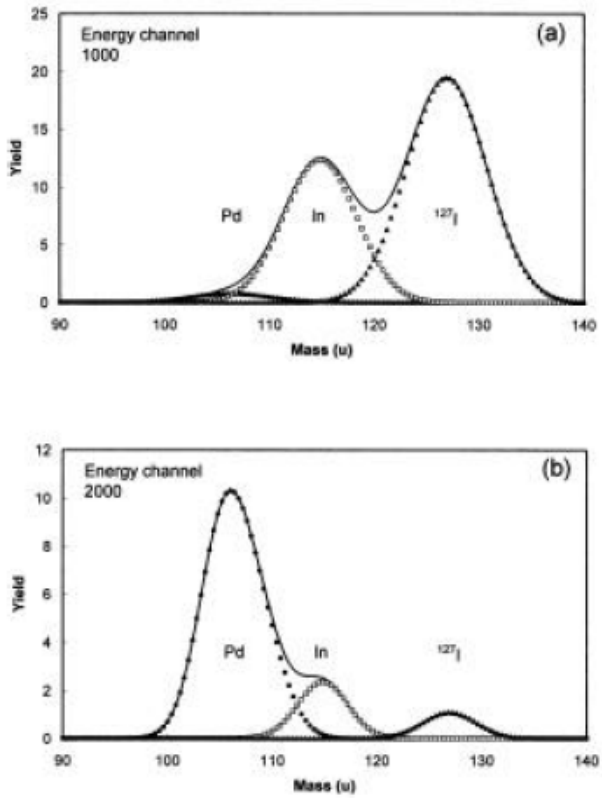

Figure 6-7 Fitted mass line-shapes corresponding to the mass-energy data in Figure 6-6 for energy channels in the InP substrate (a) and Pd surface film (b). [9]

Experimental measurements were done using a 77MeV $^{127}I^{10+}$ ion beam, with incident angle 60°. Recoils were ejected at 45° to the beam direction and detected in a 437.5mm-long telescope. The sample analyzed was ~50nm of Pd layer on a InP substrate. The data were transformed to a two-dimensional mass energy spectrum (Figure 6-6) following the mass assignment procedure by El Bouanani et al. in Eq. 4-6 [9].

Figure 6-7 presents the fitted mass line-shapes corresponding to energy channel 2000 (Figure 6-7b Pd film) and channel 1000 (Figure 6-7a deep in the InP substrate). The thin surface layer of Pd was clearly resolved [9].

Although Persson et al. obtained element discrimination, the main limit of the procedure is the lack in isotopic discrimination. Indeed in Figure 6-7b (Pd film) no Pd isotopes are discriminated.

Another drawback is that the nature of the method implies that the $f_k(i)$ functions used for the spectral decomposition have to be established accurately otherwise uncertainties will be introduced into the elemental distributions [9]. Thus fixing the mass position of each Gaussian to the nominal value it is not possible to take into account irradiation damage mass shifts (section 4.2).

6.2 Experimental results

In this section we will analyze experimental results coming from IMEC setup. Data elaboration is conducted according to a newly developed procedure, called 'decomposition'. It allows to discriminate isotopic abundances in a ERD experiment even when different elemental signals have overlapping regions in the TOF-Mass histogram.

6.2.1 Maximum likelihood method

In Section 5.2 we assumed that mass spectra have a Gaussian distribution, in order to estimate from data the FWHM. We will now investigate on this hypothesis.

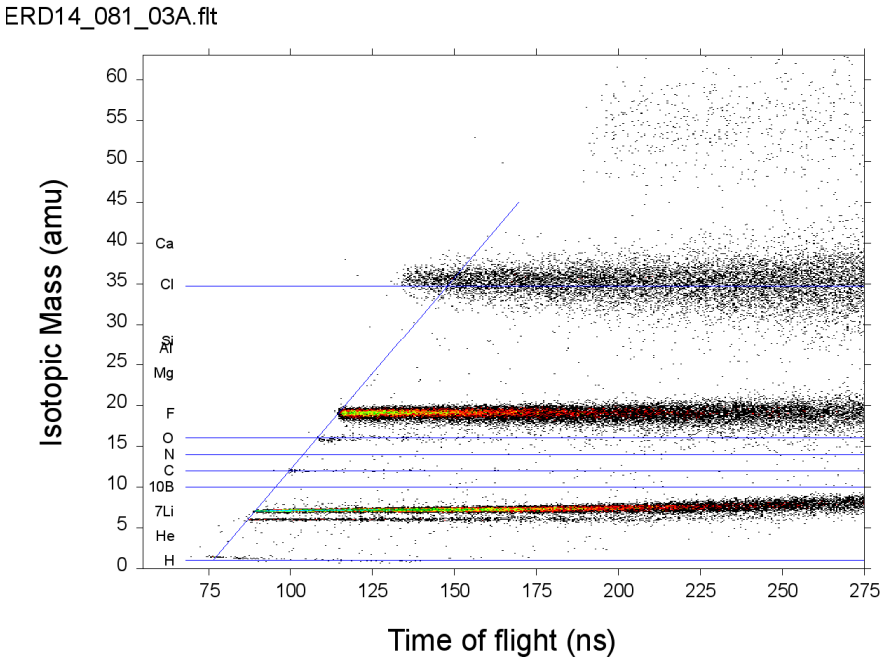

Figure 6-8 TOF-Mass histogram for LiF calibration sample analyzed with the IMEC setup. Apart from major sample elements like isotopes 6 and 7 of lithium and fluorine, also hydrogen, carbon and oxygen are present as small contaminations and chlorine 35 as scattered product from the ERD experiment.

The idea is to fit the mass spectra for each time bin with a 'composition' of Gaussian functions. In order to do that the least square fit described in Section 4.5.1 is no longer useful because of the low counting statistics.

Indeed as described by Hauschild et al. ([21] and references therein) the least squares method, which uses Eq. 4-13 to calculate CHI, is only attainable when at least 5 counts are in every bin. Otherwise adjacent bins must be combined, but it washes out the fine structure that may contain valuable information [21].

One calibration sample was made of lithium (isotope 6 and 7) and fluorine with some other contaminations (e.g. carbon, oxygen and hydrogen) as it is shown in Figure 6-8. The mass spectrum, as (M, Y) pair data, for $TOF = 150ns$ is shown in Figure 6-9. From Figure 6-9 we can see that in most cases mass bins contain less than 5 counts.

When less than 5 counts are present in every bin the maximum likelihood method can be a solution. An intuitive way of extracting information from measured data is to ask the question whether it is probable that the data have occurred given a set of parameters and a model. The idea of maximum likelihood estimation (MLE) is to maximize this probability called "likelihood" [21].

The likelihood L is given by the combined probability of measuring a set of Y_i counts at positions x_i where the model predicts $m_a(x_i)$ [21]. If the model m_a depends on the parameters a_j then the likelihood L needs to be maximized with respect to these parameters in order to find their optimum values [21].

If the measurements are Poisson distributed (counting experiments) the Poisson likelihood L_p is

$$L_p(a) = \prod_i \frac{[m_a(x_i)]^{Y_i}}{Y_i!} e^{-m_a(x_i)}$$

Eq. 6-7

It is easier to use the logarithm of this expression [21]

$$-2lnL_p(a) = 2\sum_i [m_a(x_i) - Y_i ln\, m_a(x_i)]$$

Eq. 6-8

Minimizing $-2lnL_p$ leads to the same parameters as maximising L_p [21].

An algorithm was implemented to fit mass spectra data (M_i, Y_i) with Gaussian distributions according to the maximum likelihood method, thus minimizing Eq. 6-8.

The model is

$$m_a(x_i) = \frac{A}{\sigma\sqrt{2\pi}} e^{-\frac{(x_i-\mu)^2}{2\sigma^2}}$$

Eq. 6-9

which adapted to mass spectra becomes

$$m_a(x_i) = Y_{sim}(M_i) = \sum_k \left(\frac{A_k}{\sigma\sqrt{2\pi}} e^{-\frac{(M_i-M_{el,k})^2}{2\sigma^2}}\right)$$

Eq. 6-10

where k are the isotopes present in the sample, Y_{sim} is the simulated yield, σ is the mass standard deviation obtained from $FWHM_{MASS}$ calibration for any mass and time bin (Section 5.3), A_k is the area of the Gaussian function, $M_{el,k}$ is the isotopic mass and M_i the recoil mass data in Figure 6-9.

Thus the model in Eq. 6-10, which will fit the mass spectra data, is the 'composition' of k Gaussian functions, as many as the isotopes in the samples.

The free parameters in Eq. 6-10 are A_k and $M_{el,k}$. Indeed we want to know A_k, which indicates the abundance of each isotope in a sample and $M_{el,k}$, the experimental isotopic mass.

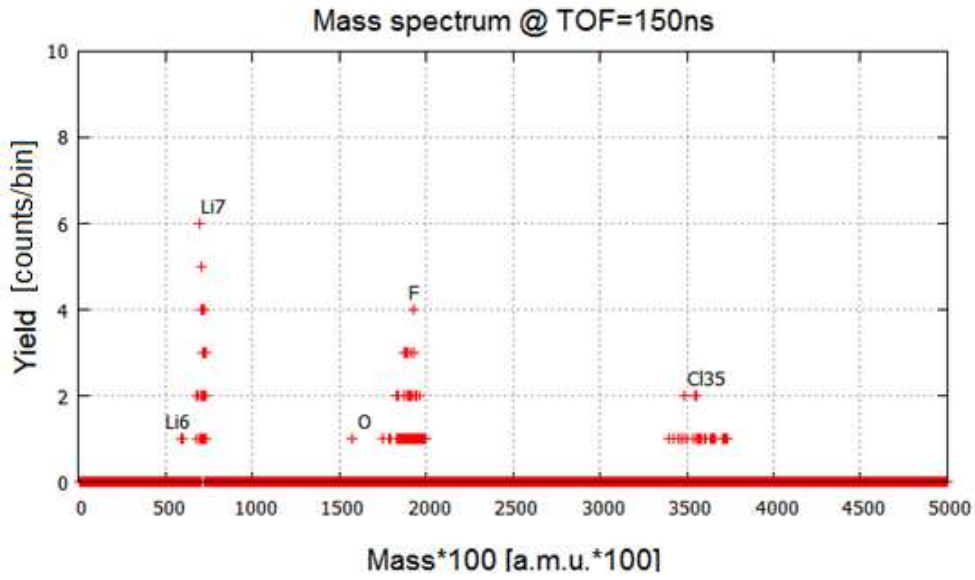

Figure 6-9 Mass spectrum with recoil data at TOF=150ns for LiF calibration sample analyzed with the IMEC setup. Apart from major sample elements like isotopes 6 and 7 of lithium and fluorine, also oxygen is present as small contamination and chlorine 35 as scattered product from the ERD experiment.

The experimental isotopic mass is left free to take into account radiation damage shift in the mass transformation. For this reason the experimental isotopic mass can shift from the nominal isotopic mass due to heavy particles hitting the silicon detector.

The abundance A_k is left as a free parameter for each isotope because it is not correct to fix it to the natural isotopic abundance reported in theory.

Indeed for the case showed in Figure 6-9 we could fix lithium 6 abundance as 7.5% of the total lithium abundance, but we shall consider that the recoil cross-section decreases with recoil mass (Eq. 2-29). Thus for the heavier lithium 7 we will have smaller recoil cross-section and less recoil yield compared to the lighter lithium 6, as the recoil cross-section is proportional to the recoil yield (Eq. 2-15).

Another reason to leave A_k as free parameter for each isotope is explained in Figure 6-9 by the blue oblique line. The line represents the surface recoil TOF as a function of mass obtained as

$$T_s = L(M_1 + M_2)\sqrt{\frac{1}{8M_1 COS^2\varphi E_0}}$$

Eq. 6-11

where M_1, M_2, E_0 and φ are respectively the projectile mass, the recoil mass, the hitting ion energy and the recoil angle. T_s is proportional to recoil mass, thus the heavier lithium 7 has a higher T_s compared to lithium 6.

If we want to analyze lithium at the sample surface the time bins to be considered for lithium 6 and 7 are not the same, but shifted.

For these two reasons the discrimination should be conduct isotopically-separated.

The algorithm looks for optimal A_k and $M_{el,k}$ parameters, in order to minimize Eq. 6-8, when we substitute $m_a(x_i)$ with Eq. 6-10, and Y_i with yield data in Figure 6-9.

Looking for optimal A_k and $M_{el,k}$ for each time bin we will achieve isotopic abundance discrimination for the whole TOF-mass histogram (Figure 6-8). From now on we will call this isotopic abundance discrimination procedure as 'decomposition'.

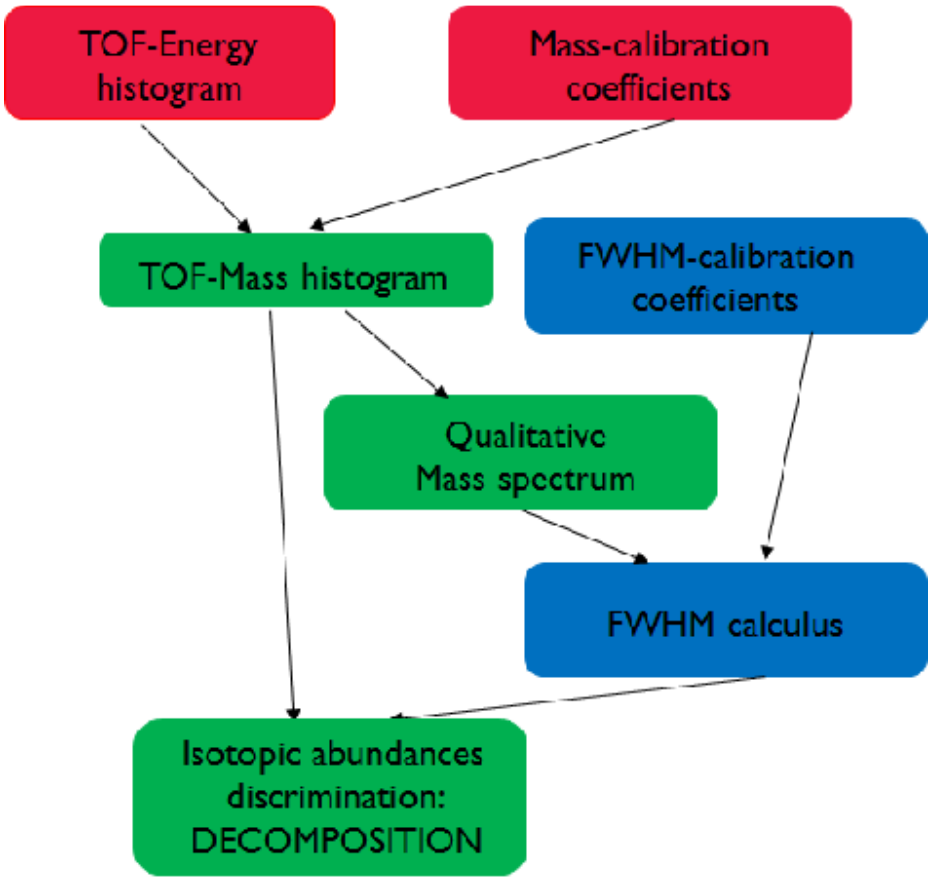

Figure 6-10 Flow chart indicating the various steps needed to achieve abundance decomposition on an ERD experiment.

The decomposition should be attainable even in the high TOF region, where the mass-bananas broadening is heavy, thus isotopic discrimination is not achievable by human eye.

In Figure 6-10 it is shown a flow chart explaining the various steps to reach the abundance 'decomposition' on an ERD experiment.

First we acquire data on a TOF-Energy histogram, then thanks to B coefficients, varying for each TOF bin, we are able to transform each pair data $(TOF; E)$ into pair data $(TOF; M)$ according to Eq. 4-15. With $(TOF; M)$ data we can plot the TOF-Mass histogram and a qualitative mass spectrum, like in Figure 6-9.

At this point thanks to D coefficients, varying for each TOF bin, we are able to calculate for each mass data its $FWHM_{MASS}$ value according to Eq. 5-13.

Finally feeding the decomposition algorithm with $FWHM_{MASS}$ values and $(TOF; M)$ data we can achieve abundance decomposition in each TOF bin.

6.2.2 Integrated spectrum decomposition

We will first analyze the decomposition procedure on a time integrated spectrum, thus when the yield is still quite high for each isotope. In the next section we will investigate on the case of low counting statistics, thus on time bins spectra.

The decomposition was performed on a calibration sample made of Al_2O_3.

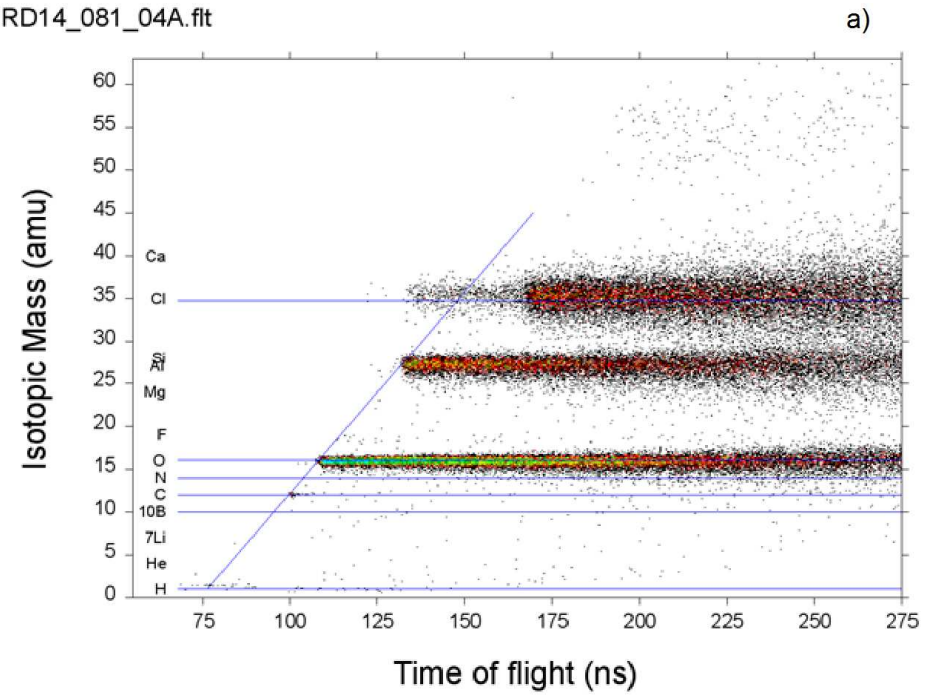

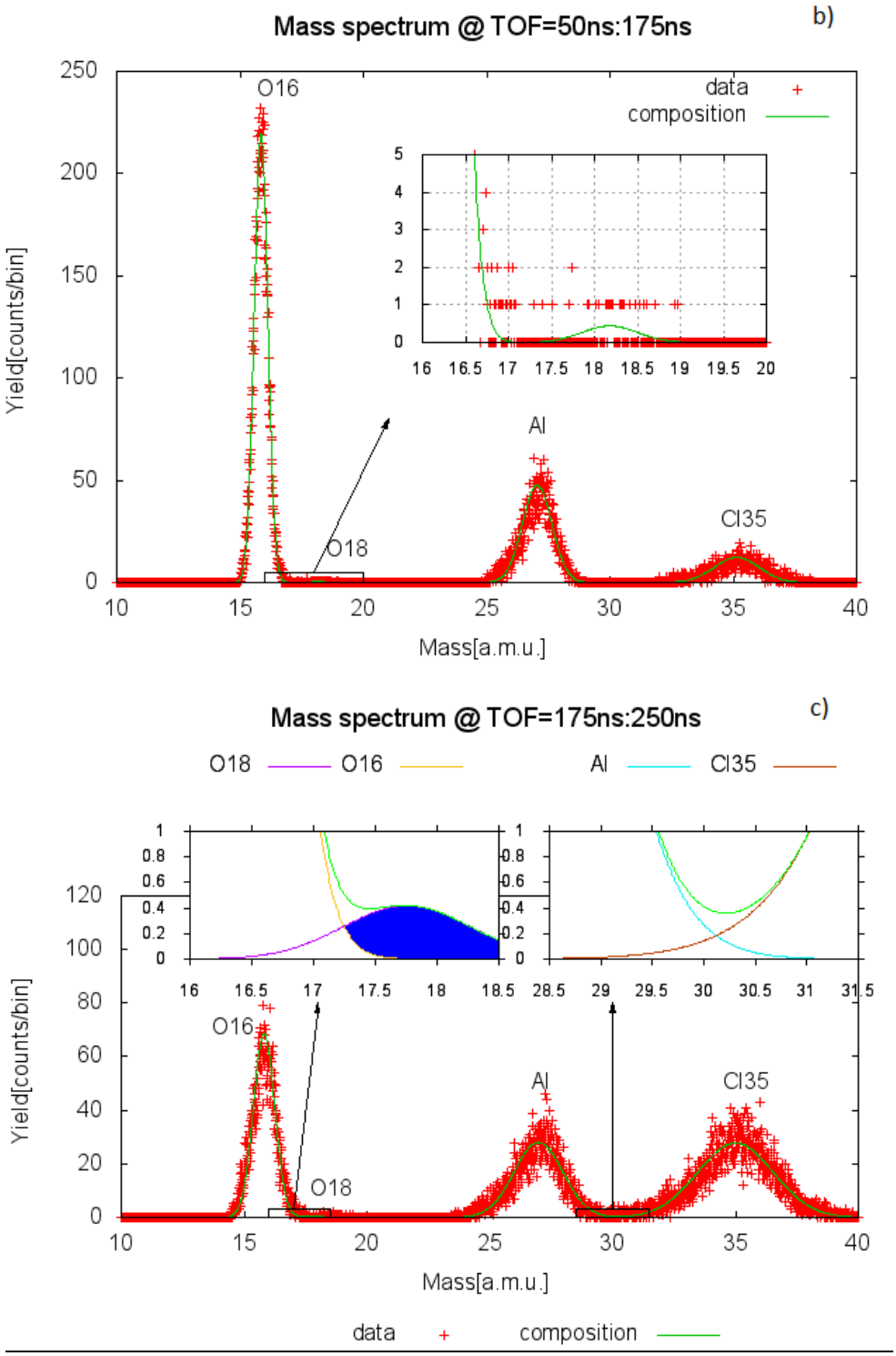

Figure 6-11 a) TOF-Mass histogram for the Al_2O_3 calibration sample analyzed with the IMEC setup. Apart from major sample elements like oxygen and aluminum, also hydrogen and carbon are present as small contaminations and chlorine 35 as scattered product from the ERD experiment. b) Integrated time mass spectrum in the TOF region between 50ns and 175ns. In red recoil data are plotted, the green line represents the composition of the four optimal Gaussians corresponding to oxygen 16 and 18, aluminum and chlorine 35. In the insert the resolution of oxygen 18 is shown. c)

Integrated time mass spectrum in the TOF region between 175ns and 250ns. In red recoil data are plotted, the green line represents the composition of the four optimal Gaussians corresponding to oxygen 16 and 18, aluminum and chlorine 35. Inserts show in yellow, purple, cyan and brown respectively decomposed Gaussians for oxygen 16, 18, aluminum and chlorine 35. In blue the overlapping regions of data respectively for the isotopic couples oxygen 16-18 and aluminum-chlorine 35.

To perform the integrated time decomposition on the Al_2O_3 calibration sample we select the events comprised between TOF=50ns and TOF=175ns and between TOF=175ns and TOF=250ns in Figure 6-11a.

We can plot the time integrated mass spectrum for the sample in these two TOF regions, respectively Figure 6-11b and Figure 6-11c (red crosses). In the analysis we exclude contaminations of carbon and hydrogen.

Results of the decomposition procedure in these two TOF regions are shown respectively in Figure 6-11b and Figure 6-11c (lines) and tabulated respectively in Table 6-1 and Table 6-2 (rows 3 and 4).

The green line in Figure 6-11b-c is the optimized model expressed in Eq. 6-10, thus the composition of the four optimal Gaussians corresponding to oxygen 16 and 18, aluminum and chlorine 35. Each optimal Gaussian has an area $\mathrm{A_{k,sim}}$ and a centroid $\mathrm{M_{el,k}}$, those values are reported for both TOF regions in Table 6-1 and Table 6-2 rows 3 and 4.

In the TOF region between 50ns and 175ns it's possible to distinguish $\mathrm{A_k}$ separately for each isotope. Decomposed isotopic $\mathrm{A_{k,sim}}$ and $\mathrm{M_{el,k}}$ in Table 6-1 are compared respectively to the isotopic yield, $\mathrm{A_k}$, obtained considering the counts in the 99.9% of each isotopic Gaussian and nominal isotopic masses $\mathrm{M_{nom}}$ (Table 6-1 rows 1 and 2).

Decomposition results are in good agreement with data as showed in Figure 6-11b and Table 6-1. The decomposition procedure developed allows to discriminate in this TOF region isotope 18 of oxygen (insert in Figure 6-11b), as already achieved by Kottler et al. (Figure 6-4).

Furthermore over a large TOF region, like between 50ns and 175ns, the procedure returns oxygen 16 and 18 abundances so that their ratio is ~0.2% as the theoretic value is. This ratio could not be as the theoretic one when going to time bin spectrum decomposition for the reasons explained in Section 6.2.1.

In the TOF region between 175ns and 250ns, where data overlap, the decomposition procedure allows to discriminate isotope 18 of oxygen and to separate aluminum from chlorine 35. This is showed in Figure 6-11c inserts. The blue areas represent the overlapping areas both for oxygen 16-18 and aluminum-chlorine35. The decomposed Gaussians for oxygen 16, 18, aluminum and chlorine are shown respectively in yellow, purple, cyan and brown. The decomposed Gaussians have area $\mathrm{A_{k,sim}}$ and centroid $\mathrm{M_{el,k}}$ listed in Table 6-2 rows 3 and 4.

The fact that this procedure allows to discriminate oxygen isotope 18 even in this critical TOF area where data overlap can be considered as an improvement comparing this procedure with results by Kottler et al. [19] showed in Figure 6-4.

In this TOF region it's not possible anymore to distinguish abundance data $\mathrm{A_k}$ separately for oxygen 16 and 18 which have overlapped data and even for aluminum and chlorine 35 (Figure 6-11a). Thus in Table 6-2 row 1 we consider combined abundance data $\mathrm{A_{k,comb}}$ for oxygen16-18 and aluminum-chlorine35.

On the other hand the procedure is able to discriminate separately the abundances $\mathrm{A_{k,sim}}$ of oxygen 16 and 18, aluminum and chlorine35.

To test the goodness of the procedure in this TOF region we can sum the decomposition abundance results $\mathrm{A_{k,sim}}$ (Table 6-2 row 3) both for oxygen16-18 and aluminum-chlorine35. We get good agreement with combined abundance data $\mathrm{A_{k,comb}}$ (Table 6-2 row 1).

TOF=50ns:175ns	O16	O18	Al	Cl35
A_k	15079	32	7118	2808
M_{nom}[a.m.u.]	15.994	17.999	26.981	34.968
$A_{k,sim}$	15077	35.786	7118	2808
$M_{el,k}$ [a.m.u.]	15.851	18.177	27.043	35.138

Table 6-1 Tabulated results of the decomposition procedure performed on the Al_2O_3 calibration sample analyzed with the IMEC setup within the TOF region between 50ns and 175ns. Rows 1 and 3 list data abundances and simulated ones for each isotope in the analysis. Row 2 lists the nominal mass of each isotope, instead row 4 lists the decomposed one, which is the centroid of each isotopic Gaussian.

TOF=175ns:250ns	O16 + O18	Al + Cl35
$A_{k,comb}$	7434	17581
M_{nom}[a.m.u.]	15.994 & 17.999	26.981 & 34.968
$A_{k,sim}$	7388.1 + 53.937= 7442	6960.3 + 10626= 17586
$M_{el,k}$ [a.m.u.]	15.807 & 17.755	26.98 & 34.998

Table 6-2 Tabulated results of the decomposition procedure performed on the Al_2O_3 calibration sample analyzed with the IMEC setup within the TOF region between 175ns and 250ns. Rows 1 and 3 list data abundances and simulated ones for each isotope in the analysis. Row 2 lists the nominal mass of each isotope, instead row 4 lists the decomposed one, which is the centroid of each isotopic Gaussian.

6.2.3 Time bin spectrum decomposition

To perform time bin spectrum decomposition it was observed that at least 200 counts were needed in each time bin mass spectrum (Figure 6-9), to make the maximum likelihood method converge. Since we divided the xaxis of the mass spectra in 5000 mass bins, most of the mass bins will have zero counts. In this situation maximum likelihood method is strongly advisable.

Time bins were re-binned in order to have at least 200 counts in the correspondent mass spectrum, thus the time bin definition given in Section 4.5.1 doesn't hold anymore. In the region of the TOF-Mass histogram where we have the major concentration of events (100ns : 200ns), typically one newly defined time bin is 0.5ns wide.

From now on we will call these new time bins 'TOF', knowing that each of them has typically a resolution of 0.5ns in the region of major interest.

We perform, as an example, the time bin spectrum decomposition on the Al_2O_3 sample for two different mass spectra at TOF=150 ns and TOF=245 ns. This two time bins were strategically chosen to show decomposition in a region were overlapping is not much affecting data, and in a region where data overlapping is a challenge.

We can plot the time bin mass spectrum for the sample in these two time bins, respectively Figure 6-12a and Figure 6-12b (red crosses). In the analysis we exclude contaminations of carbon and hydrogen.

Results of the decomposition procedure for these two TOF are shown respectively in Figure 6-12a and Figure 6-12b (lines) and tabulated respectively in Table 6-3 and Table 6-4(rows 3 and 4).

The green line in Figure 6-12a-b is the optimized model expressed in Eq. 6-10, thus the composition of the four optimal Gaussians corresponding to oxygen 16 and 18, aluminum and chlorine 35. Each optimal Gaussian has an area $A_{k,sim}$ and a centroid $M_{el,k}$, those values are reported for both TOF in Table 6-3 and Table 6-4 rows 3 and 4.

TOF=150ns	O16	O18	Al	Cl35
A_k	118	0	87	11
M_{nom}[a.m.u.]	15.994	17.999	26.981	34.968
$A_{k,sim}$	118	0.10647	87	11
$M_{el,k}$ [a.m.u.]	15.848	17.802	26.963	35.169

Table 6-3 Tabulated results of the decomposition procedure performed on the Al_2O_3 calibration sample analyzed with the IMEC setup at TOF=150ns. Rows 1 and 3 list data abundances and simulated ones for each isotope in the analysis. Row 2 lists the nominal mass of each isotope, instead row 4 lists the decomposed one, which is the centroid of each isotopic Gaussian.

TOF=245ns	O16 + O18	Al + Cl35
A_k	45	169
M_{nom}[a.m.u.]	15.994 & 17.999	26.981 & 34.968
$A_{k,sim}$	43.703 + 1.4432 = 45.14	71.014 + 97.986 = 169
$M_{el,k}$ [a.m.u.]	15.807 & 17.755	26.98 & 35.38

Table 6-4 Tabulated results of the decomposition procedure performed on the Al_2O_3 calibration sample analyzed with the IMEC setup at TOF=245ns. Rows 1 and 3 list data abundances and simulated ones for each isotope in the analysis. Row 2 lists the nominal mass of each isotope, instead row 4 lists the decomposed one, which is the centroid of each isotopic Gaussian.

At TOF=150 ns it's possible to distinguish A_k separately for each isotope. Decomposed isotopic $A_{k,sim}$ and $M_{el,k}$ in Table 6-3 are compared respectively to isotopic yield, A_k, obtained considering the counts in the 99.9% of each isotopic Gaussian and nominal isotopic masses M_{nom} (Table 6-3 rows 1 and 2).

Decomposition results are in good agreement with data as showed in Figure 6-12a and Table 6-3.

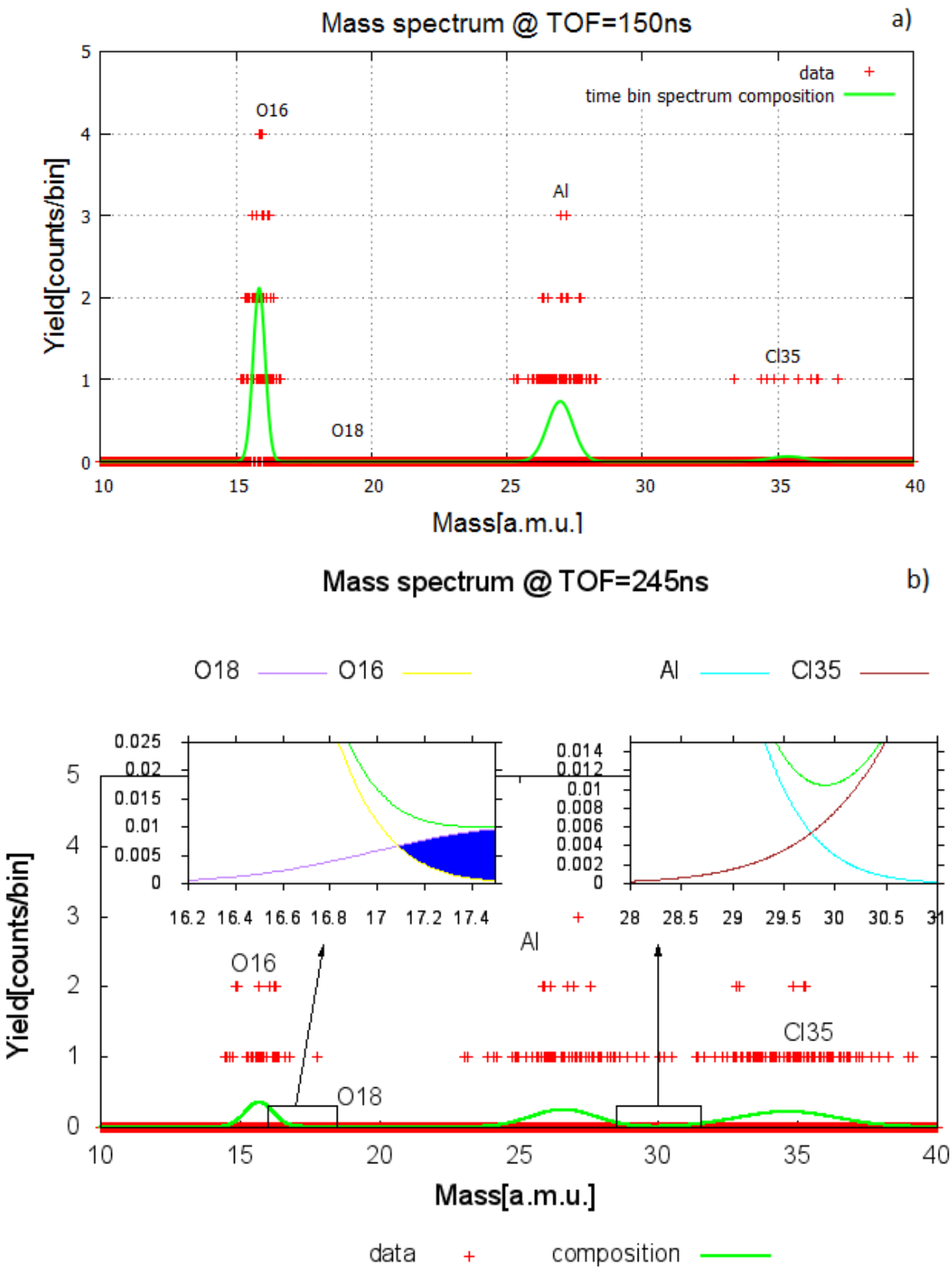

Figure 6-12 a) Time bin mass spectrum at TOF=150ns. In red recoil data are plotted, the green line represents the composition of the four optimal Gaussians corresponding to oxygen 16 and 18, aluminum and chlorine 35. In the insert the resolution of oxygen 18 is shown. b) Time bin mass spectrum at TOF=245ns. In red recoil data are plotted, the green line

represents the composition of the four optimal Gaussians corresponding to oxygen 16 and 18, aluminum and chlorine 35. Inserts show in yellow, purple, cyan and brown respectively decomposed Gaussians for oxygen 16, 18, aluminum and chlorine 35. In blue the overlapping regions of data respectively for the isotopic couples oxygen 16-18 and aluminum-chlorine 35.

At TOF=245 ns, where data overlap, the decomposition procedure allows to discriminate isotope 18 of oxygen and to separate aluminum from chlorine 35. This is showed in Figure 6-12b inserts. The blue areas represent the overlapping areas both for oxygen 16-18 and aluminum-chlorine35. The decomposed Gaussians for oxygen 16, 18, aluminum and chlorine are shown respectively in yellow, purple, cyan and brown. The decomposed Gaussians have area $A_{k,sim}$ and centroid $M_{el,k}$ listed in Table 6-4 rows 3 and 4.

At TOF=150 ns it's not possible anymore to distinguish abundance data A_k separately for oxygen 16 and 18 which have overlapped data and even for aluminum and chlorine 35 (Figure 6-11a). Thus in Table 6-4 row 1 we consider combined abundance data $A_{k,comb}$ for oxygen16-18 and aluminum-chlorine35.

On the other hand the procedure is able to discriminate separately the abundances $A_{k,sim}$ of oxygen 16 and 18, aluminum and chlorine35.

To test the goodness of the procedure at this TOF we can sum the decomposition abundance results $A_{k,sim}$ (Table 6-4 row 3) both for oxygen16-18 and aluminum-chlorine35. We get good agreement with combined abundance data $A_{k,comb}$ (Table 6-4 row 1).

If we repeat the time bin decomposition over the all TOF range where we recorded events, between 100 ns and 250 ns, we get the exact decomposed abundances for oxygen 16, oxygen 18, aluminum and chlorine 35 in each TOF bin.

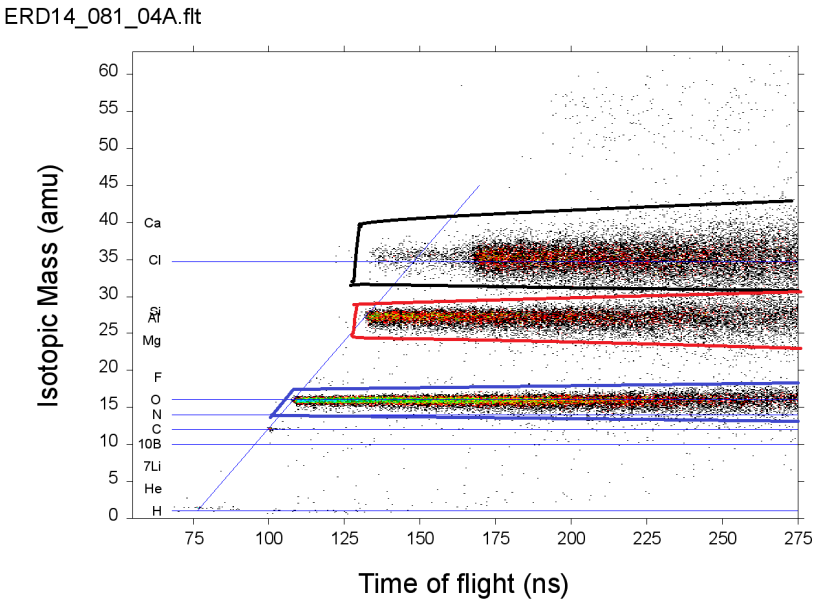

Figure 6-13 TOF-Mass histogram with manual selection of recoil events for the Al_2O_3 calibration sample analyzed with the IMEC setup. The black cut is the manual selection for chlorine 35, the red cut is for aluminum and the blue one for oxygen.

Human eye cannot distinguish between oxygen 16 and 18 events, that is why only one manual selection was drawn for total oxygen events.

To show this powerful result we plot with lines in Figure 6-14a the decomposed abundances for each analyzed isotopes as a function of TOF, called TOF distributions. TOF distributions are isotopically differentiated and they have time bin resolution of ~0.5ns.

In Figure 6-14a colored stars represent abundances as a function of TOF when a manual selection for each mass-banana is performed in the TOF-Mass histogram.

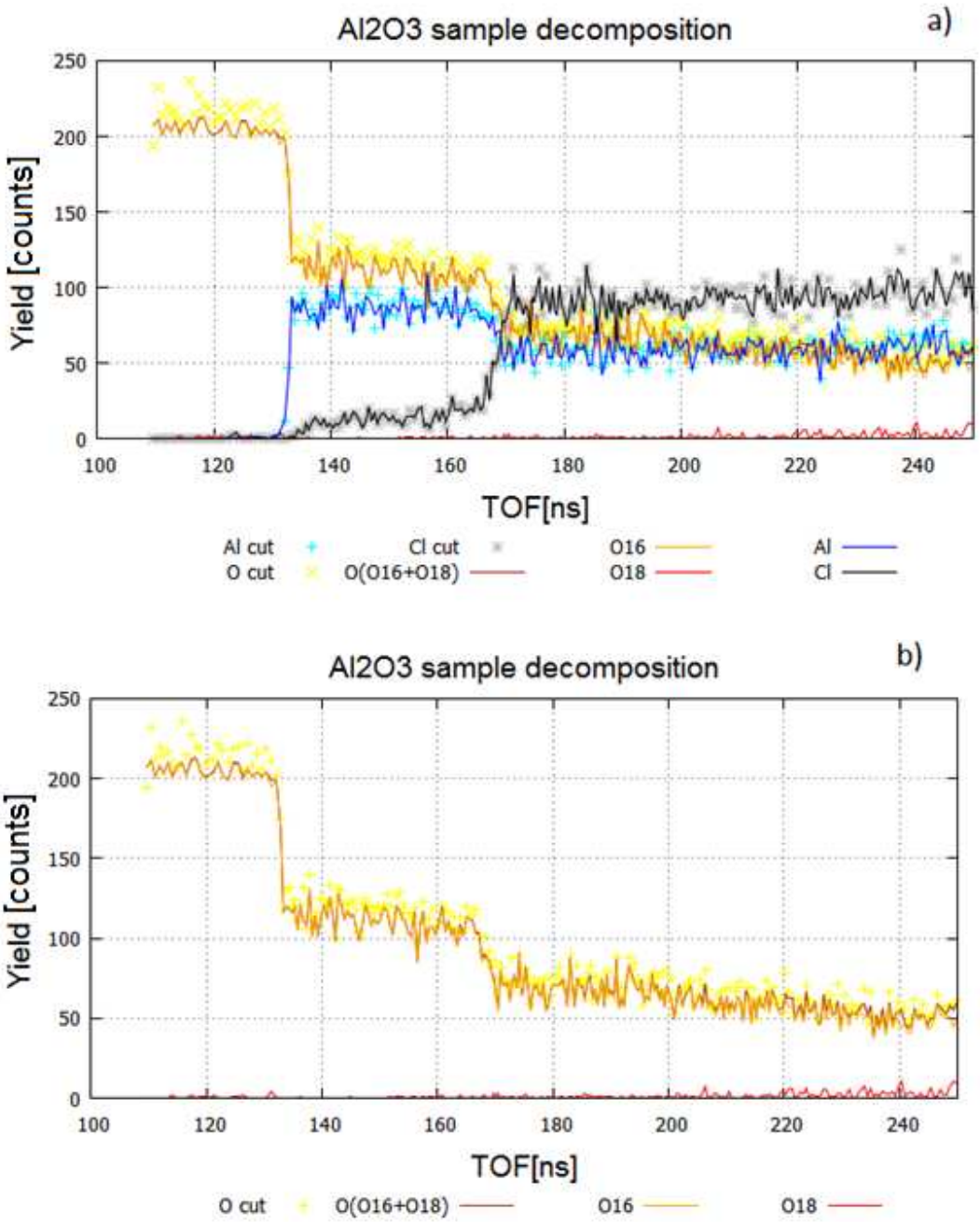

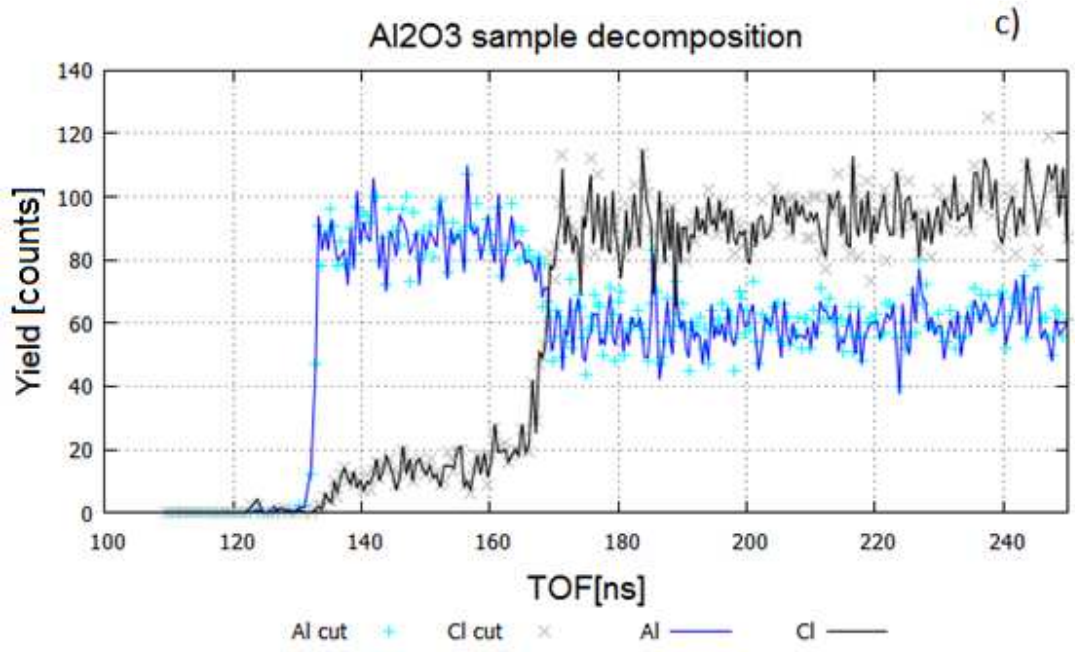

Figure 6-14 a) TOF distribution for the Al_2O_3 calibration sample analyzed with the IMEC setup. Lines represent the decomposed abundances for oxygen 16, 18, aluminum and chlorine 35 as a function of TOF. Colored stars represent abundances for oxygen, aluminum and chlorine 35 as a function of TOF when manual selections of recoils in each mass-banana is performed in the TOF-Mass histogram in Figure 6-13. b) TOF distribution with decomposed and manually selected abundances for oxygen 16 and 18. c) TOF distribution with decomposed and manually selected abundances for aluminum and chlorine 35.

In Figure 6-13 manual selections are drawn in the TOF-Mass histogram: the black selection is for chlorine 35, the red selection is for aluminum and the blue one for oxygen. Human eye cannot distinguish between oxygen 16 and 18 events, that is why only one manual selection was drawn for total oxygen events.

In Figure 6-14a it is visible the TOF region between 110ns and 130ns where all 200 counts in a time bin belong to oxygen, from TOF=130ns they become shared between the three elements. Good agreement between manual selected abundances and decomposed ones is observed, as in Figure 6-14a lines overwrite stars trends.

Figure 6-14b represents manual selection abundance for oxygen and decomposed abundances for the two isotopes of oxygen. In red oxygen 18 decomposed abundance is distinguishable.

Figure 6-14c represents manual selection abundance and decomposed abundances for aluminum and chlorine 35. It is visible in the TOF region between 130ns and 140ns that the black line for chlorine 35 is a bit higher than grey points (manual selection), and the blue line for aluminum is a bit lower than cyan points (manual selection). This could mean we overestimated the area of aluminum events and underestimated the area of chlorine 35 events in Figure 6-13 when manually selecting events.

With this decomposition procedure we make the discrimination of elements and isotopes free from human eye errors, and we are able to automatize it. This of course means reduction of work and money.

From TOF distributions depth profiles can be traced for each ERD experiment.

The depth profiles are obtained as follows: we convert the TOF for each isotopic yield into energy according to Eq. 4-1, where we know L is 755.4mm, T is the TOF and M the isotopic mass. Knowing the energies E and the isotopic yields Y_k it is possible to fill in Eq. 2-32 and follow the depth profiling algorithm.

Now depth profiles will report concentrations obtained from the decomposition, thus they will be free from any human mis-discrimination.

6.2.4 Advanced case of study and future outlook

The decomposition was performed on a sample made of 13nm-Al_2O_3 layer deposited on a silicon bulk. TOF-Energy data are showed in the TOF-Energy histogram in Figure 6-15.

TOF-Energy histogram like the one in Figure 6-15 could be a classical microelectronics example, where we have an Al layer, for interconnections, deposited on a silicon substrate and heavy oxygen contaminations from air.

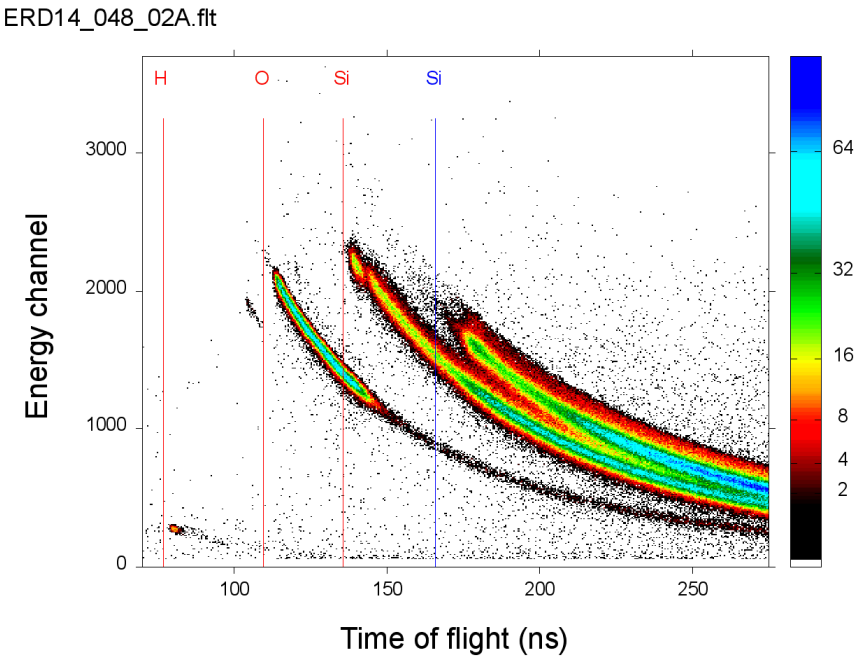

Figure 6-15 TOF-Energy histogram for a sample made of 13nm-Al_2O_3 layer deposited on a silicon bulk. TOF-Energy data were measured in June 2014.

TOF-Energy data were transformed into TOF-Mass data according to Eq. 4-15, where B parameters vary for each time bin. Thus we got the TOF-Mass histogram for this sample (Figure 6-16a). It is

clearly visible from the histogram in the TOF region around 140ns the data dot for aluminum which is at the surface; at higher TOF we have the silicon mass-banana.

To perform the integrated time decomposition on the Al_2O_3/Si sample we select in the TOF-Mass histogram the events comprised between TOF=50ns and TOF=175ns.

We can plot the time integrated mass spectrum for the sample in this TOF region (Figure 6-16b red crosses). In the analysis we exclude contaminations of carbon and hydrogen.

Results of the decomposition procedure in these two TOF regions are shown in Figure 6-16b. The green line is the optimized model expressed in Eq. 6-10, thus the composition of the five optimal Gaussians corresponding to oxygen 16 and 18, aluminum, silicon 28 and chlorine 35. The blue line is the decomposed Gaussian for aluminum, while the magenta line is the decomposed Gaussian for chlorine 35.

It is visible from Figure 6-16b that the composition of aluminum and silicon 28 Gaussians (green line in the region 25 a.m.u. : 35 a.m.u.) is not optimally fitting the data in red. Indeed data in red show a deviation from a Gaussian function especially in the mass region around 29 a.m.u., where it is visible a tail.

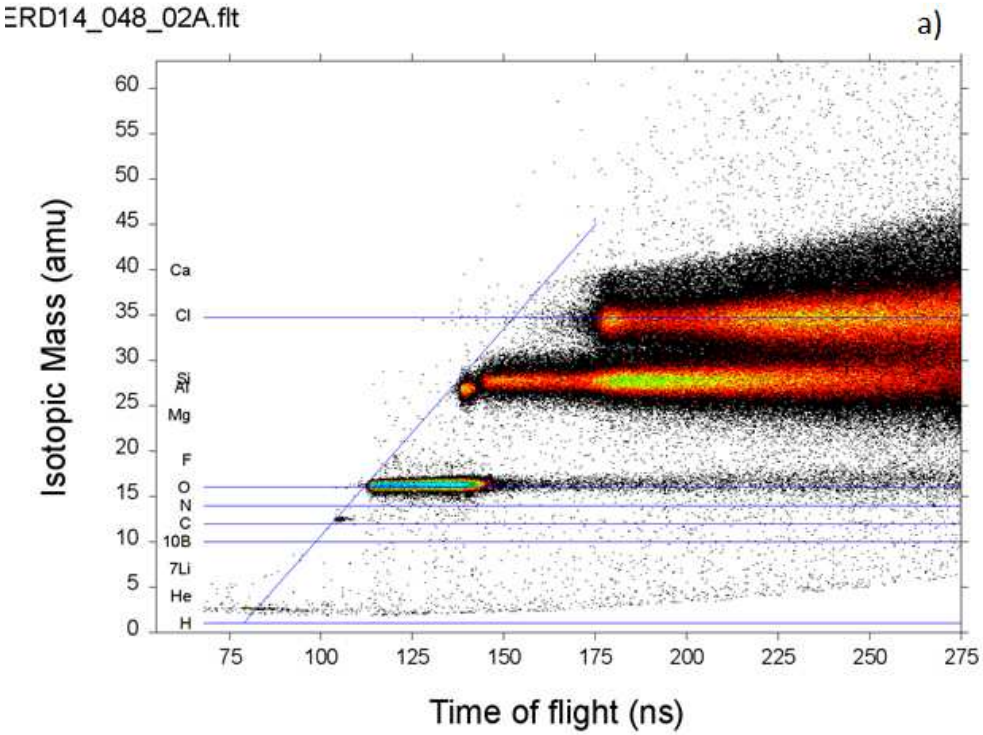

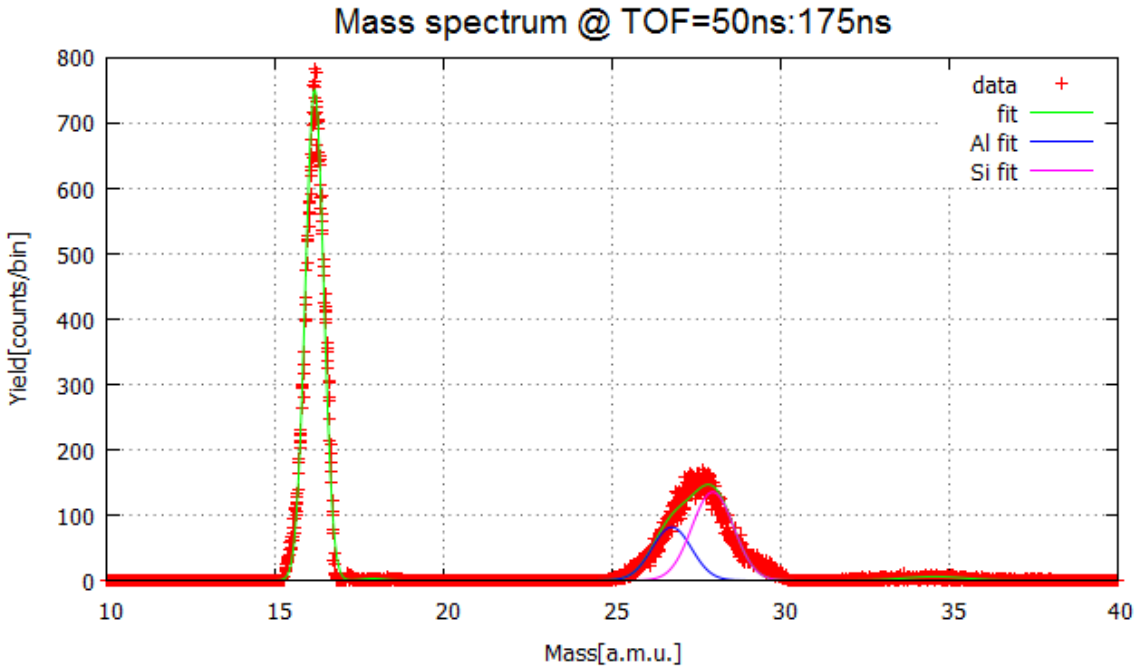

Figure 6-16 a) TOF-Mass histogram for the 13nm-Al_2O_3 layer deposited on Si sample analyzed with the IMEC setup. Apart from major sample elements like oxygen, aluminum and silicon, also hydrogen and carbon are present as small contaminations and chlorine 35 as scattered product from the ERD experiment. b) Integrated time mass spectrum in the TOF region between 50ns and 175ns. In red recoil data are plotted, the green line represents the composition of the five optimal Gaussians corresponding to oxygen 16 and 18, aluminum, silicon 28 and chlorine 35. The blue line represents the decomposed Gaussian for aluminum, and the magenta line shows the decomposed Gaussian for silicon 28.

This tail in the data leads to a misfit in the decomposition procedure. Moreover an heavy dependence between abundance and centroid values for aluminum, silicon 28, 29 and 30 Gaussians was observed. Thus we had to exclude from the decomposition analysis isotopes 29 and 30 of silicon.

Further improvements are needed in the decomposition procedure, in order to take into account cases where data deviate from normal Gaussian behavior. For instance as a future outlook a decomposition procedure that fits data with skewed Gaussians instead of normal ones could be implemented. Plus an algorithm which takes into account the dependence of Gaussians parameters for close isotopes could be implemented.

Summary

In the first part of this thesis work a new mass assignment procedure has been developed. The procedure allows to assign the mass to each recoil detected in an ERD experiment. The appropriateness of this technique is demonstrated by the fact that recoils from the same isotope in a sample are placed along straight iso-mass lines in the TOF-Mass histogram.

The procedure compared to the existing ones has main advantages:

- It takes into account the non-constant relation between the silicon energy detector response and the energy calculated according to the classical formula.
- Less computational effort. Indeed the masses assignment for an ERD experiment only requires few minutes of computation. While mass re-calibration, needed monthly in order to take into account radiation damage calibration shifts, needs half a day for data processing.
- It is always possible to add new isotopes as calibration references.

In the second part of this work an isotopic discrimination procedure was developed, the procedure is called ‘decomposition’.

The decomposition allows to:

- distinguish recoils from minor isotopes in a sample, otherwise they would not be discriminated by human eye;
- distinguish recoils from various isotopes in regions where data overlap, where human eye is incapable to discriminate;
- avoid human input to select certain intervals of data. Thus decomposition reduces errors, time effort and it allows to save money.

As future outlooks a more complex algorithm can be implemented to improve the decomposition procedure. The algorithm should fit skewed Gaussians, when data exhibit unexpected tails; and it should be optimized to take into account heavy correlation of the decomposition free parameters when data are seriously overlapped. Finally, taking data from the decomposed TOF distributions it would be possible to trace depth profiles more accurately.

Acknowledgements

The realization of this work would not have been possible without the help and the encouragement of many people.

First of all, I would like to thank my promoter Prof. Marcello Mariani and my daily supervisor at IMEC Dr. Johan Meersschaut. They both made it possible to realize one of my dreams, to be part of IMEC research. Plus I have really appreciated the freedom they offered me in the realization of this work. I owe a great debt of gratitude to Johan, who taught me with a lot of enthusiasm and professionalism most of the things I currently know of TOF-ERDA, and made my passion for it growing day by day.

I am thankful to my opponent Dr. Federica Zanderigo, for her precious advices.

A special thank goes to Johan Desmet, for good advices and data. My thanks also go to my MCA colleagues for the nice working atmosphere, great lunches, coffee breaks and for their friendships inside and outside IMEC.

I would like to thank my parents, and whole family for their patience and their entire and unconditional support. And finally thanks to all my friends, both in Milan and Bari. Among them I want to thank Claudia, her support was invaluable.

REFERENCES

[1] Y. Wang, M. Nastasi.
Handbook of Modern Ion Beam Materials Analysis 2nd Edition. Materials Research Society. **1** (2009) 83-121.

[2] S. Giangrandi.
Low-energy elastic recoil detection and ion beam analysis for quantitative elemental profiling of thin films. PhD Thesis (2010) 9-19 21-22 31-34 42-50.

[3] E. J. Sternglass.
Theory of secondary electron emission by high-speed ions. Phys. Rev. **1** (1957) 108.

[4] P. Koschar, K. Kroneberger, A. Clouvas, M. Burkhard, W. Meckbach, O. Heil, J. Kemmler, H. Rothard, K. O. Groeneveld, R. Schramm, and H. D. Betz.
Secondary-electron yield as a probe of pre-equilibrium stopping power of heavy ions colliding with solids. Phys. Rev. **A 40** (1989) 3632.

[5] Y. Zhang, H. J. Whitlow, T. Winzell.
Influence of heavy ion irradiation damage on silicon charged particle detector calibration. Nuclear Instruments and Methods in Physics Research **B 161-163** (2000) 297-301.

[6] T. L. Alford, L. C. Feldman, J. W. Mayer.
Fundamentals of Nanoscale Film Analysis. Springer. **1** (2007) 12-21.

[7] A. Bergmaier, G. Dollinger, C. M. Frey.
Quantitative elastic recoil detection. Nuclear Instruments and Methods in Physics Research **B 99** (1995) 488-490.

[8]M. El Bouanani, M. Hult, L. Persson, E. Swietlicki, M. Andersson, M. Östling, N. Lundberg, C. Zaring,
D. D. Cohen, N. Dytlewski, P. N. Johnston, S. R. Walker, I. F. Bubb, H. J. Whitlow.
Multivariate analysis method for energy calibration and improved mass assignment in recoil spectrometry. Nuclear Instruments and Methods in Physics Research **B 94** (1994)530-536.

[9] L. Persson, H. J. Whitlow, M. El Bouanani, M. Hult, M. Andersson, I. F. Bubb, D. D. Cohen, N. Dytlewski, P. N. Johnston, S. R. Walker, C. Zaring, M. Östling.
Separation of mass-overlapped time of flight-energy elastic recoil detection analysis data using Ryan and Jamieson's dynamic analysis method. Nuclear Instruments and Methods in Physics Research **B 179** (2001) 403–411.

[10] P.F. Hinrichsen, D.W. Hetherington, S.C. Gujrathi, L. Cliche.
Heavy-ion energy resolution of SSB detectors. Nuclear Instruments and Methods in Physics Research **B 45** (1990) 275-280.

[11] M. Hult, M. El Bouanani, L. Persson, H. J. Whitlow, M. Andersson, C. Zaring, M. ***Ö***stling, D. D. Cohen, N. Dytlewski, I. F. Bubb, N. Johnston, S. R. Walker.

Empirical characterization of mass distribution broadening in TOF-E recoil spectrometry. Nuclear Instruments and Methods in Physics Research **B 101** (1995) 263-266.

[12] M. Döbeli, C. Kottler, M. Stocker, S. Weinmann, H.-A. Synal, M. Grajcar, M. Suter.
Gas ionization chambers with silicon nitride windows for the detection and identification of low energy ions. Nuclear Instruments and Methods in Physics Research **B 219-220** (2004) 415-419.

[13] M. Hult, H. J. Whitlow, M. *Ö*stling.
High-resolution recoil spectrometry for separate characterization of Ga and As in $Al_xGa_{(1-x)}As$ structures. Journal of applied physics letters **60** (1992) 219.

[14] M. Laitinen.
Improvement of time-of-flight spectrometer for elastic recoil detection analysis. PhD Thesis (2013) 19-28.

[15] T. Sajavaara, M. Laitinen.
TOF-ERDA–project to IMEC, Belgium. Presentation (2013) 1-13.

[16] T. Sajavaara.
Heavy Ion Recoil Spectroscopy of Surface Layers. Academic dissertation (2002) 13-14.

[17] K. Suzuki.
Analysis of ion implantation profiles for accurate process/device simulation: analysis based on quasi-crystal extended LSS theory. FUJITSU Sci. Tech. J. **46-3** (2010) 318-320.

[18] M. Mallepell.
Ringförmiger gasionisationsdetektor für schwerionen-rückstreuanalyse. PhD Thesis (2009) 107-123.

[19] C. Kottler, M. D*ö*beli, F. Glaus, M. Suter.
A spectrometer for low energy heavy ion ERDA. Nuclear Instruments and Methods in Physics Research **B 248** (2006) 155-162.

[20] M. Hult, H. J. Whitlow, M. ***Ö***stling, M. Andersson, Y. Andersson, I. Lindeberg, K. Stahl.
Rapid thermal annealing induced reactions of Co/GaAs thin film structures: studies using mass and energy dispersive recoil spectrometry. Journal of applied physics letters **75** (1994) 835-843.

[21] T. Hauschild, M. Jentschel.
Comparison of maximum likelihood estimation and chi-square statistics applied to counting experiments. Nuclear Instruments and Methods in Physics Research **A 457** (2001) 384-401.

[22] M. Mariani.
Interconnesioni. Presentation for the academic course 'Technologies and processes for microelectronics' (2014) 1-42.

[23] U. Bexell.
Surface Characterisation Using ToF-SIMS, AES and XPS of Silane Films and Organic Coatings Deposited on Metal Substrates. PhD Thesis (2003) 13-24.

[24] M. Laitinen, M. Rossi, J. Julin, T. Sajavaara.

Time-of-flight – Energy spectrometer for elemental depth profiling – Jyväskylä design. Nuclear Instruments and Methods in Physics Research **B 337** (2014) 55–61.

[25] Del Mar Photonics, *Microchannel Plates and MCP Detectors and Imaging Systems,* **http://www.dmphotonics.com/MCP_MCPImageIntensifiers/mcp_references.htm** (26/03/2015).

[26] Wikipedia, *Microchannel plate detector,* **http://en.wikipedia.org/wiki/Microchannel_plate_detector** (26/03/2015).

[27] Photonis USA INC, *Long-life microchannel plates,* **http://www.optimacorp.co.jp/BurleEO/MCP.htm** (26/03/2015).

[28] M. Laitinen, T. Sajavaara.
Trajectory bending and energy spreading of charged ions in time-of-flight telescopes used for ion beam analysis. Nuclear Instruments and Methods in Physics Research **B 325** (2014) 101-106.

[29] J. Meersschaut, M. Käyhkö, H. P. Lenka, T. Witters, Q. Zhao et al.
RBS and PIXE analysis of chlorine contamination in ALD-Grown TiN films on silicon. AIP Conf. Proc. **1525**, (2013) 190- 194.